TECHNISCHE UNIVERSITÄT MÜNCHEN

TUM School of Engineering and Design

Monitoring and Optimizing the Surface Quality of Friction Stir Welds Using Machine Learning

Roman Hartl

Vollständiger Abdruck der von der TUM School of Engineering and Design der Technischen Universität München zur Erlangung des akademischen Grades eines

Doktors der Ingenieurwissenschaften

genehmigten Dissertation.

Vorsitz:	Prof. Dr.-Ing. Wolfram Volk
Prüfer*innen der Dissertation:	1. Prof. Dr.-Ing. Michael F. Zäh
	2. Prof. Dr.-Ing. Darius Burschka

Die Dissertation wurde am 19.04.2021 bei der Technischen Universität München eingereicht und durch die TUM School of Engineering and Design am 24.09.2021 angenommen.

Acknowledgment

This dissertation was elaborated during my engagement as a research associate at the Institute for Machine Tools and Industrial Management (*iwb*) at the Technical University of Munich (TUM).

First, I would like to thank Prof. Dr.-Ing. Michael F. Zäh, the full professor of the Chair of Machine Tools and Manufacturing Technology, for the opportunity to pursue my doctorate and for his favorable and generous support toward my research work. Additionally, I would like to thank him for the opportunity to be a member of the institute's management board and to be in charge of the Machine Tools Department. I am grateful to Prof. Dr.-Ing. Darius Burschka, Chair of Robotics, Artificial Intelligence and Real-time Systems, for his careful review as a co-examiner of this dissertation. I also wish to thank Prof. Dr.-Ing. Wolfram Volk, full professor of the Chair of Metal Forming and Casting, for presiding the doctoral viva of this work.

My gratitude extends to my colleagues at the *iwb*, particularly the members of the Joining and Cutting Technology Department and the Machine Tools Department. I want to especially thank Stefan Meyer, Christina Häußinger, Christoph Wunderling, Florian Günter, Maximilian Schmöller, and Christian Stadter for the valuable, multidisciplinary discussions and for a memorable, great time.

I am also grateful to Dr.-Ing. Andreas Bachmann, Martina Sigl, Maximilian Benker, and Prof. Dr. Jutta Stirner for carefully reviewing this dissertation.

Finally, I would like to express my sincere gratitude to my family and friends who have given me the strength and support to overcome any situation in life. The biggest thank you goes to my girlfriend Sabrina Brams for the continuous support and backing she has provided me.

Munich, October 2021 *Roman Hartl*

Table of Contents

List of Abbreviations

Abbreviation	Description
AI	**A**rtificial **i**ntelligence
ANN	**A**rtificial **n**eural **n**etwork
AS	**A**dvancing **s**ide
AW	**A**luminum **w**rought alloy
BM	**B**ase **m**etal
BO	**B**ayesian **o**ptimization
CAM	**C**omputer-**a**ided **m**anufacturing
CCD	**C**harge-**c**oupled **d**evice
CMOS	**C**omplementary **m**etal **o**xide **s**emiconductor
CNN	**C**onvolutional **n**eural **n**etwork
CPU	**C**entral **p**rocessing **u**nit
Cr	Chromium
Cu	Copper
CUDA	**C**ompute **u**nified **d**evice **a**rchitecture
DFT	**D**iscrete **F**ourier **t**ransform/**t**ransformation
DIN	German Institute for Standardization (German: **D**eutsches **I**nstitut für **N**ormung)
DWT	**D**iscrete **w**avelet **t**ransform/**t**ransformation
EN	European standard
FCNN	**F**ully **c**onnected **n**eural **n**etwork
FD	**F**ractal **d**imension
Fe	Iron
FEM	**F**inite **e**lement **m**ethod
FSW	**F**riction **s**tir **w**elding
GA	**G**enetic **a**lgorithm

GLCM	**G**ray-**l**evel **c**o-occurrence **m**atrix
GP	**G**aussian **p**rocess
GPR	**G**aussian **p**rocess **r**egression
GPU	**G**raphics **p**rocessing **u**nit
GUI	**G**raphical **u**ser **i**nterface
HAZ	**H**eat-**a**ffected **z**one
IOU	**I**ntersection **o**ver **u**nion
ISO	International Organization for Standardization
iwb	Institute for Machine Tools and Industrial Management (German: **I**nstitut für **W**erkzeugmaschinen und **B**etriebswissenschaften) of Technical University of Munich (TUM)
KDD	**K**nowledge **d**iscovery in **d**atabases
MDP	**M**arkov **d**ecision **p**rocess
Mg	Magnesium
ML	**M**achine **l**earning
Mn	Manganese
NASA	**N**ational **A**eronautics and **S**pace **A**dministration
no.	Number
P	**P**ublication
p.	**P**age
PCC	**P**earson **c**orrelation **c**oefficient
PRF	**P**otential **r**esearch **f**ield
R-CNN	**R**egion-based **c**onvolutional **n**eural **n**etwork
RA	**R**esearch **a**rea
RAM	**R**andom **a**ccess **m**emory
RBF	**R**adial **b**asis **f**unction
RL	**R**einforcement **l**earning
RNN	**R**ecurrent **n**eural **n**etwork
ROI	**R**egion **o**f **i**nterest
RP	**R**esearch **p**rogress
RPD	**R**obust **p**arameter **d**esign

RPM	**R**evolutions **p**er **m**inute
RS	**R**etreating **s**ide
RSM	**R**esponse **s**urface **m**ethodology
S/N	**S**ignal-to-**n**oise
Si	Silicon
SPP	**S**tatic **p**ayback **p**eriod
SSD	**S**ingle **s**hot **d**etector
ST	**S**ub-**t**arget
SVM	**S**upport **v**ector **m**achine
TCP	**T**ool **c**enter **p**oint
Ti	Titanium
TMAZ	**T**hermo**m**echanically **a**ffected **z**one
TOPSIS	**T**echnique for **o**rder **p**reference by **s**imilarity to **i**deal **s**olution
TUM	**T**echnical **U**niversity of **M**unich
TWI	**T**he **W**elding **I**nstitute
VRAM	**V**ideo **r**andom **a**ccess **m**emory
WLAN	**W**ireless **l**ocal **a**rea **n**etwork
YOLO	**Y**ou **o**nly **l**ook **o**nce
Zn	Zinc

List of Symbols

Vectors are printed in bold (such as $\boldsymbol{x}$), and matrices are capitalized and printed in bold (such as $\boldsymbol{\Sigma}$). To increase the readability, the list in this chapter is sorted by the topics as they are found in this thesis.

Friction stir welding

Variable	Unit	Description
a_x	m/s^2	Acceleration in welding direction
a_y	m/s^2	Acceleration perpendicular to the welding direction in the plane of the workpiece surface
a_z	m/s^2	Acceleration normal to the workpiece surface
d_{arc}	mm	Height difference between a local valley and the subsequent local peak along the weld centerline
d_c	mm	Diameter of a cavity
def	–	Scaled surface defects
d_{P}	mm	Tool probe diameter
d_{R}	mm	Depth of the rings for a tool shoulder with concentric rings
d_{S}	mm	Tool shoulder diameter
d_{Sp}	mm	Spiral depth for a tool shoulder with a spiral shape
f	mm	Flash height
f_{m}	mm	Mean flash height
f_{max}	mm	Maximum flash height
f_{rev}	mm	Feed per tool revolution
F_x	N	Force in welding direction
F_y	N	Force perpendicular to the welding direction in the plane of the workpiece surface
F_z	N	Force in axial tool direction

l	mm	Weld seam length
l_P	mm	Probe length
M_z	Nm	Spindle torque
n	min^{-1}	Tool rotational speed
N	–	Scaled values for the topography indicators
n_count	–	Counted number of local valleys and local peaks along the weld centerline
n_theoret	–	Theoretical number of local valleys and local peaks along the weld centerline
p_d	mm	Plunge depth of the tool center point
R^2	–	Coefficient of determination
Ra	µm	Arithmetic mean deviation of the assessed profile
r_arc	–	Ratio between the counted number and the theoretical number of local peaks and local valleys along the weld centerline
R_m	MPa	Tensile strength
r_P	mm	Tool probe radius
r_R1, r_R2, r_R3	mm	Radii of the rings for a tool shoulder with concentric rings
r_S	mm	Tool shoulder radius
S_d	mm	Standard deviation of d_arc
S_f	mm	Standard deviation of the flash height f
S_u	mm	Standard deviation of the seam underfill u
S_w	mm	Standard deviation of the weld seam width w
T_P	°C	Temperature at the tool probe
T_S	°C	Temperature at the tool shoulder
t_S	mm	Sheet thickness
u	mm	Seam underfill
u_m	mm	Mean seam underfill
V_mp	ml/m²	Peak material volume
v	mm/min	Welding speed
w	mm	Weld seam width
w_Sp	mm	Spiral width for a tool shoulder with a spiral shape

α	°	Tilt angle
ß	°	Conical tool probe angle
γ	°	Concave tool shoulder angle
ζ, η	°	Angles of the rings for a tool shoulder with concentric rings

Artificial neural networks

Variable	Description
b_i	Bias for the *i*-th neuron
f	Activation function
N_i	Total number of inputs for the *i*-th neuron
t	Discrete time step
$\boldsymbol{w_i}$	Vector with all weights for the inputs of the *i*-th neuron
$w_{j,i}$	Weight for the *j*-th input of the *i*-th neuron
$\boldsymbol{x_i}$	Vector with all inputs of the *i*-th neuron
$x_{j,i}$	*j*-th input of the *i*-th neuron
x_t	Input at time step t
y_i	Output of the *i*-th neuron
y_t	Output at time step t

Gaussian processes and Bayesian optimization

Variable	Description
$y \mid x$	Conditional random variable y given x
$\mathcal{D}$	Data set
d	Number of dimensions
$\mathbb{E}(x)$	Expectation of the random variable x
$\mathcal{GP}$	Gaussian process
$k(\boldsymbol{x}, \boldsymbol{x}')$	Covariance function (or kernel) of a Gaussian process evaluated at $\boldsymbol{x}$ and $\boldsymbol{x}'$
l	Length-scale
$m(\boldsymbol{x})$	Mean function of a Gaussian process evaluated at $\boldsymbol{x}$
$\mathcal{N}(\mu, \sigma^2)$ or $\mathcal{N}(x \mid \mu, \sigma^2)$	One-dimensional Gaussian (normal) distribution with mean μ and variance σ^2

$\mathcal{N}_d(\boldsymbol{\mu}, \boldsymbol{\Sigma})$ or $\mathcal{N}_d(\boldsymbol{x} \mid \boldsymbol{\mu}, \boldsymbol{\Sigma})$	d-dimensional Gaussian (normal) distribution with mean vector $\boldsymbol{\mu}$ and variance-covariance matrix $\boldsymbol{\Sigma}$
$p(f(x_i))$	Predictive distribution of the function value $f(x_i)$
$\mathrm{Var}(x)$	Variance of the random variable x
$\boldsymbol{x}$	Normal random vector
x	One-dimensional random variable
δ	Kronecker delta
ε	Gaussian noise
$\boldsymbol{\theta}$	Vector of hyperparameters
$\mu(x)$	Mean of the random variable x
$\boldsymbol{\mu}$	Mean vector of the random vector $\boldsymbol{x}$
$\boldsymbol{\Sigma}$	Variance-covariance matrix
σ^2	Variance of the random variable x
σ_f^2	Signal variance
σ_n^2	Noise variance

Markov decision processes

Variable	**Description**
A	Set of all possible actions
a	Action
a_t	Action at time step t
$p(s', r \mid s, a)$	Probability of transition to successor state s' with reward r, from state s and action a
r_t	Reward at time step t
S	Set of all possible states
s, s'	State and successor state
s_t	State at time step t
π	Policy (decision-making rule)

Economic potential analysis

Variable	Unit	Description
A_E or A_S or A_T	€/a	Annual costs for employees or an automated surface inspection system or for a tensile testing machine
$B_{S/E}$ or $B_{S/T}$	€/a	Annual monetary benefit of the automated surface inspection system compared to employees or compared to a tensile testing machine
B_{WT}	€	Monetary benefit per welding task when applying the developed algorithm-based process parameter determination
B_{TT}	€	Monetary benefit for one substituted tensile test
$C_{BO/WT}$ or $C_{E/WT}$	€	Costs to determine suitable process parameters for one welding task when using the developed algorithm or not
C_E	€/h	Labor costs per hour
C_S or C_T	€	Investment costs for an automated surface inspection system or for a tensile testing machine
C_{WP}	€	Costs for one workpiece
D_E	d/a	Working days per year
D_S or D_T	€/a	Imputed depreciation per year for an automated surface inspection system or for a tensile testing machine
H_E	h/d	Working hours per day
I_S or I_T	€/a	Imputed interests per year for an automated surface inspection system or for a tensile testing machine
M_S or M_T	€/a	Maintenance and service costs per year for an automated surface inspection system or a tensile testing machine
N_{WT}	1/a	Necessary welding tasks per year such that the algorithm-based process parameter determination is profitable
R	%	Imputed interest rate
St_{BO} or St_E	–	Required steps to find suitable process parameters when using the developed Bayesian optimization algorithm or not
T_{WT}	h	Time to produce one weld
T_T	h	Time to perform one tensile test

1 Introduction

1.1 Impact of digital technologies on production engineering

Manufacturing can be defined as "the application of mechanical, physical, and chemical processes to convert the geometry, properties, and/or appearance of a given starting material to make finished parts or products" (RAO 2011, p. 1). It is a fundamental means of human existence and contributes significantly to increasing prosperity (HITOMI 1996, p. 497). Various trends including globalization, environmental sustainability, and digitalization have far-reaching implications on manufacturing (HAMMER 2019, p. 25). Digitalization in particular yields immense financial opportunities: The potential benefits for business community and society were estimated to reach $100 trillion in the period from 2016 to 2025 by the World Economic Forum (MARTIN ET AL. 2017). There are different definitions of the term "digitalization." According to WOLF & STROHSCHEN (2018, p. 58), "digitalization" means that analogue services are fully or partially replaced by services in a digital, computer-manageable model. Regarding digitalization, four main computational technologies have arisen in the past few decades that have resulted in changes in the interaction between humans and computers. The chronological order of these four technologies is information systems, e-business applications, web 2.0 revolution, and artificial intelligence (AI; DORNBERGER ET AL. 2018, p. 2).

The latest technology, which is AI, uses nature-inspired methods to overcome problems that are connected to the constantly rising amount and complexity of data that is to be processed in real-world applications. The conventional mathematical methods that have been used so far are only suitable to a minor extent to represent processes holistically and to make analyses, predictions, and decisions on this basis (WILLENBACHER ET AL. 2018, p. 226). Traditional methods also quickly reach their limits when processing fuzzy knowledge or erroneous data (ALFRED 1995, pp. 231 f.), when dealing with changing boundary conditions, and when handling problems for which there is no known algorithm (GÉRON 2017, pp. 6 f.). Research on AI had already begun in the latter half of the 20th century, but it led to disenchantment in the 1990s, because in theory AI promised better results than the computing power available at that time allowed. However, since then, computational performance has increased significantly. As a result, data can now be transferred and processed faster, algorithms that require enormous computing power can be applied, and machines have begun to "learn" from data (DORNBERGER ET AL. 2018, pp. 5 – 7).

Manufacturers can apply AI-based techniques such as machine learning (ML), deep learning, and artificial neural networks (ANNs) to deal with high-dimensional data acquired from production to reveal previously unrecognized or undiscovered know-how and to determine implicit relations in the data (WUEST ET AL. 2016, p. 28). In this way, the usage of AI can help to monitor, optimize, and control manufacturing processes in enterprises (WUEST ET AL. 2016, p. 27) and consequently support the implementation of energy- and resource-saving production, which is important for industrial enterprises to work economically and in turn to remain competitive. The number of companies investing in the development of their own AI applications is therefore steadily increasing (WILLENBACHER ET AL. 2018, pp. 225 f.). A study with one of the first utilizations of AI in manufacturing was published in 2018 by the automobile manufacturer Audi AG (Ingolstadt, Germany), stating its intention to use deep learning in series production. For this purpose, Audi developed a software that enables the detection and marking of cracks in sheet metal parts in the press shop. The ML application was intended to replace visual inspection by employees and the previous optical crack detection system, which used several smart cameras that evaluated the captured images by using image recognition software based on simple algorithms. For the new AI-based system, ANNs were trained over a period of many months with the help of millions of images. The greatest challenges that were mentioned were the creation of a sufficiently large amount of data and the labeling of the images. During the labeling phase, the cracks in the images were marked by hand. There were two advantages of the new machine-learning-based software compared to the former optical inspection system that used smart cameras. First, in contrast to the new method, the former method used smart cameras that had to be reconfigured for each component, for example, doors, engine hoods, or fenders. Second, the previous technology was prone to errors, as the simpler algorithms of the smart cameras were highly dependent on environmental factors such as exposure conditions or the surface quality of the components (TANER & BOESCH 2018). This use case demonstrates that the application of AI in production is possible, makes sense, and offers great benefits for the evaluation of sensor data.

1.2 Significance of friction stir welding in industry

Towards the end of the 19th century, welding established itself as a viable manufacturing process (MESSLER 2004, p. 6). To accomplish this, various key discoveries were necessary such as the production of acetylene gas, the invention of resistance welding, and the development of carbon arc welding. Gas welding and arc welding are fusion welding techniques, which means that the workpieces first locally melt together and then join during solidification (LOHWASSER & CHEN 2010, p. 2).

Besides fusion welding processes, there are also solid-state welding techniques, which include friction stir welding (FSW). Some important technological progress in solid-state welding was necessary prior to the invention of FSW. One major step was the development of friction welding in 1956 (MESSLER 2004, p. 8). In friction welding, the components to be joined are pressed together after setting them in motion relative to each other. This creates frictional heat and softens the material in the joining area. Finally, elevated pressure is exerted on the softened material to achieve a metallurgical bond. Therefore, the workpieces do not melt. In this way, welds can be executed without solidification-caused porosities or cracks and with minimal deformation. There is also no need to employ shielding gases, and there are no arc-related emissions and fumes. Thus, welding processes without melting are regarded as environmentally friendly. However, the relative movement, which is required to develop heat and soften the material, can practically only be rotational (rotary friction welding) or linear (linear friction welding) in friction welding. Consequently, the geometry of the welded parts is restricted, and the applications are limited. This problem was overcome by the discovery of FSW (LOHWASSER & CHEN 2010, pp. 2 f.). In 1991, Wayne Thomas and his colleagues at The Welding Institute (TWI) in England realized that by employing a rotating tool consisting of a material that is harder than the workpieces and is used to exert friction and stirring, the workpiece material becomes plasticized. In addition, the rotation establishes an effective transport mechanism to convey the plasticized material around the tool, thus joining the components together. This marked the invention of the FSW process and enabled friction welding to be applied to a wide range of component geometries (LOHWASSER & CHEN 2010, p. 3). The first commercial application of FSW took place in 1995 in Scandinavia. There, aluminum extrusion profiles used for shipbuilding were welded to large panels with minimal distortion (KALLEE 2010, p. 118). To date, FSW has been applied most successfully for aluminum alloys because of the simple application of the process for this material group and the usage of these alloys in many important industries (LOHWASSER & CHEN 2010, p. 4).

Since its invention, the greatest interest in FSW has been shown by the aerospace industry, where it has become a suitable alternative to riveting. Many high-strength aluminum alloys that were previously considered un-weldable due to defects occurring during fusion welding have become weldable with FSW. Thus, in the early-to-mid 1990s, the companies Airbus SE (Toulouse, France) and Boeing Corporation (Chicago, IL, USA), and the National Aeronautics and Space Administration (NASA; Washington, D.C., USA) started to qualify FSW for the production of aircraft structures, rocket fuel tanks, and external fuel tank sections (LOHWASSER & CHEN 2010, pp. 4 f.). In the Ariane 6 program, the manufacturer MT Aerospace AG (Augsburg, Germany) is responsible for the design, qualification, and series production of components such as metallic bare tanks for the new heavy European launcher. New manufacturing techniques were necessary due to the increased launch rates and the ambitious performance and cost requirements. One focus in the development of new processes was the qualification of FSW for the Ariane 6 program (MERINO ET AL. 2017).

Apart from aviation, the automotive industry and especially the electromobility are currently developing markets for FSW (RICHTER 2017). According to RICHTER (2017), when battery housings of electric vehicles are manufactured, various aluminum alloys must be welded in butt or overlap configurations. Additionally, the welds must be leak-tight to seal cooling circuits for the battery and must be able to reliably withstand alternating loads and vibrations during the vehicle’s lifetime. Finally, a large bonding cross section and defect-free and compacted welds are required. These conditions and requirements make FSW a suitable process to fabricate battery storage for electromobility. The International Energy Agency predicts that electric vehicle sales will reach 44 million vehicles per year by 2030 (IEA 2019). Based on current car and battery designs, this would require approximately 400,000 km of FSW joints per year (PARRATT & MARTIN 2019). According to RICHTER (2017), the assembly of battery modules in battery packs imposes strict requirements for technical cleanliness. One aspect to which attention must be paid when using FSW in the production of battery packs is flash formation. In particular, the creation of metal particles and chips on the weld surface must be avoided. This must be considered when planning the welding process and the production system.

1.3 Problem statement and structure of the thesis

With the increasing use of FSW, demand is growing for non-destructive evaluation methods that are more reliable than those currently available on the market. Effective quality monitoring is important, especially in safety-critical applications, such as aviation and electromobility (TAHERI ET AL. 2019). Therefore, the work presented in this publication-based thesis is intended to contribute to a more reliable, non-destructive monitoring and an efficient optimization of friction stir welds by making use of the possibilities provided by digitalization and progress in the field of AI. As described by RICHTER (2017), one important criterion in FSW is surface quality. This is addressed in this thesis. Its focus is therefore set on the algorithm-based automated detection and optimization of surface defects and properties.

The thesis is structured as follows: the necessary basics for understanding the research results are presented in Chapter 2. In particular, the fundamentals of FSW and relevant ML methods are explained. Existing research results from other researchers that are related to this thesis are described in Chapter 3. In Chapter 4, a more precise definition of the scientific objectives of this thesis follows along with an explanation of the methodology to achieve them. Chapter 5 contains short summaries of the embedded publications. In Chapter 6, the presented technical approaches are assessed from an economic point of view. The findings are summarized in Chapter 7 and an outlook is given on promising future research that can follow this work.

2 Fundamentals

2.1 Chapter overview

The presentation of the fundamental knowledge on which this thesis is based is subdivided into three sections: basic information about aluminum alloys and their designation (Section 2.2), the FSW process (Section 2.3), and the applied ML methods (Section 2.4).

The description of the FSW process sequence, the most important weld characteristics, as well as input, output and process variables of the welding process are dealt with in Subsections 2.3.1 to 2.3.3.

Subsection 2.4.1 provides an overview of various methods of AI, ML, and deep learning. The approaches relevant for the work of this thesis are explained in more detail in Subsections 2.4.2 to 2.4.5.

2.2 Aluminum alloys

Since the majority of commercial applications of FSW concern the joining of aluminum alloys (ISO 25239-1), some Al alloys were also used for the investigations in this thesis. Most aluminum alloys contain from 90 % to 96 % aluminum. It is common for aluminum alloys to contain several minor alloying elements in addition to one or two main alloying elements to improve the workability or achieve certain material properties (KAUFMAN 2000, p. 6). The most important parent groups of aluminum alloys are the following (KAUFMAN 2000, p. 6):

- **Strain-hardenable aluminum alloys:** The alloying elements do not provide significant solid solution or precipitation strengthening in any form of thermal treatment. These alloys must therefore be strengthened utilizing strain hardening, for example, by cold rolling or drawing.
- **Heat-treatable aluminum alloys:** The alloying elements provide considerable solid solution as well as precipitation strengthening throughout the solution heat treatment and subsequent aging.
- **Wrought aluminum alloys:** These alloys are produced in the form of ingots or billets and then are transformed into semi-finished products by processes such as rolling or drawing.
- **Cast aluminum alloys:** These alloys are typically used in parts that are cast into the final or the near-final shape. They are not used for subsequent metal shaping processes.

Since only wrought alloys were used for the work in this thesis, these are described in more detail in the following paragraphs. The standard DIN EN 573-1 regulates the numerical designation of the chemical composition and shape of semi-finished products. The general designation essentially consists of the use of the prefix *EN*, followed by the letter *A* for aluminum and the letter *W* for wrought products and four digits for the chemical composition. The numerical designation system for the different alloy groups is listed in Table 2.1.

Table 2.1: Numerical designation system for aluminum alloys (DIN EN 573-1)

Numerical designation	Alloy group
1xxx (Serie 1000)	Minimum 99 % aluminum and higher
2xxx (Serie 2000)	Alloys with major alloying element copper
3xxx (Serie 3000)	Alloys with major alloying element manganese
4xxx (Serie 4000)	Alloys with major alloying element silicon
5xxx (Serie 5000)	Alloys with major alloying element magnesium
6xxx (Serie 6000)	Alloys with major alloying element magnesium and silicon
7xxx (Serie 7000)	Alloys with major alloying element zinc
8xxx (Serie 8000)	Alloys with other elements

Aluminum alloys of the 5000 and 6000 series were selected for this work. The properties of the 5000 series are mainly due to the addition of magnesium. They are strain-hardenable but not heat-treatable. The 6000 series alloys contain both magnesium and silicon as the main alloying elements. These combine into magnesium silicide after the solid solution. The alloys of the 6000 series are heat-treatable (KAUFMAN 2000, p. 11). The temper designations of wrought products of aluminum and aluminum alloys are regulated in DIN EN 515. The basic temper designations are listed in Table 2.2.

Table 2.2: Basic temper designations for wrought products of aluminum and aluminum alloys (KAUFMAN 2000, pp. 16 f.)

Designation	Temper
F	As fabricated: Wrought or cast products that are produced by shaping processes in which there is no special control utilized over thermal conditions or strain-hardening processes to obtain certain properties.
O	Annealed: Wrought products that are annealed to get the lower strength temper.
H	Strain-hardened: The strength of these products is increased by strain-hardening.
W	Solution heat-treated: These alloys age spontaneously after solution heat treating.
T	Thermally treated to produce stable tempers other than F, O or H: Products that are thermally treated to produce stable tempers.

The letters listed in Table 2.2 are usually followed by one or more numbers that further specify the treatment (DIN EN 515). In this work, alloys with the tempers T6 and H111 were applied. The designation T6 means “solution heat-treated and then artificially aged” (HESSE 2016, p. 20), and the designation H111 indicates “annealed and slightly strain-hardened during subsequent operations such as stretching or leveling” (HESSE 2016, p. 17).

2.3 Friction stir welding

2.3.1 Process sequence

In FSW, the weld is produced through frictional heating and mixing of material in the plastic state using a rotating tool (ISO 25239-1). The tool typically consists of a shoulder, which is pressed against the surface of the workpieces and compresses the weld seam, and of a probe with a smaller diameter than the shoulder, which penetrates the workpieces (COLLIGAN 2010, p. 16). Figure 2.1 depicts the principle of the welding process using the example of a butt-joint.

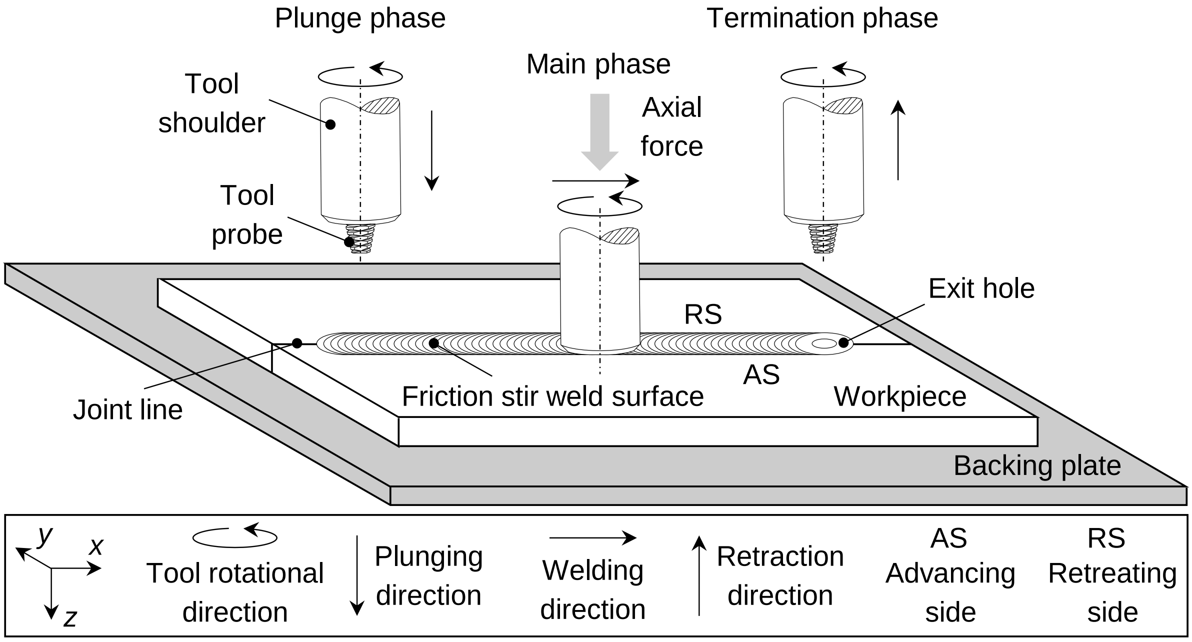

Figure 2.1: Principle of FSW in butt-joint configuration (based on BACHMANN ET AL. 2017)

The FSW process consists of three phases: the plunge phase, in which the welding is initiated, the main phase, in which the weld is produced, and the termination phase, in which the tool is retracted from the workpiece (COLLIGAN 2010, p. 18). The three phases are described in more detail as follows:

- **Plunge phase:** In the plunge phase, the rotating welding tool is inserted into the joint. For this purpose, the tool probe is axially pushed into the workpiece with a specified speed or force. Through frictional heating and pressure, the workpiece material is shifted and forms a ring of plasticized material around the probe. The heat generated is conducted into the surrounding material and the backing plate. Usually it is necessary to dwell at the plunge point for a certain time to reach a sufficiently high temperature in the welding tool and the workpiece. (COLLIGAN 2010, p. 18)
- **Main phase:** As soon as the feed starts, the tool is moved along the joint line, generating heat through friction and plastic work. This maintains sufficient softening in the workpiece, allowing the material to flow around the probe. The process heat is transferred within the workpiece and is utilized to

preheat the material ahead of the tool (COLLIGAN 2010, p. 19). Due to the superposition of the translational and rotational movement of the welding tool along the joint line, an asymmetrical weld is formed (THREADGILL ET AL. 2009, p. 49). The side of the weld where the tool's rotational direction (tangential component) coincides with the welding direction is called the advancing side (AS), and the side of the weld where the tool's rotational direction (tangential component) is opposite of the welding direction is called the retreating side (RS; ISO 25239-1).

- **Termination phase:** When the welding tool reaches the end of the welding trajectory, the forward movement is stopped, the tool is retracted from the workpiece and an exit hole remains at the end of the weld (COLLIGAN 2010, p. 19).

2.3.2 Weld seam characteristics

The interaction between the tool and the workpiece results in a characteristic weld seam pattern. As illustrated schematically in Figure 2.2 (a), the joining zone can be divided into four areas (MISHRA & MAHONEY 2007, p. 2, COLLIGAN 2010, p. 17):

- **Base metal (BM):** This is material remote from the weld, which is neither deformed nor affected by heat, both in terms of microstructure and mechanical properties. However, it may have been subjected to heat during the welding process.
- **Heat-affected zone (HAZ):** In this area, which is closer to the weld seam center than the BM, sufficient heat has been introduced into the material that usually changes the microstructure and the mechanical properties. Plastic deformation does not occur in this region.
- **Thermomechanically affected zone (TMAZ):** In this area, the material was/is plastically deformed by the FSW tool and the process heat causes a thermal influence on the material. For aluminum, it is possible to achieve a considerable plastic strain in this zone without recrystallization.
- **Nugget:** This expression relates to the completely recrystallized area in the weld seam center, where the welding probe was previously positioned.

The weld seam surface is composed of the weld face in the center and the flash on the two edges of the weld (ISO 25239-1). A characteristic feature of the friction stir weld surface is the formation of semicircular arcs (XU & DENG 2008). According to JENE ET AL. (2008), the distance between these visible marks, which are generated by the tool shoulder, usually corresponds to the set feed per revolution. Figure 2.2 (b) depicts a friction stir weld surface containing clearly visible semicircular arcs.

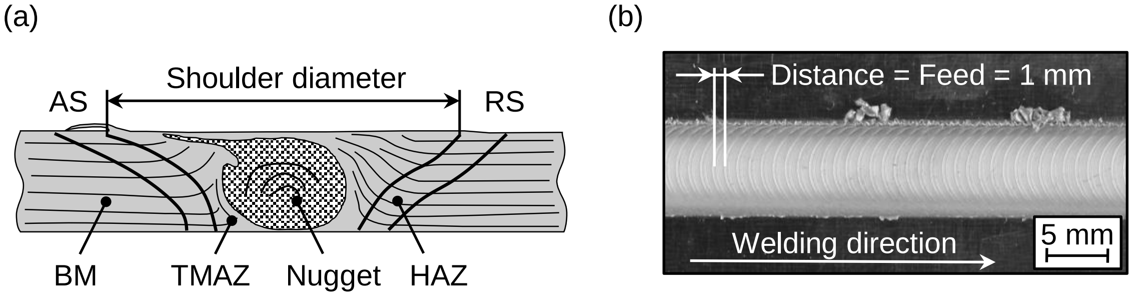

Figure 2.2: (a) Division of the joining zone into four areas (based on R*OTH 2016, p. 6); (b) surface of a friction stir weld with clearly visible semicircular arc texture (based on* G*EBHARD 2011, p. 59)*

The feed per revolution f_{rev} is calculated as (GEBHARD 2011, p. 59)

$$f_{\text{rev}} = \frac{v}{n}\,, \tag{2.1}$$

with the welding speed v and the tool rotational speed n (RPM rate). In the weld depicted in Figure 2.2 (b), the welding speed was 1500 mm/min, and the tool rotational speed was 1500 min^{-1}, which resulted in a feed per revolution of 1 mm. Furthermore, the theoretical number of semicircular arcs n_{theoret} within a certain weld seam length l is

$$n_{\text{theoret}} = \frac{n}{v} \cdot l\,. \tag{2.2}$$

There is a variety of possible weld defects in FSW and different ways to categorize them. In the ISO 25239-5 standard, the irregularities are divided into surface imperfections, internal imperfections, and root flaws. It is stated that the surface imperfections can be detected by visual inspection. According to the standard ISO 25239-4, a 100 % visual inspection of finished friction stir welds is a mandatory part of the welding procedure specification to meet the requirements for the qualification of the welding process. ZETTLER ET AL. (2010, pp. 247 – 265) divided the causes of defects in FSW into defects from welding at excessively high temperatures, defects from welding at insufficient temperatures, and defects caused by geometrical mistakes. In the following paragraphs, several important defects that may occur in friction stir welds are described in more detail. Since the automated detection of surface defects is a major part of this thesis, these are described in particular. Figure 2.3 contains images of weld defects and properties that can be detected by visual inspection.

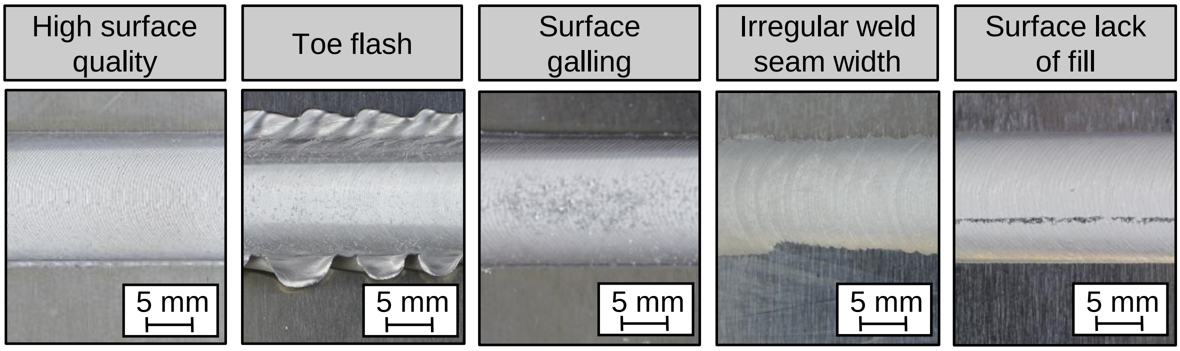

Figure 2.3: Images of friction stir weld seam surfaces

- **Toe flash:** The material that cannot be held in the joining zone by the tool shoulder is expelled from the joining zone and deposited next to the weld face as a toe flash (ISO 25239-1). A small welding flash is a characteristic of an FSW seam and is not yet a defect (Roth 2016, p. 10). But if the heat input into the workpiece gets too high due to, for example, an excessively high tool rotational speed, a large amount of material is displaced, because the removed material can no longer offer sufficient resistance to the tool (Kim et al. 2006). Flash can always be removed by applying a post welding process such as milling. Its impact on mechanical properties tends to be negligible, unless it is accompanied by an excessive seam underfill (Smith & Hinrichs 2011, p. 265).
- **Excessive seam underfill:** A seam underfill occurs due to a tool shoulder that plunges into the weld zone and displaces material from the weld seam (Huggett 2017, p. 72). Underfill may or may not constitute a weld defect, which depends on its amount (Smith & Hinrichs 2011, p. 264). One possible calculation rule for the acceptable quantity of underfill u is provided in ISO 25239-5 as

$$u \leq 2\,\mathrm{mm} + 0.1 \cdot t_\mathrm{S} \,, \tag{2.3}$$

  whereby t_S is the sheet thickness (see Figure 2.4 (a)). Since the seam underfill is usually only a few tenths of a millimeter deep, a visual inspection will normally not reveal whether the underfill is acceptable or too pronounced. One cause for the formation of an excessive seam underfill can be a too large axial force for the excessively softened material in the process zone. In general, the tensile strength of the friction stir weld decreases with increasing seam underfill, due to the resulting local thinning of the workpiece (Huggett 2017, pp. 89 – 92).
- **Surface galling:** Surface galling occurs when the axial force on the tool is too low and the tool rotational speed is too high. Consequently, the material in the immediate vicinity of the tool shoulder is sheared off from the rest of the material and insufficiently compressed due to the reduced axial force (Voellner 2010, p. 22). According to Widener et al. (2008), surface galling has a significant effect not on the tensile strength but on the fatigue behavior.
- **Irregular weld seam width:** When this defect occurs, the weld seam has an irregular shape at the edges, and the weld seam width is often smaller than the shoulder diameter. Voellner (2010, p. 64) suspected that the main cause of this defect is an insufficient axial force.

- **Surface lack of fill:** The surface lack of fill, also called surface void or surface-breaking cavity, usually appears as a crack along the welding direction and results from a too low axial force, inadequate process parameters, an unsuitable tool geometry or gaps between the workpieces (Smith & Hinrichs 2011, p. 264).
- **Cavity:** Cavities, also called wormholes or internal voids, are not visible from the surface (Smith & Hinrichs 2011, p. 264). Cavities usually extend over longer distances or even the entire weld seam length (Voellner 2010, p. 20). They can occur in various sizes d_c (see Figure 2.4 (b)) and quantities. Large cavities can sometimes be noticed by viewing the exit hole or a simple saw cut. However, smaller ones can only be identified by preparing and examining a metallographic sample. The reasons for occurring cavities are similar to those of the surface's lack of fill (Smith & Hinrichs 2011, p. 264).

Figure 2.4: Schematic depiction of (a) a seam underfill and (b) a cavity (based on ISO 25239-5)

The effects of these defects can range from negligible to significant. Thus, for a defect to be assessed critical, it must have considerable negative effects regarding the application of the welded part. Production control plans should indicate the acceptable limits of each of the potential defects (Smith & Hinrichs 2011, p. 266). For this purpose, in the ISO 25239-5 standard, a concept using three acceptance levels for the evaluation of the weld quality has been introduced.

2.3.3 Process characterization

The FSW process is subject to a large number of input variables, which determine the welding result (Mahoney 2007, p. 71). Figure 2.5 provides a non-exhaustive overview of input variables, output variables, and process variables for FSW. Usually, the disturbance variables cannot be controlled. The other input variables can be subdivided according to whether they can be adjusted only in the preparation of the welding process (offline) or also during the welding process (inline). Similarly, the process output variables can be divided into whether they are measurable only offline subsequent to the process or also inline during the process (Roth 2016, pp. 12 f.).

Depending on the control mode, that is, the position control or force control, the plunge depth p_d and the axial force F_z can either be an input variable or a process variable (Smith 2007, p. 232). Since the process parameters were widely varied in the studies conducted for this thesis, the position-controlled mode was the more reliable strategy to prevent damage to the welding system or the measuring equipment. Consequently, the plunge depth p_d is to be regarded as an input variable and the axial force F_z as a process variable.

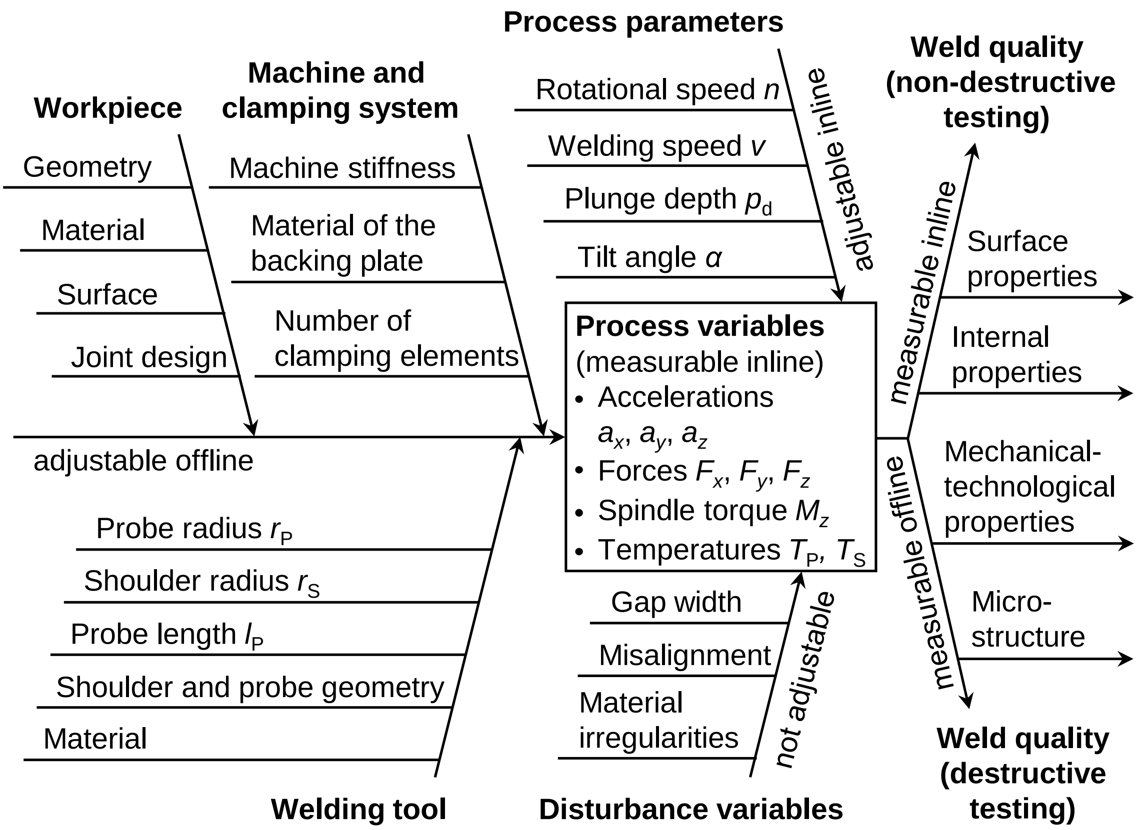

Figure 2.5: Variables for a position-controlled FSW process in butt-joint configuration (based on Zappia 2010b, p. 187, Roth 2016, p. 13, and Mishra et al. 2018)

Offline adjustable input variables

Workpiece: The geometry, the material properties, and the surface conditions of the components to be joined as well as the joint design, have a decisive influence on the FSW process (Zappia 2010b, pp. 185 – 187). In practice, these properties are usually predefined and can only be changed to a limited extent (Roth 2016, p. 13).

Machine and clamping system: Depending on the workpiece and the resulting process requirements, a suitable machine and a clamping system must be selected (Zappia 2010a, p. 74). The material of the backing plate, which serves to withstand the high axial forces F_z, also has a significant influence on the thermal boundary conditions on the bottom side of the weld and thus on the heat balance in the weld (Bachmann et al. 2017). Appropriate clamping elements must be used to ensure that the joining partners cannot bulge or move relative to each other (Zappia 2010a, p. 99). If the FSW process is to be transferred to another welding system, the machine stiffness plays an important role and must be taken into account in particular when determining the axial force F_z or the plunge depth p_d of the tool (Zaeh & Gebhard 2009).

Welding tool: The welding tool has a direct influence on the process as a central component in FSW (Zappia 2010b, p. 186). In comparison to the machine and the clamping system, the tool can be varied with less effort and thus represents an important input variable for the FSW process that can be adjusted offline (Roth 2016, p. 14). Figure 2.6 illustrates a principle sketch of the welding tool and the FSW process. The most important parameters of the tool geometry are the probe radius r_P, the probe length l_P, and the shoulder radius r_S (Smith 2007, p. 221). According to Fuller (2007, p. 25), for the r_S/r_P ratio, a range from two to three is usually applied. To improve and regulate the material flow and thus produce defect-free, high-quality welds, the probe and the shoulder front side are often provided with additional geometric features:

- The probe typically has a conical shape to reduce the process forces in the *z*- and *x*-directions.
- The material flow around the probe can be increased by laterally flattening the probe, and a downward material flow is facilitated by a thread on the probe.
- The tool shoulder can also contain features such as spiral-shaped channels or a concave profile to raise the amount of material deformation caused by the tool shoulder.

In addition to the tool geometry, the tool material is an important factor, as it must withstand the high thermal and mechanical loads during the process (Fuller 2007, pp. 7 – 19). Tool steel is generally acceptable as material both for the shoulder and the probe for FSW of aluminum alloys (Colligan 2010, p. 28).

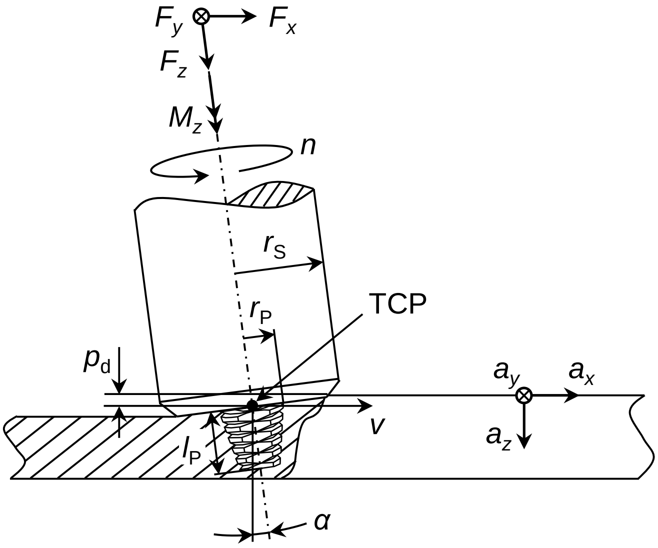

Figure 2.6: Principle sketch of the welding tool and the FSW process in a longitudinal section through the weld seam (based on Ruhstorfer 2012, p. 8)

Inline adjustable input variables

The inline adjustable input variables are of particular importance as they can be altered prior and during the welding process. They are usually referred to as process parameters (Roth 2016, p. 16). The tool rotational speed *n* and the welding speed *v* are considered the most relevant process parameters. The tilt angle α and either the plunge depth p_d for position-controlled operation or the axial force F_z for force-controlled operation are further relevant process parameters (SIDHU & CHATHA 2012). In industrial applications, the process parameters are typically determined through trial and error or by manufacturers' experience (RAJAKUMAR ET AL. 2010).

Rotational speed: The speed at which the tool rotates is the most significant factor influencing the welding temperature for a given tool geometry (RECORD ET AL. 2004, p. 14). The higher the rotational speed n is, the more frictional heat is generated and the higher is the welding temperature (ZETTLER 2010, p. 57). In addition to the heat generation, the tool rotational speed n has a major influence on the material flow around the probe (SCHMIDT & HATTEL 2005).

Welding speed: In fusion welding processes, the power input and the welding speed are independent of each other, making it straightforward to control the line energy. According to WILLIAMS & STEUWER (2010, p. 232), the line energy is defined as the energy input per unit of the weld seam length. In contrast, this relation is different in the FSW process. Here, due to the direct mechanical contact between the tool and the workpiece, the welding speed v influences the line energy as well as the power introduced into the workpiece (COLEGROVE ET AL. 2007). The power input increases with rising welding speed at a fixed rotational speed of the tool, while the line energy declines with a rising welding speed. The far-field temperature depends more on the line energy than it does on the power input, whereas the power is more decisive for the maximum welding temperature (REYNOLDS 2007, p. 60).

Plunge depth: In this thesis, the plunge depth p_d refers to the distance by which the tool center point (TCP) is pressed into the workpiece (see Figure 2.6). According to ROTH (2016, p. 17), the TCP is the point of intersection of the tool axis with the shoulder plane. The actual plunge depth can be less than the adjusted plunge depth and depends on the stiffness of the machine and the clamping system (GEBHARD 2011, pp. 54 f.). The plunge depth and the axial force are closely coupled to each other (GEBHARD 2011, p. 114).

Tilt angle: The tilt angle α is the angle of inclination of the tool axis against an axis perpendicular to the welding direction and the workpiece surface. It affects the immersion depth of the shoulder's rear edge and consequently also the axial force (ROTH 2016, p. 17). A tilt angle between 1.5° and 3.0° is typically selected to increase the process stability during FSW (SMITH 2007, p. 222).

Non-adjustable input variables

Non-adjustable input variables are disturbance variables that cannot be fully influenced by the user or can only be affected with increased effort. Improper selections of these variables can have a negative effect on the FSW process and the resulting weld quality (ROTH 2016, p. 22). Non-adjustable input variables include geometric irregularities in the joining zone, such as a gap or a linear misalignment, and irregularities in the material prior to welding, such as cavities and fluctuations in mechanical properties, as well as tool wear (ZAPPIA 2010b, pp. 185 f.). In this thesis, it was tried to keep the influence of the disturbance variables as low as possible, for example, by geometrically clamping the workpieces as precisely as possible to avoid geometric irregularities.

Process variables

Process variables that can be measured inline during the process include, among others, the accelerations a_x, a_y, a_z, the process forces F_x, F_y, F_z, the spindle torque M_z, and the temperatures at the tool probe T_P and the tool shoulder T_S. Methods for non-destructively monitoring the friction stir weld quality can be classified into *direct* and *indirect* techniques. The evaluation of the process variables to correlate them with weld properties corresponds to the latter. These are less accurate than direct methods are, but they are economically and practically more suitable for industrial application, because they are only little dependent on environmental impacts such as the illumination or dust formation in the production area (MISHRA ET AL. 2018). Industrial systems for monitoring the process variables are primarily based on the definition of threshold values that must not be exceeded or undercut (ZAPPIA 2010b, p. 189).

Accelerations: Accelerations and vibrations can be measured by means of acceleration sensors, displacement sensors, or velocity sensors. Mostly, however, accelerometers are used to measure the mechanical vibration based on the piezoelectric effect (MISHRA ET AL. 2018). These were also employed for the work conducted for this thesis. According to MISHRA ET AL. (2018), low-frequency events can be classified well by evaluating acceleration signals, but the prediction of transient phenomena such as weld defects or mechanical properties is difficult. PANZER ET AL. (2018) discovered that acceleration measurements are a suitable instrument to identify friction stir welds with an irregular surface and thus may be a method for inline process monitoring of the weld surface quality. The acceleration sensors should be positioned as closely as possible to the process.

Forces: During the welding process, the forces F_x, F_y, and F_z act on the tool from the machine side (see Figure 2.6). Thereby, F_x is the force to push the FSW tool through the material in the welding direction, F_y is the force perpendicular to the welding direction in the plane of the workpiece surface, and F_z is the force on the tool in its axial direction (SMITH 2007, p. 231). According to SMITH (2007, p. 232), it is highly recommended to implement a force monitoring strategy for FSW, because it can help to detect changes in the FSW tool condition, incorrect or defective parts, missing parts, and weld quality variations.

The axial force F_z that occurs along the rotational axis of the tool is of major importance for the FSW process. During the plunge phase, it results from the resistance of the material against the penetration by the tool. In the main phase, F_z is the force required to maintain contact between the tool shoulder and the weld surface. Therefore, the axial force F_z in conjunction with the tool shoulder has a significant influence on the compression of the weld and thus on its quality. (ROTH 2016, pp. 18 f.)

Spindle torque: In addition to the process forces, which result from the translational movement of the tool, a torque M_z also acts on the tool due to the tool rotation (LOHWASSER & CHEN 2010, p. 3). The spindle torque is closely related to the material flow and the welding temperature. Disturbances in the material flow lead to weld defects and become evident in the form of changes in the resulting required torque M_z. Therefore, the required spindle torque M_z offers the possibility to monitor and control the weld quality (ARBEGAST 2007, p. 280). The spindle torque and the process forces can be measured indirectly via the motor currents of the machine spindle and the moving machine axes (MEHTA ET AL. 2013). Alternatively, direct measurement is also possible with the aid of suitable sensors mounted either on the tool or the workpiece side. According to SMITH (2007, p. 232), the direct method of measurement provides a higher accuracy than the indirect method does.

Temperatures: The welding temperature is a thermal process variable that depends on the heat input by friction between the tool and the workpiece as well as the dissipation during the plastic deformation of the material. The dominant heat generation mechanism is determined by the process parameters, the tool geometry, and the thermal conductivities of the workpiece, the tool, and the backing plate. When selecting the process parameters, it is common sense that empirically high welding temperatures correlate with high tool rotational speeds n and low welding speeds v. Conversely, low welding temperatures correspond to low tool rotational speeds n and high welding speeds v (SCHNEIDER 2007, p. 37). On the one hand, the welding temperature must be high enough to adequately soften the material in the immediate vicinity of the tool and to ensure a sufficient material transport around the probe, yielding defect-free welds (SHERCLIFF & COLEGROVE 2007, p. 187). On the other hand, the process parameters must be selected such that the welding temperature is as low as possible to prevent thermal damage of the material and the resulting reduction of the mechanical properties (ROTH 2016, p. 20). Due to the self-regulating behavior of the FSW process with regard to the heat input, the maximum welding temperature usually remains below the solidus temperature of the workpiece material (WILLIAMS & STEUWER 2010, p. 232). QIAN ET AL. (2013) calculated the optimum welding temperature for faultless welds for a range from 80 % to 90 % of the material solidus temperature (percentages are based on absolute temperatures in K). As a measuring method for determining the welding temperature, the integration of thermocouples into the tool probe or the tool shoulder has proven to be suitable for research purposes (NISHIHARA & NAGASAKA 2004).

Inline measurable output variables

Direct methods for non-destructively monitoring the weld quality are based on techniques such as triangulation, camera vision, ultrasonic waves, or radiography (MISHRA ET AL. 2018). Some direct methods to determine the weld seam properties can be performed inline during the welding process (PIETRAS & WEGLOWSKI 2014).

Surface properties: Surface properties of friction stir welds can be determined based on appearance or topography. The surface appearance of welds can be examined by a human visual inspection or by an automated visual inspection:

- **Human visual inspection:** This is the most straightforward and simplest technique to inspect friction stir weld surfaces. It can be used to inspect for features such as toe flash, surface galling, or surface lack of fill (cf. Subsection 2.3.2), which are visible to the naked eye (ZAPPIA 2010b, p. 196). Disadvantages of a human visual inspection are, for example, that the observations depend on personnel experience and that the eyes fatigue with increasing testing duration (ZAPPIA 2010b, p. 210).
- **Automated visual inspection:** The most important components for an automated visual inspection system are the exposure unit, the camera, the lens, and the computer containing a suitable software. Two common types of semiconductor sensors for cameras are charge-coupled device (CCD) and complementary metal oxide semiconductor (CMOS) sensors. These convert light into electric currents. The pixels are arranged either in a line (line scan camera) or in a matrix (area scan camera) (KEFERSTEIN & MARXER 2015, pp. 179 – 185).

Two frequently used principles for recording the weld topography are the light-section method and the structured light projection, which are both based on the technique of triangulation:

- **Light-section method:** A low-power laser passes through a pattern generator, and the resulting laser plane is projected onto the weld surface. This creates a laser stripe that follows the surface profile of the weld. The laser light is reflected from the weld surface and scattered in different directions. A CCD or CMOS image sensor is applied to record the reflected laser light. The distance between the image sensor and the weld surface as well as the lateral position and the geometric surface characteristics of the weld, can be precisely determined on the basis of mathematical relations in the micrometer range. (HUANG & KOVACEVIC 2011)
- **Structured light projection:** Projected stripes are used to lay several light sections over the workpiece, which are captured by an image sensor from a different direction. The narrower the stripes are, the more accurate is the height resolution. The shape of the workpiece influences the shape of the line patterns. From the distorted line patterns, which are recorded by the image sensor, the geometry of the workpiece, that is, a point cloud with a high point density, can be calculated (KEFERSTEIN & MARXER 2015, p. 235). This technique was utilized in the work conducted for this thesis.

Internal properties: For the identification of internal irregularities in friction stir welds, methods such as ultrasonic testing or X-ray testing are usually employed offline in a post-weld process (TAHERI ET AL. 2019). Ultrasonic testing of friction stir welds is also possible inline (HUGGETT 2017, p. 157). It uses high-frequency sound waves to perform the investigations. The main factor limiting the inline application of ultrasonic testing for FSW is the uneven weld surface. For this reason, the ultrasonic testing is mostly performed by accessing the weld from the root side or after a surface finishing step such as milling or grinding (TAHERI ET AL. 2019).

Offline measurable output variables

The output variables that must be measured after the joining process include all weld properties that can only be determined by destructive testing methods (MISHRA ET AL. 2018). According to the ISO 25239-4 standard, for butt-joints of aluminum wrought alloys, mechanical-technological tests as well as macroscopic tests are particularly relevant.

Mechanical properties: For this thesis, the tensile strength, the elongation at break, and the Vickers hardness of friction stir welds were determined. These mechanical properties are described in more detail below:

- **Tensile strength:** The tensile strength R_m is a characteristic value of the tensile test on metallic materials (ISO 6892-1). It is calculated from the maximum force occurring during the tensile test in relation to the initial cross section of the tensile specimen. Since the reduction of the initial cross section due to lateral contraction is not taken into account, the tensile strength R_m is the so-called *technical tension*, which is smaller than the *actual tension* (KOPAS ET AL. 2017). The ISO 25239-4 standard recommends considering the ISO 4136 norm, which describes the specimen geometry and production for the transverse tensile test of butt-joints. The determined tensile strength gives information about the load capacity of the weld seam in comparison to the BM (ROTH 2016, p. 21).
- **Elongation at break:** In contrast to the tensile strength, other characteristic values determined in the tensile test, such as the elongation at break, are not suitable for comparing the weld seam with the BM. During the transverse tensile test, the test load is applied transversely to the weld, so that all areas of the weld, which are the BM, the HAZ, the TMAZ, and the nugget (see Figure 2.2 (a)), are in the force flux. Due to the different microstructures in these areas, the tensile test specimens are stretched differently in the individual zones. Consequently, the measured total elongations for the welded tensile specimen cannot be meaningfully compared with the elongation of a non-welded tensile specimen. However, if the specimen dimensions and the weld seam widths are identical, the elongations at break of different welded tensile specimens can be compared among each other (VOELLNER 2010, p. 18). Strains during the tensile test can be determined by using optical systems such as laser extensometers (CONIGLIO 2008, p. 5).
- **Vickers hardness:** Hardness tests of friction stir welds are usually conducted on cross sections perpendicular to the welding direction at the midpoint line across the weld zone and also extend into the BM to allow a comparison of the hardness profile in the weld with the hardness of the BM (MOREIRA ET AL. 2009). Especially the measurement of the Vickers hardness is suitable for friction stir welds, since the hardness values may vary considerably and unsteadily in the various weld seam areas (SUENGER ET AL. 2014). The shape of the hardness curve over the cross section of the FSW seam depends strongly on the aluminum alloy (strain-hardenable or heat-treatable) and on the temper condition (cf. Section 2.2). Most friction stir welds in heat-treatable alloys welded in the T6 temper,

for example, EN AW-6082-T6, exhibit a characteristic W-shaped hardness profile. Friction stir welds of strain-hardenable alloys in the H temper, for example, EN AW-5754-H111, usually have a constant but lower hardness profile in the weld compared to the BM (THREADGILL ET AL. 2009, p. 66).

Microstructure: In addition to mechanical-technological testing methods, welded joints can also be evaluated optically using a metallography specimen. The most common method is to prepare a cross section according to the ISO 17639 standard. A micrograph allows the evaluation of the internal weld structure and thus a characterization with regard to geometric features such as the weld penetration depth, the grain sizes, the width of the weld seam zones, and internal weld seam defects such as cavities. (VOELLNER 2010, p. 20)

2.4 Artificial intelligence, machine learning, and deep learning

2.4.1 Overview of machine learning methods

The idea of AI dates back to the 1950s, when pioneers in the emerging field of computer science, such as TURING (1950) and ROCHESTER ET AL. (1956), began to wonder if computers could be made to "think." A succinct definition of AI is "the effort to automate intellectual tasks normally performed by humans." As such, AI is a wide-ranging field that includes ML and deep learning (see Figure 2.7), but also many other areas such as robotics and natural language processing (KREUTZER & SIRRENBERG 2020, p. 23). (CHOLLET 2018, p. 4)

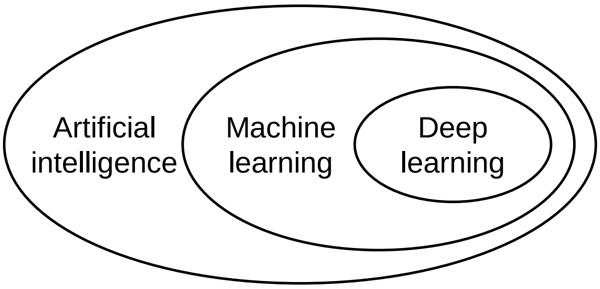

Figure 2.7: Relation between AI, ML, and deep learning (CHOLLET 2018, p. 4)

The AI algorithms utilized in this thesis belong to the field of ML. An ML system gets predominantly trained instead of explicitly programmed. It is exposed to many training examples, and finds a statistical structure in the examples. This finally allows the system to establish rules for automating the task. Although ML did not begin to thrive until the 1990s, it has since rapidly evolved into the most popular and successful branches of AI. This trend is spurred by the availability of more powerful hardware and larger data sets (CHOLLET 2018, pp. 5 f.). There are many different types of ML systems; consequently, it is useful to classify them into categories. One frequently chosen approach for this categorization is the degree of human supervision that is required to train the ML system. The four corresponding categories are *supervised learning*, *unsupervised learning*, *semi-supervised learning*, and *reinforcement learning* (RL; GÉRON 2017, p. 8):

- **Supervised learning:** In supervised learning, the training data for the algorithm includes both the inputs and the outputs of the ML system, whereby the outputs are called labels (GÉRON 2017, p. 8). The application example for the recognition and marking of cracks in sheet metals (cf. Section 1.1) can be assigned to the group of supervised learning, since all training images were available with labels. The two main goals in supervised learning are *classification*, which aims to assign the input data to different categories, and *regression*, which is intended to predict a real value or vector associated with the input. The simplest case for classification is binary classification, in which there are only two classes. In the introductory use case from Audi AG, the classification could be *crack* or *non-crack*. Further examples are classifying an email as *spam* or *non-spam* or an image as *face* or *non-face* (KWOK ET AL. 2015, pp. 497 f.). Although supervised learning is mostly applied for classification and regression, there are other variants as well. One example is *object detection*, whose aim is to draw one or more *bounding boxes* around specific objects within the image. This can also be formulated as a classification problem, where there are many potential bounding boxes and the contents of each one must be classified. It can also be considered as a combination of a classification and a regression problem, whereby the bounding box coordinates are predicted by regression (CHOLLET 2018, p. 94).
- **Unsupervised learning:** This group of ML methods aims to find useful transformations of the input data without any need of labels, for example, for data visualization, data compression, or a better sense of the correlations inherently present in a data set. (CHOLLET 2018, p. 94)
- **Semi-supervised learning:** Some algorithms can cope with partially labeled training data, which typically contain mainly unlabeled data and only a small amount of labeled data. This is referred to as semi-supervised learning. They are in most cases a combination of unsupervised and supervised algorithms. A prominent example for semi-supervised learning is Google Photos (Google LLC, Mountain View, CA, USA): After uploading photos that contain faces, it is automatically recognized that the same person shows up in other images. Thus, only one label per person is necessary, and the service is able to name each person in all the photos. (GÉRON 2017, p. 13)
- **Reinforcement learning:** In RL, a self-learning system, which is called an agent, observes the environment and selects and executes actions based on the observations. Depending on the result of the action, the agent receives a reward or a penalty. It has then to learn by itself what the best strategy is, called a policy, to achieve the highest reward or the lowest penalty over time. Which action the agent should select when it is in a certain situation is specified by the policy (GÉRON 2017, p. 13). A frequently mentioned use case for RL is a robot vacuum cleaner, which should find a suitable strategy to vacuum as much dust as possible in an apartment in a certain time (GÉRON 2017, p. 440).

Deep learning is a specific subarea of ML (CHOLLET 2018, p. 8). It is a type of ML that can process a wider range of data resources, often requires less human data pre-processing, and delivers more accurate results compared to traditional ML approaches for many applications (KREUTZER & SIRRENBERG 2020, p. 8). Modern deep learning often involves a large number of successive layers, all of which are automatically trained through exposure to data. These layered representations are nearly always learned using ANNs (CHOLLET 2018, p. 8). Deep learning can be applied in each of the four categories mentioned above, but supervised learning is by far the predominant application of deep learning (CHOLLET 2018, p. 95).

The overall process of discovering useful knowledge from data is often referred to as knowledge discovery in databases (KDD). The KDD process is iterative and involves several steps. The main steps are illustrated in Figure 2.8. An important step is the data mining, that is, the application of specific algorithms to extract patterns from data. The additional steps, such as data selection, data pre-processing, and correct interpretation of the data mining results, ensure that valuable knowledge is derived from the data. (FAYYAD ET AL. 1996)

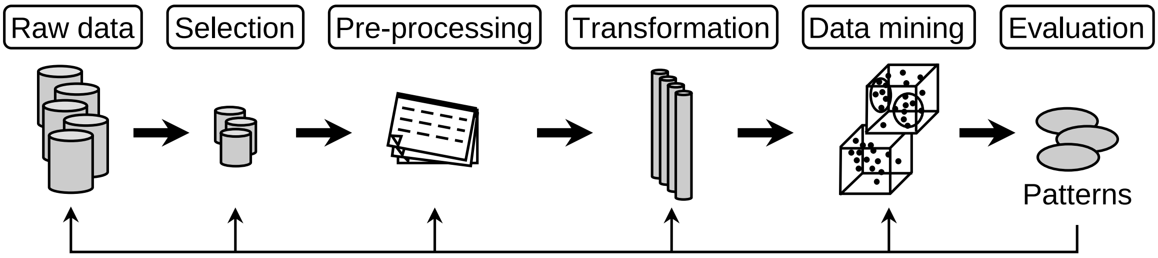

Figure 2.8: Overview of the steps constituting the KDD process (based on FAYYAD ET AL. 1996)

2.4.2 Artificial neural networks

ANNs are the central element of deep learning. The *perceptron*, which was invented by ROSENBLATT (1958), is one of the simplest ANN architectures. It is based on an artificial neuron referred to as a *linear threshold unit* (GÉRON 2017, pp. 253 – 257). Figure 2.9 (a) shows a schematic illustration of the perceptron model (TINO ET AL. 2015, p. 456): The inputs are multiplied by corresponding weights, summarized, and shifted by a bias. The output of the neuron is then calculated by passing the sum through a non-linear function, which is called the activation function. This process can be described by the equation (RUSSELL & NORVIG 2016, p. 728)

$$y_i = f(\sum_{j=1}^{N_i} w_{j,i} \cdot x_{j,i} + b_i)\,, \tag{2.4}$$

where y_i is the output, $x_{j,i}$ is the j-th input, $w_{j,i}$ is the weight for the j-th input, b_i is the bias (offset), and N_i is the total number of inputs for the i-th neuron. The operator f represents the activation function.

The perceptrons' capabilities are limited to linear calculations. To overcome this limitation, several perceptrons can be connected such that the output of one perceptron is the input for the next one. This leads to a multi-layer perceptron, which is composed of several layers of perceptrons. An example with three layers is illustrated in Figure 2.9 (b), where the first layer operates as the input layer, the second layer is a hidden layer, and the third layer serves as an output layer. In this way, a multi-layer perceptron is able to handle more complex functions than a simple perceptron is. (GÉRON 2017, pp. 259 – 261)

The most straightforward form of neural networks is *feed-forward networks*, in which each neuron is only connected to neurons in adjacent layers and the signal passes only in the direction from the inputs to the outputs (GÉRON 2017, p. 263). In case each neuron in a layer receives an input from every neuron in the previous layer, the network is called a *fully connected neural network* (FCNN; FORSYTH 2019, p. 377).

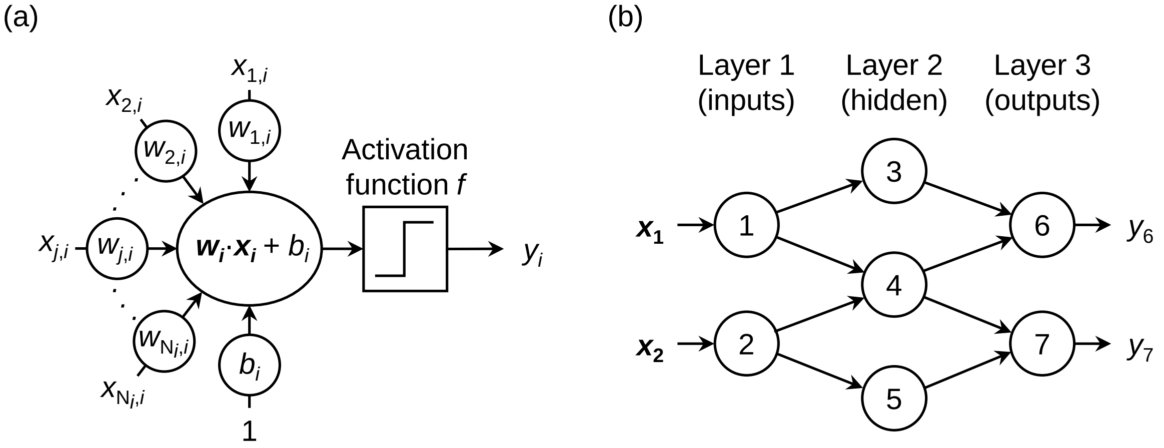

Figure 2.9: Schematic illustrations of (a) the perceptron model (based on TINO ET AL. 2015, p. 456) and (b) a multi-layer perceptron with seven neurons, arranged in three layers (based on GÉRON 2017, p. 261)

Besides the layers, the input data, and the corresponding targets, further important elements for the training of an ANN are the loss function and the optimizer. In Figure 2.10, it is illustrated how these components interact. The ANN, which consists of several layers, receives input data and makes predictions. The loss function then compares these predictions with the true targets and generates a loss value according to the loss function. The loss function is the objective function to be minimized during training. The loss value is a measure of how well the ANN's predictions match the true targets. The fundamental trick in deep learning is that this loss value is used by the optimizer to adjust the weights, whereby the goal is to find the right values for the weights. (CHOLLET 2018, pp. 10 f. and pp. 58 – 60)

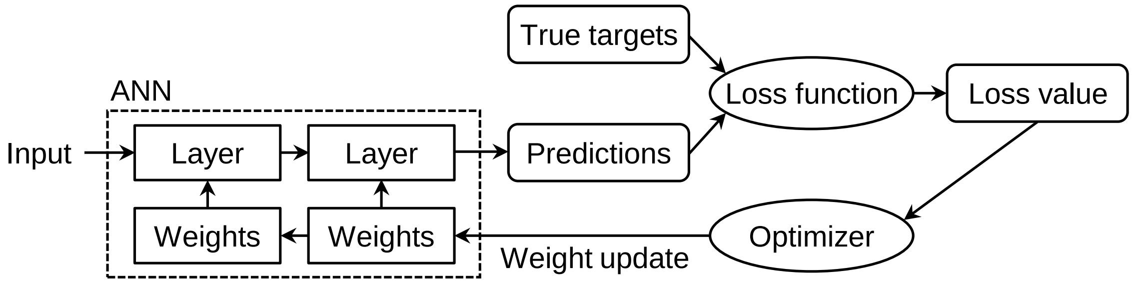

Figure 2.10: Connection between the ANN, the loss function, and the optimizer (based on CHOLLET 2018, p. 58)

The standard learning algorithm, which is implemented by the optimizer, is called back-propagation (RUMELHART ET AL. 1986). The difference between the predictions and the true targets is propagated backward through the network, and the weights are adjusted based on a gradient-descent method.

To further improve the learning process of ANNs, a number of techniques are usually applied (GUENTHER 2018, p. 36). Three frequently applied methods are listed below:

- **Value normalization:** If the input data for the ANN are of relatively large values or rather heterogeneous, this can trigger large gradient updates that will impede the network from converging. To facilitate the training process, it is common to normalize the data to have a mean of 0 and a standard deviation of 1. (CHOLLET 2018, pp. 101 f.)
- **Mini-batch:** Training samples are typically provided in batches to accelerate the training process and to improve the convergence (COTTER ET AL. 2012). The number of samples in a batch is often a power of two to simplify the memory allocation on the graphics processing unit (GPU). During training, a batch is utilized to calculate a single gradient-descent update for the weights of the ANN (CHOLLET 2018, p. 96). Each iteration across all the training data is referred to as an epoch (CHOLLET 2018, p. 53).
- **Data augmentation:** This is the approach for creating more training data from existing training samples. The number of samples is increased by using random transformations that lead to similar data. For example, by transforming the replicated images, such as by cutting or flipping them, the ANN is not provided with exactly the same image twice during training. As a result, the neural network is exposed to different aspects of the data and is able to generalize better. The risk that the model fits too closely to the training data and merely mimics the training data by "learning by heart," which is referred to as *overfitting*, is reduced. (CHOLLET 2018, p. 139)

Convolutional neural networks

In convolutional neural networks (CNNs), not all layers are fully connected, which means that the neurons in one layer are not connected to all neurons in neighboring layers but only to a small subset of neurons. This leads to the fundamental difference that convolutional layers learn local patterns, whereas fully connected layers learn global patterns. In particular, images can be divided into local patterns such as edges and textures, which makes CNNs suitable for image pattern recognition (CHOLLET 2018, p. 122). The two fundamental concepts for changing the connections between the neurons in CNNs are *sparse connectivity* and *parameter sharing* (GOODFELLOW ET AL. 2016, p. 335):

- **Sparse connectivity:** In Figure 2.11 (a), only two neurons are connected to one neuron of the subsequent layer, instead of each neuron being connected to all neurons of the subsequent layer as in a fully connected layer. This leads to fewer parameters. Consequently, less memory is needed, and the statistical efficiency is raised. To indicate that each connection has its own parameters, different types of lines were used for the connecting lines.
- **Parameter sharing:** This idea corresponds to the same parametrization of weights and biases for similar connections between the layers. In the example depicted in Figure 2.11 (b), shared parameters are indicated by the same line type.

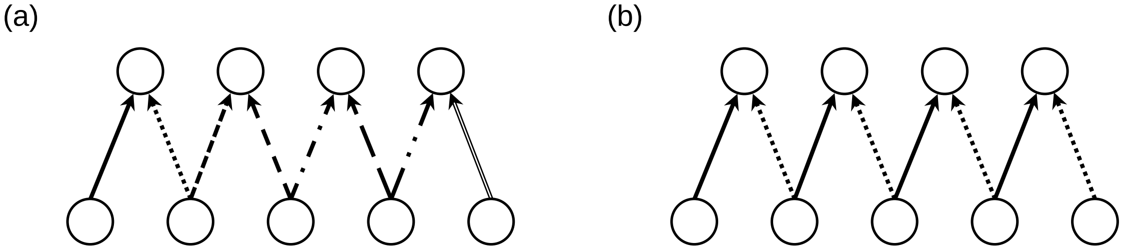

Figure 2.11: Concepts of (a) sparse connectivity and (b) parameter sharing that are fundamental for CNNs (based on GOODFELLOW ET AL. 2016, p. 353)

CNNs perform especially well on data that has a grid-like structure, such as images, which is why a frequent application of CNNs is for computer vision problems (GOODFELLOW ET AL. 2016, p. 330). The two most important types of layers applied in CNNs, convolutional layers and max pooling layers, are described by using examples from the field of image recognition in the following paragraphs.

Convolutional layers are the most essential components of CNNs. Following the concept of sparse connectivity, the neurons in the first convolutional layer are not linked to each individual pixel contained in the input image, but only to the pixels in their receptive fields (see Figure 2.12 (a)). Each neuron in the second convolutional layer is in turn only related to neurons located within a small rectangle in the first convolutional layer. By this architecture, the network is able to focus on simpler features in the initial hidden layers and then combine these simple features into more complex ones in subsequent hidden layers. This hierarchical structure is typical for real-world images, which is a major reason why CNNs perform well for image recognition (GÉRON 2017, p. 355). An illustrative example is given in CHOLLET (2018, p. 123; see Figure 2.12 (b)): the first convolutional layer recognizes smaller patterns such as edges, vertical lines, or horizontal lines. The next convolutional layer already recognizes local objects, such as eyes or ears, which are later combined, and the cat is recognized.

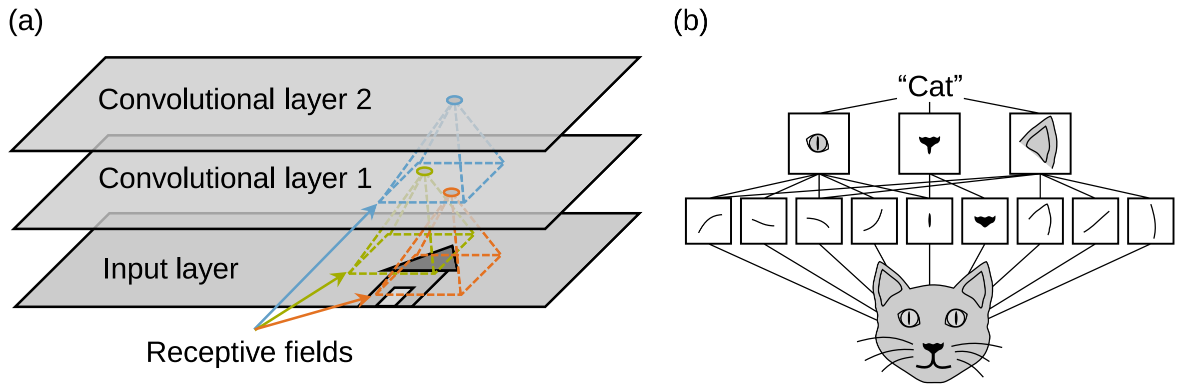

Figure 2.12: (a) CNN layers with rectangular local receptive fields (based on GÉRON 2017, p. 356); (b) principle of the hierarchical structure applied in CNNs for the recognition of complex patterns (based on CHOLLET 2018, p. 123)

Following the concept of parameter sharing, the weights of the neurons in a convolutional layer can be mapped as a small image of the size of the receptive field. This small image is called a filter or convolutional kernel. During the training of the CNN, the filter values are optimized (GÉRON 2017, pp. 357 f.). Typical filter sizes are 3 × 3 or 5 × 5 (CHOLLET 2018, p. 124). The filter is sequentially shifted across the width and height of the input of the convolutional layer, whereby the dot product between the input and the filter is calculated. This operation is known as convolution. Figure 2.13 (a) displays an example containing the input of a convolution layer, a filter of the size 3 × 3 containing the set of weights, and the result of the dot product that is entered into the output, which is called a feature map (FORSYTH 2019, pp. 402 f.). The result of the dot product for this example is

$$2 \cdot (-1) + 8 \cdot 0 + 9 \cdot 1 + 1 \cdot (-2) + 5 \cdot 0 + 4 \cdot 2 + 8 \cdot (-1) + 3 \cdot 0 + 2 \cdot 1 = 7 \quad . \tag{2.5}$$

Max pooling layers are the second essential component for CNNs, besides convolutional layers. In max pooling layers, within a given size of the max pooling mask, only the pixels with the highest value are reported to the next layer in the CNN (see Figure 2.13 (b)). This procedure has two functionalities (GOODFELLOW ET AL. 2016, pp. 339 – 442):

- **Representation invariance:** It creates an invariance to small changes of the input, such as translation or rotation. Within the max pooling mask, the pixel with the highest value can alter its position without changing the response of the ANN (GUENTHER 2018, p. 39).
- **Data compression:** The input of the next layer is compressed depending on the size of the max pooling mask. This improves the computational efficiency. Additionally, the statistical efficiency can be improved, and less memory may be necessary.

The most common size of the max pooling mask is 2 × 2. In Figure 2.13 (b), an example of a max pooling mask with a size of 2 × 2 is illustrated. A stride of two is used, which means that the filter is shifted by two pixels per operation. Consequently, the output block is half the size of the input block. (FORSYTH 2019, p. 408)

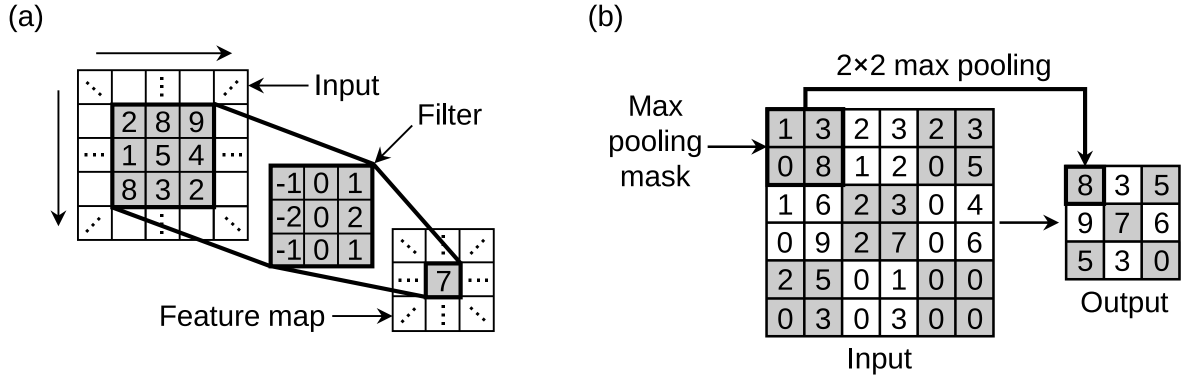

Figure 2.13: (a) Sliding the 3 × 3 filter over the input (e. g. an image) to produce a feature map (based on FORSYTH 2019, p. 403); (b) exemplary 2 × 2 max pooling layer with a stride of two (based on GUENTHER 2018, p. 39)

The first CNN that caught significant attention from the computer vision community was AlexNet (KRIZHEVSKY ET AL. 2013, FORSYTH 2019, p. 428). Since then, CNNs have won all major computer vision competitions. In some cases, human-like performance has been achieved or human capabilities in accomplishing certain tasks have even been exceeded (CIRESAN ET AL. 2013). CNNs are also used for object detectors, which means that, given an image, a so-called *bounding box* is drawn around certain objects contained in the image (CHOLLET 2018, p. 94). The performance of object detectors is usually evaluated using the intersection over union (IOU), which is computed by dividing the area of overlap by the area of the union between the ground-truth bounding box and the predicted bounding box (FORSYTH 2019, p. 445):

$$\mathrm{IOU} = \frac{\text{Area of overlap}}{\text{Area of union}} \quad . \tag{2.6}$$

The ground-truth bounding box is the manually placed bounding box that specifies where within the image the object is located (CHOLLET 2018, p. 96). The predicted bounding box is determined by the CNN-based object detector. Figure 2.14 shows an example each of a rather low (≈ 41 %) and a rather high (≈ 82 %) IOU for the detection of the friction stir weld in the image. Popular CNN-based object detectors are *region-based CNNs* (R-CNN; REN ET AL. 2017b), *single shot detector* (SSD; LIU ET AL. 2016), and *you only look once* (YOLO; REDMON ET AL. 2016).

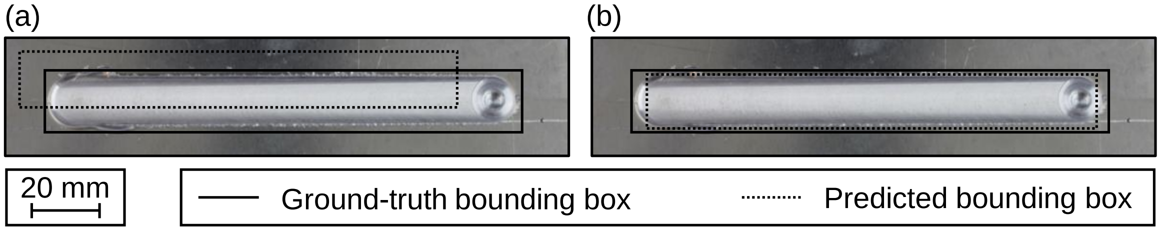

Figure 2.14: Examples of computing IOUs between the ground-truth bounding box and the predicted bounding box: (a) low IOU (≈ 41 %); (b) high IOU (≈ 82 %) (based on REN ET AL. 2017a)

Recurrent neural networks

A recurrent neural network (RNN) resembles a feed-forward neural network, except that it also has backward connections. The simplest RNN is composed of one neuron, which receives inputs, produces an output, and the output is also sent back to the neuron by a recurrent connection (see Figure 2.15 (a)). At each time step t, the recurrent neuron receives both the inputs x_t and its own output from the previous time step y_{t-1}. The network can be displayed as a graph over the time axis, which is then referred to as "unrolling the network through time" (see Figure 2.15 (b)). Each recurrent neuron has two sets of parameters: one set for the inputs and another set for the outputs of the preceding time step. Since the output of a recurrent neuron at a time step depends on all inputs from earlier time steps, the neuron has a kind of memory. An RNN is capable of receiving a sequence of inputs and generating a series of outputs at the same time, which is why these networks are useful to analyze and predict a time series, for instance. (GÉRON 2017, pp. 380 – 382)

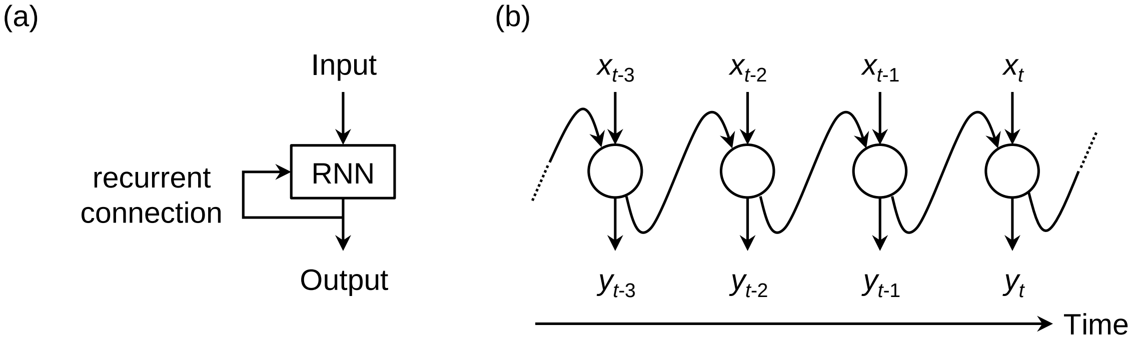

Figure 2.15: (a) A recurrent network (based on CHOLLET *2018, p. 196); (b) a recurrent network, unrolled over time (based on* GÉRON *2017, p. 380)*

2.4.3 Gaussian process regression

The class of regression methods can be further divided into *parametric* and *non-parametric* approaches (GÉRON 2017, p. 173):

- **Parametric:** Parametric models, such as linear regressions or ANNs with a fixed number of hidden units (RASMUSSEN & WILLIAMS 2006, p. 166), have a predefined number of parameters, so that their degree of freedom is limited. On the one hand, this reduces the risk for overfitting, but on the other hand it increases the risk that the adaptation is insufficient (underfitting).
- **Non-parametric:** In non-parametric models, the number of parameters is not defined prior to training. Thus, the model structure is more flexible and can be adapted well to the structure inherent in the data. A powerful non-parametric approach for function approximation is the Gaussian process regression (GPR; RASMUSSEN & WILLIAMS 2006, p. 4).

Before the GPR is described, some basics are explained regarding univariate and multivariate normal distributions.

Univariate normal distribution

The normal distribution, which is often also called the Gaussian distribution, is a key element of the GPR. If a continuous random variable x follows a Gaussian distribution with mean μ and variance σ^2, the univariate probability density function of this variable is given by (HEUMANN ET AL. 2016, p. 166)

$$f(x \mid \mu, \sigma^2) = \frac{1}{\sqrt{2\pi\sigma^2}} \exp\left(-\frac{(x-\mu)^2}{2\,\sigma^2}\right), \text{ with} \tag{2.7}$$

$$\mathbb{E}(x) = \mu \text{ , and} \tag{2.8}$$

$$\mathrm{Var}(x) = \sigma^2 \,. \tag{2.9}$$

If x is a Gaussian distributed with μ and σ^2, the notation $x \sim \mathcal{N}(\mu, \sigma^2)$ is common. The probability density function of a Gaussian distribution has its maximum at

$$x = \mu \,, \tag{2.10}$$

and the inflection points are located at (μ-σ) and (μ+σ) (see Figure 2.16 (a)). Therefore, a lower σ indicates a higher concentration around the mean μ, and a higher σ indicates a flatter probability density function (see Figure 2.16 (b); HEUMANN ET AL. 2016, p. 166).

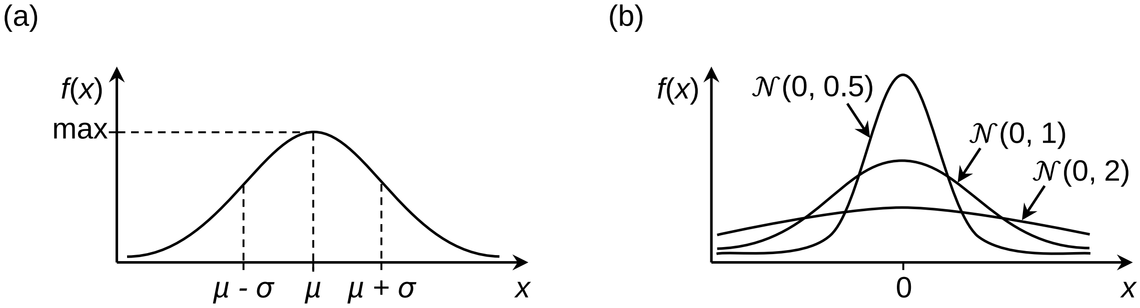

Figure 2.16: (a) Probability density function of a Gaussian distribution; (b) probability density functions of $\mathcal{N}(0, 0.5)$, $\mathcal{N}(0, 1)$, and $\mathcal{N}(0, 2)$ distributions (based on HEUMANN ET AL. 2016, p. 167)

Multivariate normal distribution

The multivariate normal distribution is a generalization of the univariate normal distribution for two or more dimensions d (LABIDI 2010, p. 862). The parameters in a multivariate set include the mean values and the variances of the individual variables x_i as well as the covariances between these variables. If $\boldsymbol{x}$ is a multivariate normal random vector with d dimensions according to

$$\boldsymbol{x} = \begin{pmatrix} x_1 \\ x_2 \\ \vdots \\ x_d \end{pmatrix}, \tag{2.11}$$

denoted $\boldsymbol{x} \sim \mathcal{N}_d(\boldsymbol{\mu}, \boldsymbol{\Sigma})$, then its probability density function is given by

$$f(\boldsymbol{x} \mid \boldsymbol{\mu}, \boldsymbol{\Sigma}) = \frac{1}{|\boldsymbol{\Sigma}|^{1/2}(2\pi)^{d/2}} \exp\left[-\frac{1}{2}\left((\boldsymbol{x}-\boldsymbol{\mu})\,\boldsymbol{\Sigma}^{-1}(\boldsymbol{x}-\boldsymbol{\mu})\right)\right], \tag{2.12}$$

where $\boldsymbol{\mu}$ is the mean vector whose components are the expectations and $\boldsymbol{\Sigma}$ is the variance-covariance matrix whose diagonal terms are variances and off-diagonal terms are covariances (LABIDI 2010, p. 862):

$$\boldsymbol{\mu} = \begin{pmatrix} \mu_1 \\ \mu_2 \\ \vdots \\ \mu_d \end{pmatrix}, \tag{2.13}$$

$$\boldsymbol{\Sigma} = \begin{pmatrix} \sigma_1^2 & \sigma_{12} & \cdots & \sigma_{1d} \\ \sigma_{21} & \sigma_2^2 & \cdots & \sigma_{2d} \\ \vdots & \vdots & \ddots & \vdots \\ \sigma_{d1} & \sigma_{d2} & \cdots & \sigma_d^2 \end{pmatrix}. \tag{2.14}$$

Several properties of a multivariate normal distribution are easier to conceive by studying the bivariate normal surface (KALPIĆ & HLUPIĆ 2011, p. 908). For this reason, the bivariate normal distribution that represents only two dimensions d is considered in the following paragraphs. Thereby, the normal random vector $\boldsymbol{x}$, the mean vector $\boldsymbol{\mu}$, and the variance-covariance matrix $\boldsymbol{\Sigma}$ scale down to

$$\boldsymbol{x} = \begin{pmatrix} x_1 \\ x_2 \end{pmatrix}, \tag{2.15}$$

$$\boldsymbol{\mu} = \begin{pmatrix} \mu_1 \\ \mu_2 \end{pmatrix}, \text{ and} \tag{2.16}$$

$$\boldsymbol{\Sigma} = \begin{pmatrix} \sigma_1^2 & \sigma_{12} \\ \sigma_{21} & \sigma_2^2 \end{pmatrix}. \tag{2.17}$$

In the following first example, the mean values are zero and the variance-covariance matrix corresponds to the identity matrix. The probability density function therefore is

$$f(\boldsymbol{x} \mid \boldsymbol{\mu}, \boldsymbol{\Sigma}) = \mathcal{N}_2(\boldsymbol{x} \mid \boldsymbol{\mu}, \boldsymbol{\Sigma}) \text{, with} \tag{2.18}$$

$$\boldsymbol{\mu} = \begin{pmatrix} 0 \\ 0 \end{pmatrix}, \text{ and} \tag{2.19}$$

$$\boldsymbol{\Sigma} = \begin{pmatrix} 1 & 0 \\ 0 & 1 \end{pmatrix}. \tag{2.20}$$

In this special case, when the variables are uncorrelated, meaning that σ_{12} and σ_{21} are zeros, and σ_1^2 is equal to σ_2^2, the contours of constant probability density are circles (see Figure 2.17; KALPIĆ & HLUPIĆ 2011, p. 908).

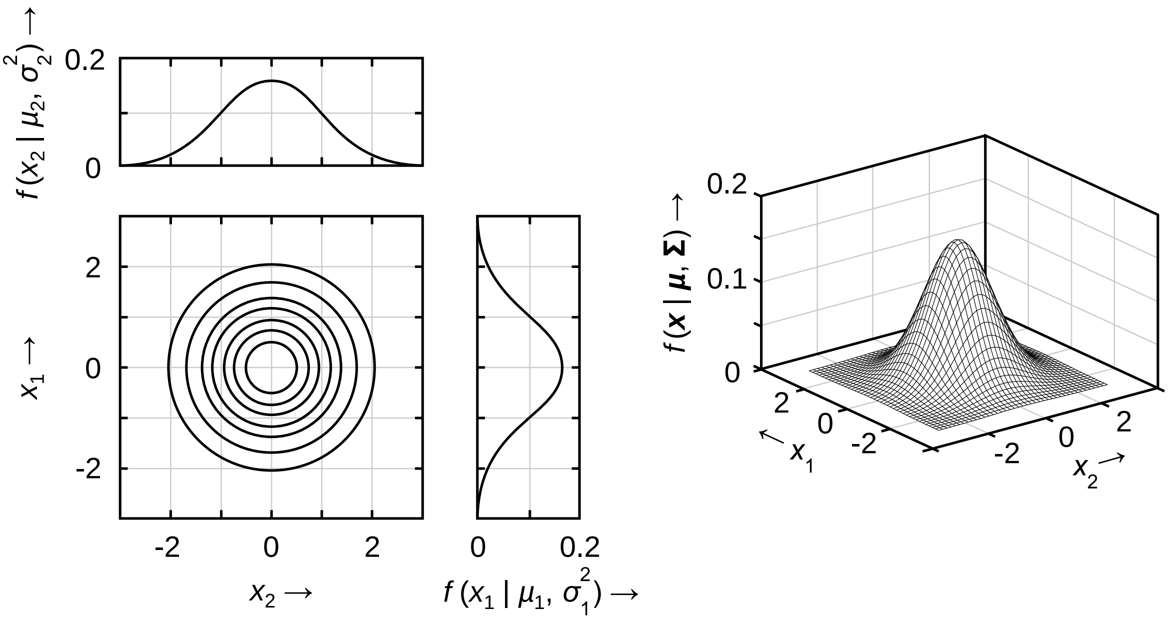

Figure 2.17: Plots of the bivariate Gaussian distribution from Equations 2.18 to 2.20 (based on KALPIĆ & HLUPIĆ 2011, p. 908)

In the presence of a correlation, the contours of constant probability density are ellipses rotated on a plane parallel to the x_1-x_2-plane (KALPIĆ & HLUPIĆ 2011, p. 909). In Figure 2.18 an adequate example is presented. The mean values of the distribution are again set to zero, but the variance-covariance matrix does not correspond to the identity matrix anymore, and the covariance is 0.8:

$$f(\boldsymbol{x} \mid \boldsymbol{\mu}, \boldsymbol{\Sigma}) = \mathcal{N}_2(\boldsymbol{x} \mid \boldsymbol{\mu}, \boldsymbol{\Sigma}) \text{, with} \tag{2.21}$$

$$\boldsymbol{\mu} = \begin{pmatrix} 0 \\ 0 \end{pmatrix} \text{, and} \tag{2.22}$$

$$\boldsymbol{\Sigma} = \begin{pmatrix} 1 & 0.8 \\ 0.8 & 1 \end{pmatrix} . \tag{2.23}$$

If the variable x_1 is additionally conditioned, for example, to the value -1.5, this results in the conditional distribution $f(x_2 \mid x_1 = -1.5)$ with the conditional mean value $\mu_{x_2 \mid x_1 = -1.5}$ of -1.2. Thus, by imposing a bivariate normal distribution on the two variables x_1 and x_2 and then observing x_1, it is possible to calculate which values are likely for the variable x_2. This concept makes it possible to perform predictions and it is fundamental for the GPR (RASMUSSEN & WILLIAMS 2006, p. 2). The described properties are also valid in more than two dimensions d (KALPIĆ & HLUPIĆ 2011, p. 909).

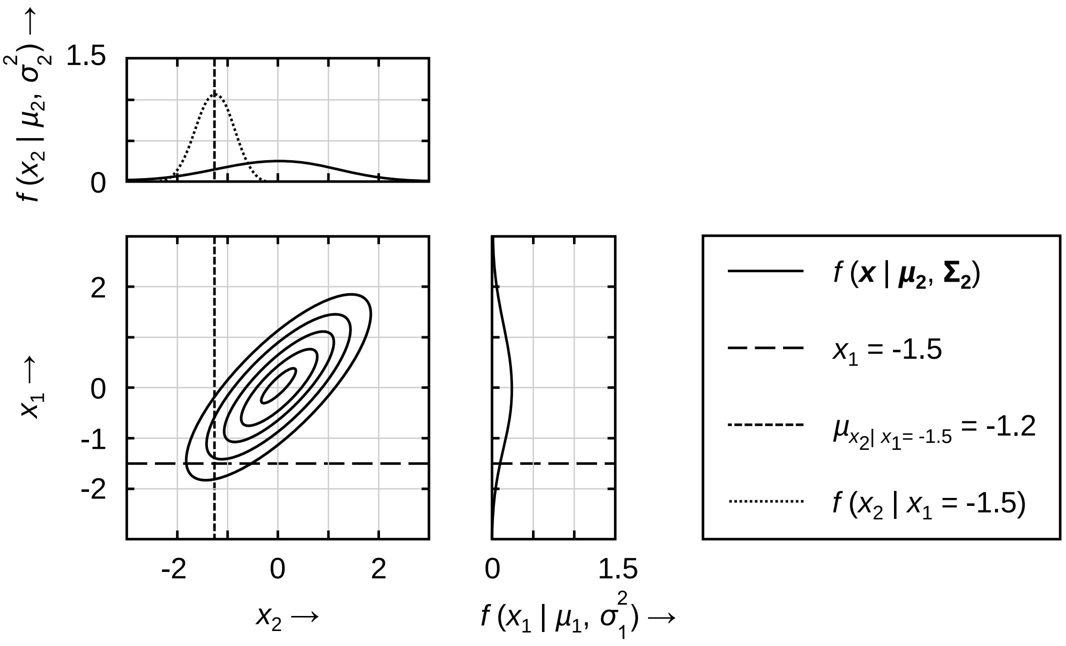

Figure 2.18: *Two-dimensional plots of the bivariate Gaussian distribution with zero means and the variance-covariance matrix differing from the identity matrix; additionally, the conditional distribution $f(x_2 \mid x_1 = -1.5)$ is plotted (based on ZELTERMAN 2015, p. 155, and BENKER 2018, p. 12).*

However, in real applications there are usually more than two observations for one variable. Therefore, as a third example, the function

$$f(\boldsymbol{x} \mid \boldsymbol{\mu}, \boldsymbol{\Sigma}) = \mathcal{N}_5(\boldsymbol{x} \mid \boldsymbol{\mu}, \boldsymbol{\Sigma}), \quad \text{with} \tag{2.24}$$

$$\boldsymbol{\mu} = \begin{pmatrix} 0 \\ 0 \\ 0 \\ 0 \\ 0 \end{pmatrix}, \quad \text{and} \tag{2.25}$$

$$\boldsymbol{\Sigma} = \begin{pmatrix} 1 & 0.65 & 0.18 & 0.02 & 0 \\ 0.65 & 1 & 0.65 & 0.18 & 0.02 \\ 0.18 & 0.65 & 1 & 0.65 & 0.18 \\ 0.02 & 0.18 & 0.65 & 1 & 0.65 \\ 0 & 0.02 & 0.18 & 0.65 & 1 \end{pmatrix}, \tag{2.26}$$

which corresponds to a five-dimensional multivariate distribution is given (WILKINSON 2019). The five dimensions are plotted in Figure 2.19. In the beginning, all variables x_i are expected to be zero, since the mean value $\boldsymbol{\mu}$ is defined accordingly (see Figure 2.19 (a)). Once the variable x_1 is observed to have the value 1.0, the expectations regarding the variables x_2, x_3, and x_4 also change (see Figure 2.19 (b)). Since the initial mean values of the distribution $\boldsymbol{\mu}$ were defined to be zero, the conditional mean values converge towards zero when they distance from the observed data point. The expected value for the variable x_5 does not change yet, since there is no dependence between the variables x_1 and x_5, according to the variance-covariance matrix **Σ** given in Equation 2.26. With observation of x_2 as well, which is 1.5, the expected values of the unobserved variables change again (see Figure 2.19 (c)). Due to the dependence between x_2 and x_5 defined in **Σ**, this time the variable x_5 also changes slightly. This demonstrates the basic concept of the GPR to make predictions about unobserved quantities based on observed values.

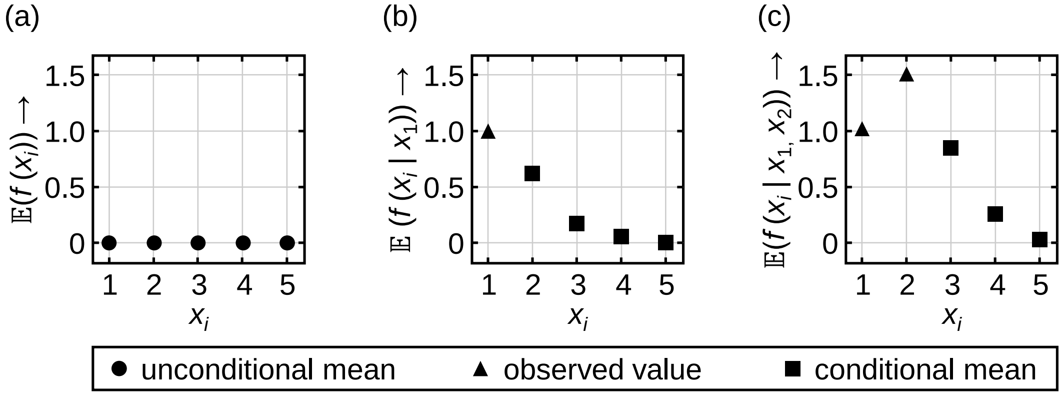

Figure 2.19: *Values of a five-dimensional Gaussian distribution: (a) unconditional mean values $\mathbb{E}(f(x_i)) = \mu_i$; (b) conditional mean values $\mathbb{E}(f(x_i \mid x_1))$ after observation of x_1; (c) conditional mean values $\mathbb{E}(f(x_i \mid x_1, x_2))$ after observation of x_1 and x_2 (based on WILKINSON 2019, p. 12, and BENKER 2018, p. 14)*

Gaussian processes

Gaussian processes (GPs) are a generalization of the multivariate Gaussian distribution and allow the evaluation of a much larger number of inputs. Whereas a probability distribution describes random variables, which are scalars or vectors, a GP can be interpreted as a distribution over functions (RASMUSSEN & WILLIAMS 2006, p. 2). The principle of the GPs is described in the following paragraphs by using the example of a one-dimensional regression problem.

Figure 2.20 (a) displays three sample functions from a prior distribution over functions. A prior distribution represents a set of functions that are expected to be observed before any data is seen. Without any knowledge, it is usually assumed that the mean value of the sample functions at each input x is zero. Although the individual functions do not have a mean of zero, the mean of the function values $f(x)$ for any fixed x would become zero, as more sample functions were added. By calculating the variance, it is also possible to quantify the variability of the sample functions at any value of x. The gray area represents twice the standard deviation for each input value x (corresponding to the 95 % confidence interval). In Figure 2.20 (a), a GP was used, which characterizes that the prior variance does not depend on x. (RASMUSSEN & WILLIAMS 2006, p. 3)

Figure 2.20 (b) illustrates the situation that a data set $\mathcal{D}$, which contains the two observations (x_1, y_1) and (x_2, y_2), is given, and only functions that pass exactly through these two data points are considered. Figure 2.20 (b) displays three sample functions that fulfill this criterion. Additionally, the mean function is provided. The prior distribution in combination with the data set leads to the so-called posterior distribution over functions. Thereby, the uncertainty close to the observations is reduced. If more data points were added, the mean function would be adjusted to pass through these points and the posterior uncertainty would be reduced close to the observations. The probabilistic approach allows the GPR to represent noise in the data and uncertainty about the prediction. (Rasmussen & Williams 2006, p. 3) The sample functions in Figure 2.20 are smooth and stationary. Stationary means that the functions occur similar at all inputs *x*. These are characteristics that are determined by the covariance function of the GP, which is also called *kernel*. Using the training data, suitable properties for the covariance function are searched. (Rasmussen & Williams 2006, p. 4)

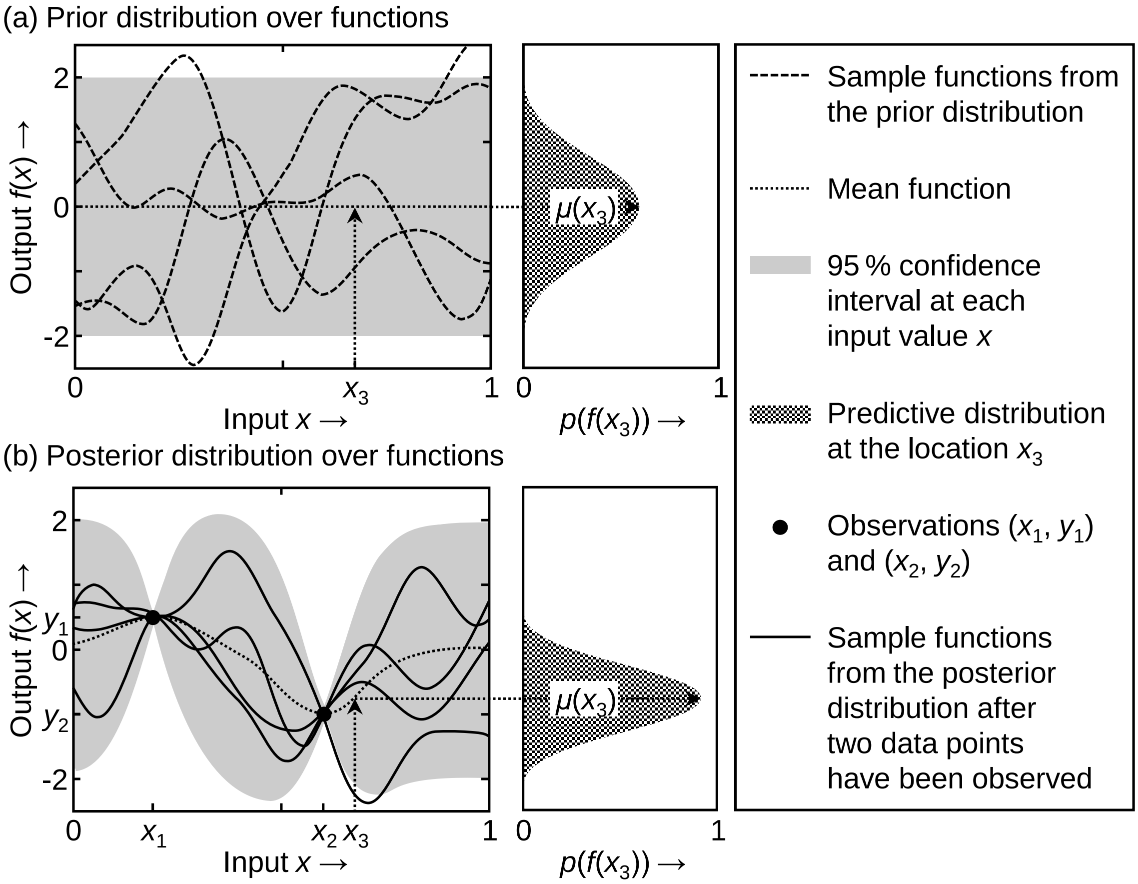

Figure 2.20: (a) Prior distribution with three sample functions; (b) posterior distribution after two data points (x_1, y_1) and (x_2, y_2) have been observed (based on Rasmussen & Williams 2006, p. 3, Deisenroth 2010, p. 18, and Murphy 2017)

A GP is completely defined by its mean function and the covariance function. The mean function $m(\boldsymbol{x})$ and the covariance function $k(\boldsymbol{x}, \boldsymbol{x'})$ of a real process $f(\boldsymbol{x})$, evaluated at the locations $\boldsymbol{x}$ and $\boldsymbol{x'}$, are

$$m(\boldsymbol{x}) = \mathbb{E}[f(\boldsymbol{x})] \quad \text{and} \tag{2.27}$$

$$k(\boldsymbol{x}, \boldsymbol{x'}) = \mathbb{E}\big[\big(f(\boldsymbol{x}) - m(\boldsymbol{x})\big)\,\big(f(\boldsymbol{x'}) - m(\boldsymbol{x'})\big)\big]\,. \tag{2.28}$$

It is common to write the GP as $f(\boldsymbol{x}) \sim \mathcal{GP}(m(\boldsymbol{x}), k(\boldsymbol{x}, \boldsymbol{x}'))$ (RASMUSSEN & WILLIAMS 2006, p. 13). Usually it is impossible to access the function values $f(\boldsymbol{x})$ themselves, but only the noisy version y. Therefore, it is valid that

$$y = f(\boldsymbol{x}) + \varepsilon\,, \tag{2.29}$$

whereby ε is the Gaussian noise. Covariance functions are parameterized by a set of free parameters called hyperparameters $\boldsymbol{\theta}$, whereby different covariance functions have various hyperparameters $\boldsymbol{\theta}$ (RASMUSSEN & WILLIAMS 2006, p. 19). The radial basis function (RBF) is “probably the most widely-used kernel” (RASMUSSEN & WILLIAMS 2006, p. 83). It has the form

$$k(\boldsymbol{x}, \boldsymbol{x}') = \sigma_f^2 \exp\left(- \frac{1}{2l^2}(\boldsymbol{x} - \boldsymbol{x}')^2\right) + \sigma_n^2\, \delta\,, \tag{2.30}$$

with the hyperparameters length-scale l, signal variance σ_f^2, and noise variance σ_n^2 that can be varied. The variable δ is the Kronecker delta. The effects of the different settings of these hyperparameters on the GP are demonstrated in Figure 2.21. The 12 data points in Figure 2.21 (a) were generated using the RBF covariance function and applying the hyperparameters

$$\boldsymbol{\theta} = (l, \sigma_f, \sigma_n) = (1, 1, 0.1)\,. \tag{2.31}$$

For Figure 2.21 (b) and (c), other values were used for the hyperparameters. The length-scale was varied and the remaining two hyperparameters were optimized with respect to the length-scale. In Figure 2.21 (b), the length-scale l is too short and the noise parameter σ_n is reduced to 0.0005. As a consequence, the data points have to be explained by a sharp variation of the underlying function, and the 95 % confidence interval grows rapidly away from the data points. In Figure 2.21 (c), the length-scale l is too long and the noise level σ_n is increased to 0.89. The data is then explained by a slowly varying function with a great deal of noise. (RASMUSSEN & WILLIAMS 2006, p. 21)

Other often utilized covariance functions for ML are the rational quadratic covariance function (RASMUSSEN & WILLIAMS 2006, p. 86) and the Matérn 5/2 covariance function (RASMUSSEN & WILLIAMS 2006, p. 85). There are also approaches to automate the choice of the covariance function (DUVENAUD ET AL. 2013).

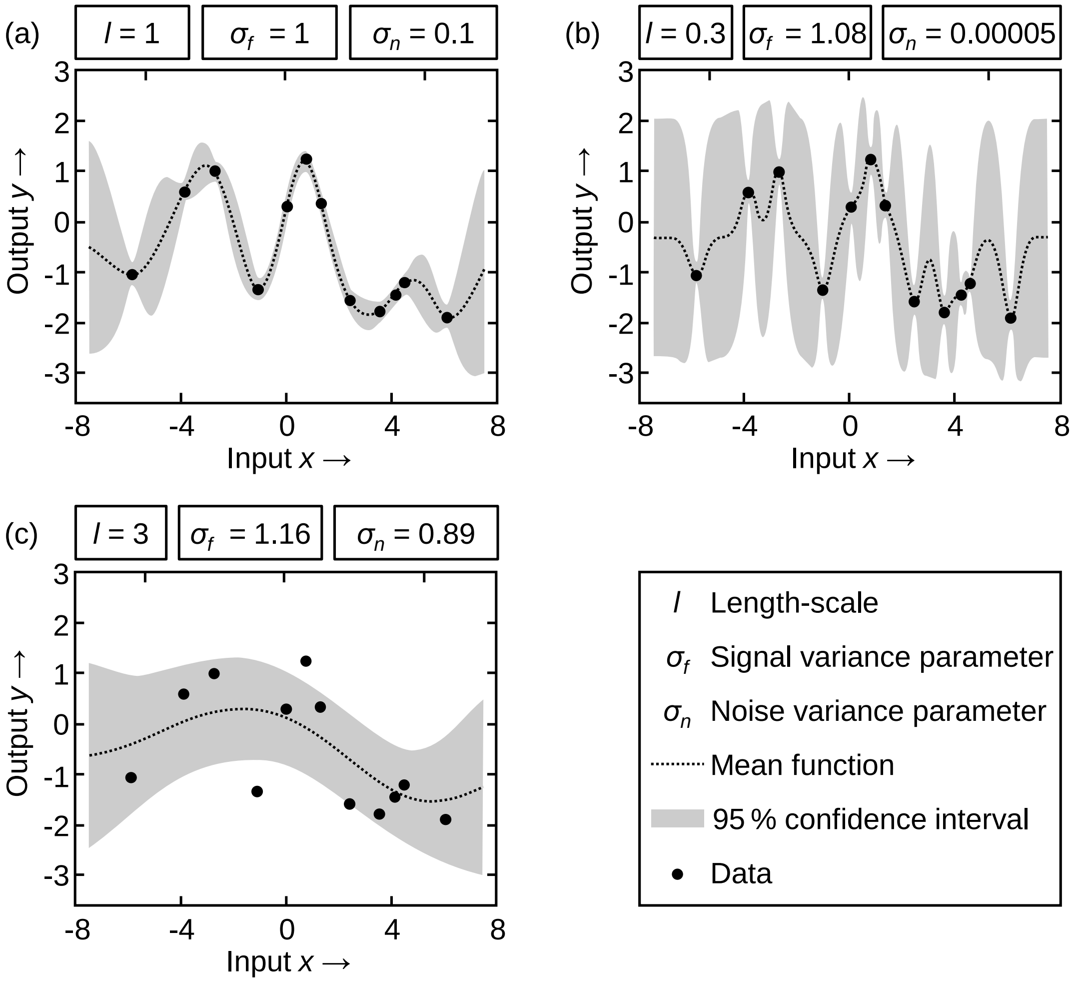

Figure 2.21: Effects of hyperparameters on the GP prediction using the example of the RBF covariance function with (a) a suitable length-scale, (b) a too short length-scale, and (c) a too long length-scale (based on RASMUSSEN & WILLIAMS 2006, p. 20, and MURPHY 2011)

2.4.4 Bayesian optimization

Bayesian optimization (BO) is an approach for the optimization of unknown objective functions, which are “expensive to evaluate” (BROCHU ET AL. 2010). An intuitive example for such a function that is expensive to evaluate is the concentration of oil in reservoirs. Here, the aim of the optimization is to find an area where the oil concentration is high by drilling as few sample wells as possible (WANG & CHEN 2017). The principle of the BO is illustrated in Figure 2.22. Its fundamental aspects are (BROCHU ET AL. 2010):

- The unknown objective function is estimated by a surrogate function.
- The surrogate function and its uncertainty are determined by a GP. In the context of the GP, the surrogate function corresponds to the posterior mean function (see Figure 2.20 (b)).
- A so-called *acquisition function* is calculated from the surrogate function and its uncertainty.

- The next observation from the objective function is placed, where the acquisition function has its maximum.
- The objective function is then observed at the location of the maximum of the acquisition function, the GP is updated, and the procedure is repeated.

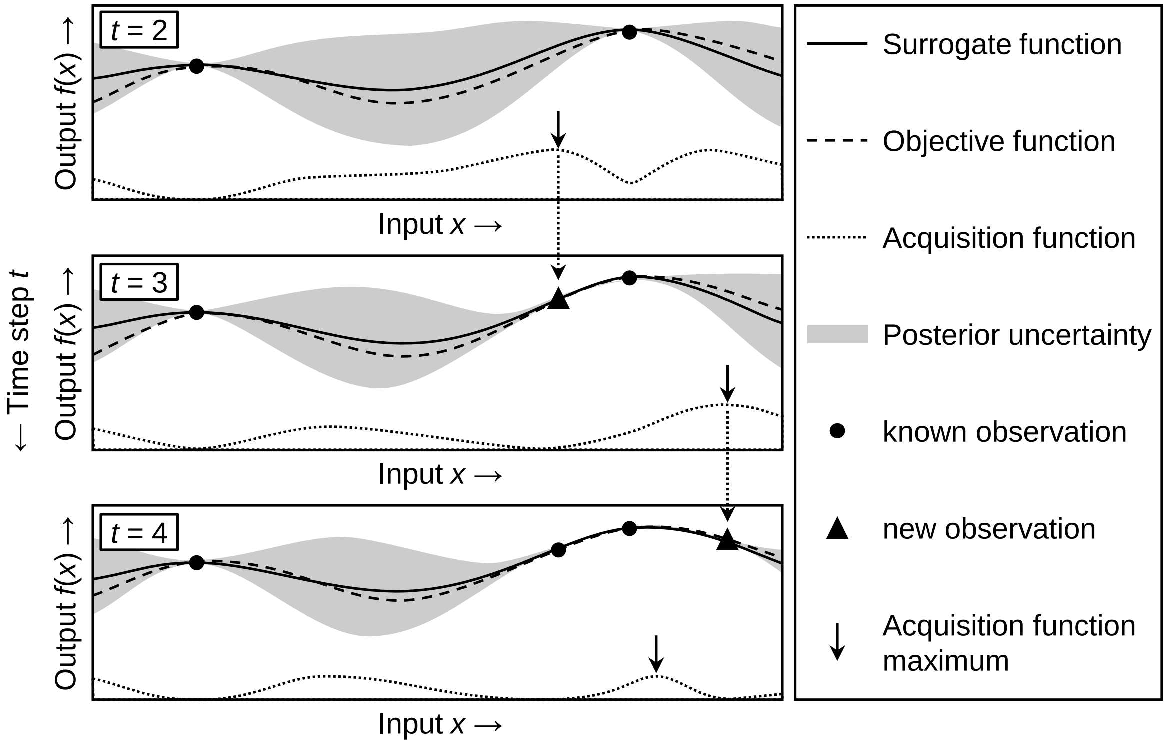

Figure 2.22: Example of using BO for a one-dimensional problem (based on BROCHU ET AL. 2010)

The acquisition function is high, where the GP predicts a high objective and where the prediction uncertainty is high. Areas where both of these attributes apply are observed first. In this way, by BO both the mean and the uncertainty of the predictions are taken into account, and the decision of where to make the next observation thus represents a trade-off between exploitation (where the GP predicts a high objective) and exploration (where the prediction uncertainty is high). The optimization in the one-dimensional example in Figure 2.22 starts with two known observations at the discrete time step two. The area on the far left side remains unobserved in the time steps three and four, because, even though it has a high uncertainty, it is correctly predicted to offer no improvement compared to the highest observation so far. (BROCHU ET AL. 2010)

The trade-off between exploration and exploitation, which the BO deals with, is called the exploration-exploitation dilemma. It is also an important concept in human decision-making: Many decisions that people make, such as which dish to choose in a restaurant or which car to buy, require an analysis of alternatives before people commit to a particular choice and take advantage of its benefits. (COHEN ET AL. 2007)

Two often applied acquisition functions are the *probability of improvement* and the *expected improvement*. While the probability of improvement indicates how likely it is that a new observation will improve the previous optimum, the expected improvement also includes the magnitude of improvement and provides a good balance between exploitation and exploration. (BROCHU ET AL. 2010)

2.4.5 Reinforcement learning

RL is the concept of goal-oriented learning by an agent through interaction with its environment. The agent observes the environment, chooses an action, and in return receives rewards or penalties. The agent seeks to maximize its long-term rewards and thereby is guided towards the goal. The charm of RL is that the agent learns autonomously to achieve the target, while the user only needs to assess how well the goal was achieved (GÉRON 2017, p. 438). Markov decision processes (MDPs) have become the standard formalism to mathematically describe sequential decision-making tasks in stochastic environments, such as RL problems (WIERING & VAN OTTERLO 2012, p. 4). An MDP is defined as follows:

- S: The set of states s in which the environment can be.
- A: The set of actions a, which the agent can perform in the environment.
- $p(s', r \mid s, a)$: The state transition function; thereby, p describes the probability distribution of the successor state s' and the reward r after the agent has executed the action a in the state s.

Figure 2.23 (a) illustrates how the agent interacts with its environment: at the beginning (time step $t = 1$), the agent is in an initial state s_1. At every time step t, the environment is in the state s_t and the agent executes an action a_t. According to the state transition function, the agent changes to the state s_{t+1} at the next time t+1 and gets the reward r_t. By using RL, a policy π is searched, according to which the agent can act in the environment to maximize its reward or minimize its penalties. The policy is supposed to maximize the sum of all expected future rewards. Immediate rewards are typically weighted higher than rewards further in the future (SUTTON & BARTO 2018, pp. 48 – 58).

As already outlined for the BO (cf. Subsection 2.4.4), the RL agent also compromises between exploration, which frequently means acting sub-optimally, and exploitation of its current knowledge to operate locally optimally. A simple example for this behavior is illustrated in Figure 2.23 (b), which is based on DEISENROTH (2010, p. 2). The initial state of the agent is marked by the disk in the upper left corner. The black squares indicate walls, and the numerical values within the squares represent the instant reward when the agent enters this square. Additionally, the arrows show an already found locally optimal path from previous interactions of the agent with the environment, which leads to the highly rewarded region in the lower left corner. Although the path avoids the high-cost squares, resulting in a reward of -20 or -30, it is not globally optimal, as each step of the agent's path results in a reward of -1. This illustrates the exploration-exploitation dilemma: either the agent stays on the current sub-optimal path or explores a new path that might be better but might also lead to one of the high-cost areas. This example also demonstrates that RL usually requires many interactions with the environment to find the best strategy.

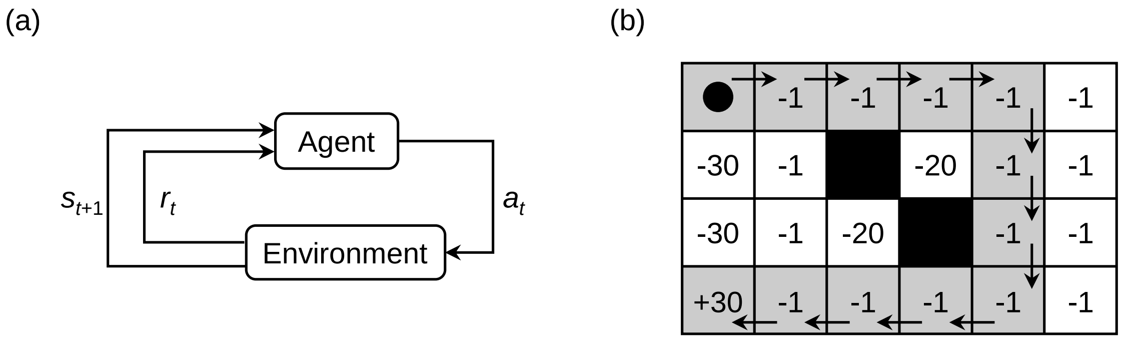

Figure 2.23: (a) The agent-environment interaction in an MDP (based on Sutton & Barto 2018, p. 48); (b) maze as an exemplary environment in which the agent seeks to maximize the reward (based on Deisenroth 2010, p. 3)

Value iteration is an algorithm to find a policy π. It uses an auxiliary function, the value function, which represents the sum of all expected weighted future rewards when the agent follows the policy π. The value iteration algorithm converges towards the optimal value function, that is, towards the optimal policy as well. However, both S and A must be finite because the algorithm iterates over all states s and actions a. (Sutton & Barto 2018, p. 84)

In the field of ML, RL recently received a great deal of attention after the AI enterprise DeepMind Technologies Ltd. (London, England) applied it to play Atari games. However, to date RL is primarily a field of research and has not yet achieved significant practical success beyond games. (Chollet 2018, p. 95)

3 State of the Art

3.1 Chapter overview

This chapter provides an overview of related work of other researchers prior or simultaneous to this thesis work. First, Section 3.2 explains which approaches for the automated detection of surface properties already exist in the field of FSW. The current state of knowledge regarding the evaluation of process parameters and process variables by applying supervised learning methods for the prediction of quality characteristics is described in Section 3.3. Optimization algorithms that have been used up to now in FSW are discussed in Section 3.4. In Section 3.5, it is explained which correlations have already been found between surface properties and mechanical properties of friction stir welds. At the end of the chapter, in Section 3.6, it is deduced which research demand results from the existing state of the art. Some of the related work cited in this chapter has already been described in the six embedded publications (in the paragraphs on the respective state of the art) of this cumulative dissertation.

3.2 Automated surface inspection in friction stir welding

Previous research on the automated detection of surface defects and properties of friction stir welds can be divided into work based on the application of image processing techniques and work that considers the surface topography of the welds. The majority of the publications deals with the former. There are also initial approaches for evaluating images of seam surfaces using ML.

Image processing

SINHA ET AL. (2008) installed a digital camera in a milling machine that had been modified to perform FSW. The camera was positioned behind the welding tool and connected to a computer, which in turn was coupled with a machine control unit. Three cases were considered: a sound weld, a weld produced during a probe failure, and a weld produced with an insufficient probe length. The images were processed offline by using different image processing techniques. Figure 3.1 illustrates the image processing steps conducted by SINHA ET AL. (2008), which were repeated on an own image of a weld that had a good surface quality. The following digital image processing steps were performed by SINHA ET AL. (2008):

- Pre-processing: definition of appropriate regions of interest (ROI) and noise elimination by filtering. In image processing, an ROI allows the definition of arbitrarily shaped areas within an image (usually rectangular). It is often called sub-image, although an ROI can include the entire image if so defined. The ROI is used for further analysis or processing (RELF 2004, p. 85).
- Conversion of the color images to grayscale images (see Figure 3.1 (a) and (b))
- Contrast enhancement through histogram equalization (MUSTAFA & ABDUL KADER 2018) to obtain histograms with a grayscale intensity distribution in the range of 0 to 255
(see Figure 3.1 (c), (d), and (e)).
- Contour plotting, whereby a contour is a path on the grayscale image along which the grayscale values are constant (see Figure 3.1 (f))
- Line plotting, which means plotting the grayscale values of the pixels along a line in the grayscale image (see Figure 3.1 (b) and (g))

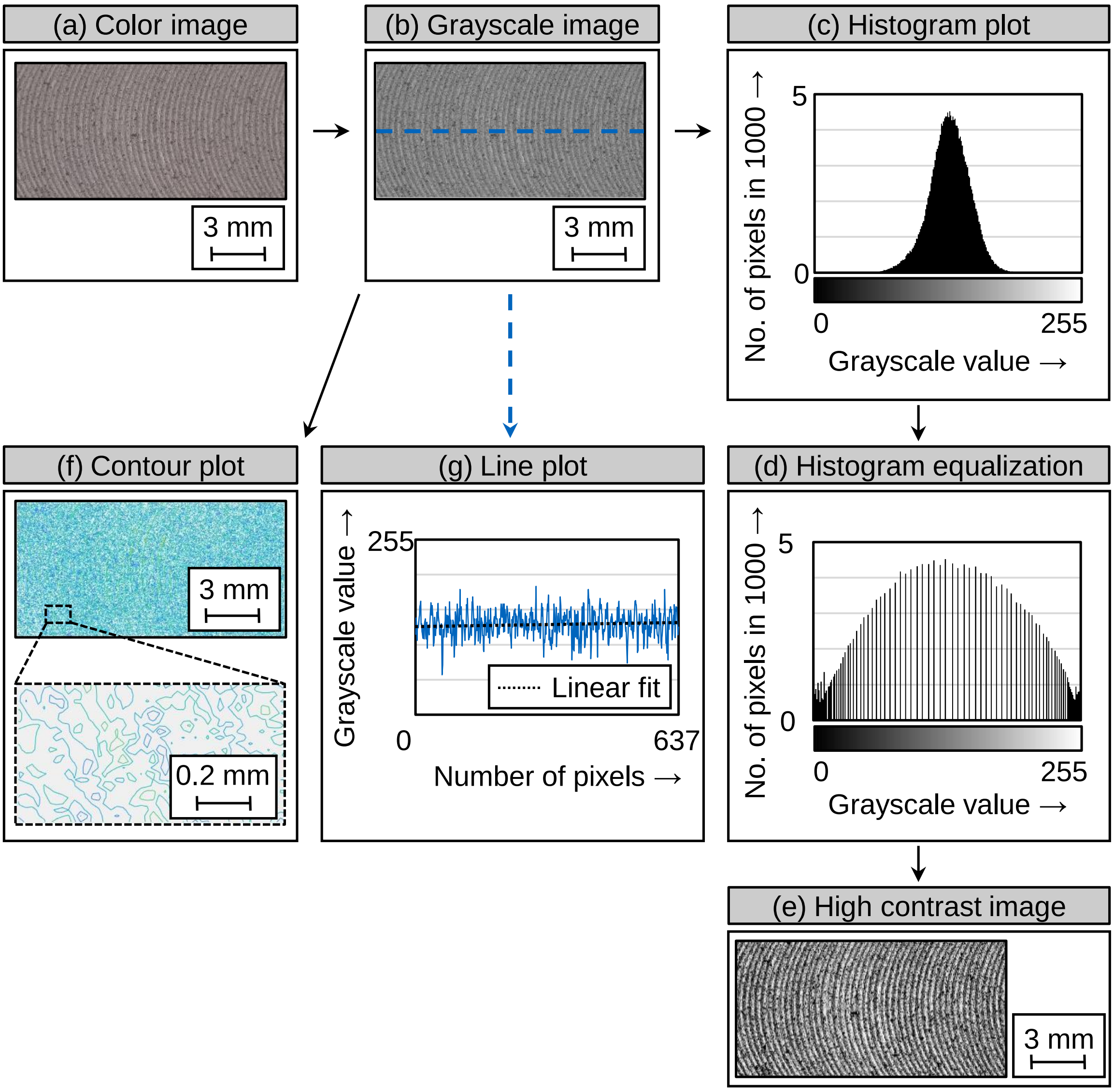

Figure 3.1: Image processing steps performed in SINHA ET AL. (2008) and RAJASHEKAR & RAJAPRAKASH (2013)

Afterwards, a comparative study of the grayscale image, the histogram plot, the contour plot, and the line plot for the three investigated cases (sound weld, probe failure, and insufficient probe length) was conducted:

- For a sound weld, the histogram plot had no pixels below a grayscale value of 50, the contour plot was uniform throughout the weld zone, and the grayscale values in the line plot revealed a low variation.
- In case of a probe failure, the grayscale values in the line plot showed a large variation.
- For an insufficient probe length, the histogram plot revealed grayscale values less than 50, the contour plot was discontinuous over the entire weld zone, and the grayscale values in the line plot revealed a high variation.

It was therefore possible to recognize the three different welding conditions from the image data. The authors concluded the following:

- An online condition monitoring system using a camera and image processing should be employed to evaluate the welding state and the weld quality. This could allow a more flexible automation in the manufacturing process.
- A machine control unit should adapt the process parameters. The proposed system should “learn” to identify the main types of welding defects.
- The recommended online monitoring system could be utilized to estimate process parameters for unknown materials.

However, more detailed information on the implementation of the suggested system was not provided.

RAJASHEKAR & RAJAPRAKASH (2013) extended the approach of SINHA ET AL. (2008). To differentiate the welds into “good” and “defective” ROI, X-ray examinations were conducted. Additionally, a method was developed to quantify the result of the line plot. For this purpose, a linear fit was added in the line plots of the grayscale values along a line in welding direction, and the slope of the linear fit was evaluated (see Figure 3.1 (g)). The slopes were higher for defective welds than for good welds. In Figure 3.1 (g), the slope of the linear fit is almost zero, which, according to RAJASHEKAR & RAJAPRAKASH (2013), indicates a quite good surface quality. Significant demarcations between good and defective ROI were also found in this work for the results of the contour plots and line plots.

SICILAN & KUMAR (2014) also continued the work of SINHA ET AL. (2008). The authors produced seven welds and measured the surface roughness values *Ra* of the welds over a length of 4 mm. It was not explicitly declared at which position of the weld seams the roughness was measured, but it was probably measured along the centerline of the weld in the welding direction. A regression analysis showed a significant connection between the surface roughness *Ra* and the peak values (number of pixels) in the histograms plots derived from grayscale images (see Figure 3.1 (c)). An upward opened quadratic curve achieved a coefficient of determination R^2 of 0.87. The roughness values *Ra* of the FSW specimens were between 4.0 µm and 10.5 µm. The maxima of the pixel numbers for the different grayscale values in the histograms were between 9500 pixels and 16000 pixels. The authors stated that this relation can be applied to detect defects and variations in the weld surface.

RAJASHEKAR & RAJAPRAKASH (2016) processed weld surface grayscale images to quantify the surface texture by evaluating *first order* and *second order* statistical parameters from histogram plots and gray-level co-occurrence matrices (GLCMs; HARALICK ET AL. 1973):

- The first order statistical parameters, which were the *standard deviation* and the *entropy,* were computed from the histogram plots of the grayscale images. The standard deviation measures the average contrast, which is sensitive to both smooth and rough surfaces. The entropy measures the randomness of the surface texture. The value of the entropy is the most important parameter for evaluating banded welds and is higher for a coarse texture than it is for periodic and smooth textures.
- The second order statistical parameters, which were the *contrast* and the *energy*, were computed from the GLCMs. GLCMs indicate how often two gray values occur in an image in a certain arrangement (STEINMETZ & NAHRSTEDT 2002, p. 59). Figure 3.2 shows the gray values of a sample image and the corresponding GLCM for an arrangement [a][b]. In this arrangement, the pixel with the gray value [b] is directly on the right side of the pixel with the gray value [a]. The GLCM in Figure 3.2 reveals how often each pair of gray values occurs in this arrangement in the sample image. For example, the case where [a] has a gray value of 2 and [b] has a gray value of 3 occurs four times.

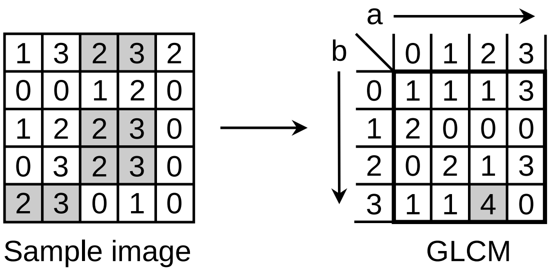

Sample image

1	3	2	3	2
0	0	1	2	0
1	2	2	3	0
0	3	2	3	0
2	3	0	1	0

GLCM

b \ a	0	1	2	3
0	1	1	1	3
1	2	0	0	0
2	0	2	1	3
3	1	1	4	0

Figure 3.2: Gray values of a sample image and the corresponding GLCM for the arrangement where pixel [b] is directly to the right of pixel [a] (based on STEINMETZ & NAHRSTEDT *2002, p. 59)*

The second order statistical parameter contrast measures the difference in intensity between one pixel and one of its adjacent pixels across the entire image and describes the smoothness of the image. The publication does not specify which neighboring pixel was used, but presumably the pixel on the right hand side (as in the example in Figure 3.2), since this is the default setting in Matlab, which was employed for the calculations. For a smooth texture, the contrast value is 0. The energy measures the uniformity of the texture. For a smooth texture, the energy value is 1 (RAJASHEKAR & RAJAPRAKASH 2016).

The variations of these statistical image parameters were evaluated along “good” and “defective” weld regions, whereby the classification into “good” and “defective” ROI was, as in Rajashekar & Rajaprakash (2013), based on X-ray examinations of the welds. The statistical image parameters varied for different ROI, which enabled to define criteria for assessing the weld quality. To validate the results of the image processing procedure, acoustic emission testing data recorded during the welding experiments were evaluated, and statistical parameters were also calculated from the acoustic emission data. The variations of the acoustic emission data were similar to the variations of the applied statistical image parameters. For a shoulder geometry with concentric rings and for a concave shoulder geometry, three intervals were defined for the statistical parameters for both the grayscale images and the acoustic emission data. From the interval, in which the statistical parameters were contained, it could be concluded whether the weld was “defective,” “good with a low tensile strength,” or “good with a high tensile strength.” Figure 3.3 displays the section of the developed evaluation system for the concave shoulder geometry and the intervals for the statistical parameters that indicate a “good weld with a high tensile strength”. The authors state that their machine vision and acoustic emission system was successfully used for a reliable assessment of the weld quality.

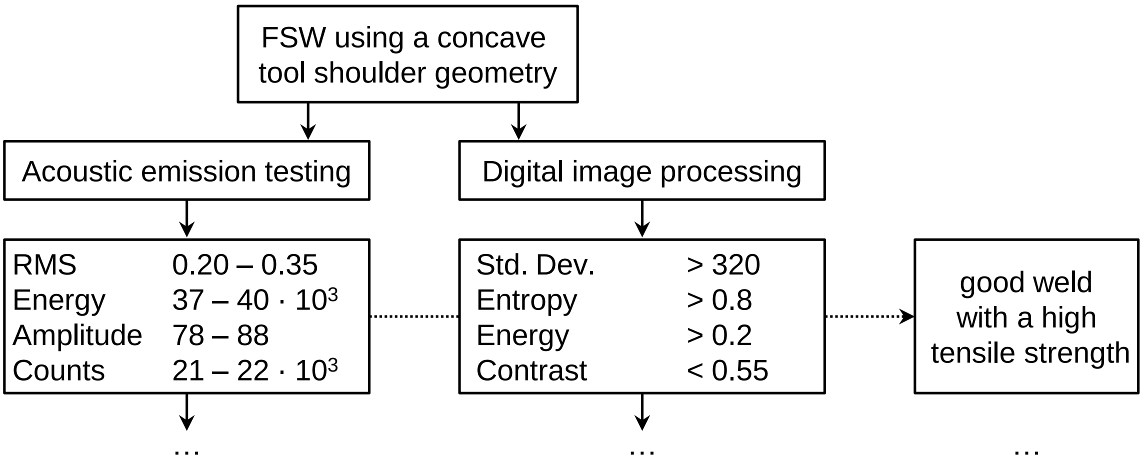

Figure 3.3: Section of the developed evaluation system for a concave shoulder geometry and the intervals for the statistical parameters that indicate a “good weld with a high tensile strength” (based on Rajashekar & Rajaprakash 2016)

Ranjan et al. (2016) were the first to use image processing not only to determine whether surface defects exist, but also to classify them. The images of the welds were taken and processed offline. Figure 3.4 illustrates both a grayscale image and also a binary black-and-white output image resulting after all image processing steps have been performed. The image processing steps are described below.

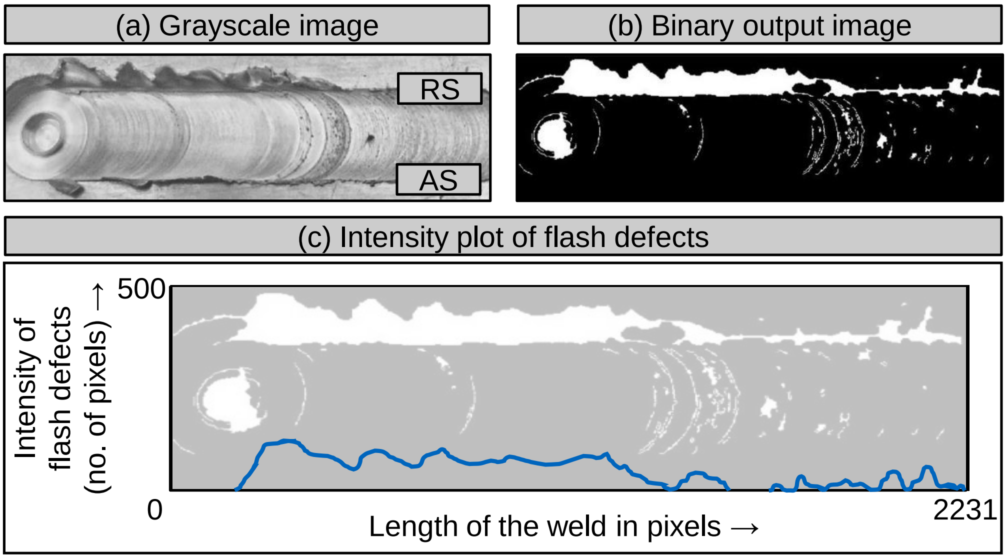

Figure 3.4: *(a) A grayscale image, (b) a binary output image containing white patches at surface defects, and (c) the corresponding intensity plot for the flash formation (based on* RANJAN ET AL. *2016)*

Initially, the images of the welds were taken with a digital camera in red-green-blue format and cut into the size of 2231 × 500 pixels (see Figure 3.4 (c)). The camera was installed at a specific location such that it always captured a fixed area of the weld. A specified illumination condition was also ensured for maintaining a uniform luminous intensity over the entire weld surface. Various image processing steps were implemented to be able to detect the different types of surface features:

- To detect grooves, voids, and the exit hole, the color images were first converted into grayscale images. For a better identification of the defects, subsequent filtering operations were conducted. The further processing was done by applying the image pyramid method (ADELSON ET AL. 1984), which was appropriate for data compression, image analysis, and image enhancement, as both spatial and frequency information of the images were retained. Afterwards, the Sobel edge detection from CANNY (1986) was applied, which resulted in a black-and-white image. Finally, some morphological operations such as dilation, erosion, morphological opening, and morphological closing were applied to obtain a white patch at the defective regions.
- To detect cracks and edges, among others, an image reconstruction algorithm (VINCENT 1993) was applied. Therefore, a so-called *mask image* and a *marker image* were necessary. The grayscale image of the original weld was used as the mask image, and an eroded image was utilized as the marker image for the image construction. For a more detailed explanation of the applied image reconstruction algorithm and the generation of the eroded image, one can refer directly to RANJAN ET AL. (2016) and VINCENT (1993).

The two resulting binary output images were merged into a single binary image that contained all types of surface defects, except for the flash formation, in the form of white patches on the black-and-white image. As the flash defects spread on the RS along the length of the weld, it was better to analyze them separately. By using the Hough transform (DUDA & HART 1972), an ROI was defined around the entire RS of the weld for analysis of flash defects, and another ROI was positioned between the RS and the AS of the weld for the identification of the other defect types (see Figure 3.4 (a)). The classification of the surface defects into the different defect types was based on the geometric characteristics of the white patches. The following definitions were made:

- **Grooves:** Grooves were long and horizontal. The major axis length of an ellipse formed around the defect patch was at least 35 pixels, and the orientation of the major axis was in the range of -25° to +25° relative to the welding direction.
- **Cracks:** Cracks were narrower than grooves. The average width was 5 pixels or less.
- **Exit hole:** The ellipse, which formed around the exit hole, had a maximal ratio of 2 between the length of the major axis and the length of the minor axis. The length of the major axis was in the range of 65 to 350 pixels.
- **Voids:** The remaining patches were classified as voids.

Afterwards, intensity plots were generated to display the amounts, the extents, and the positions of the various defects. The line in Figure 3.4 (c) shows the intensity plot for the flash formation of the weld displayed in Figure 3.4 (b), which is also in the background of Figure 3.4 (c). The line indicates how many pixels along the respective vertical line of the image are covered by flash.

The calculation time to run the developed Matlab code was mentioned to be approximately 3.9 s for one frame, whereby the computer architecture used was not specified. RANJAN ET AL. (2016) claimed that the welding speed in FSW hardly goes beyond 200 mm/min, and therefore the calculation was fast enough to use their approach for online monitoring. This statement was valid at that time; however, today welding speeds of 1000 mm/min or more are required in certain industries to produce economically, such as in the production of components for electromobility (RICHTER 2017).

Image processing using machine learning

BHAT ET AL. (2015) performed an image pre-processing step before applying a discrete wavelet transform (DWT) to images of friction stir welds to extract suitable features, which were subsequently used as inputs for a support vector machine (SVM; SCHOELKOPF & SMOLA 2002, p. 187). The SVM provided a supervised learning algorithm that classified the welds into “good” or “defective.” This was the first time that an ML method was applied to evaluate image data of friction stir welds.

The operations performed are explained in more detail as follows. The images were captured inline using a CCD camera. The resolution of the images was 280 × 840 pixels. Due to a minor change in illumination conditions at the time of the image acquisition, a pre-processing step was required. Therefore, a histogram equalization technique, which transformed the low contrast images into high contrast images, was applied (see Figure 3.1 (c), (d), and (e)). Afterwards, each pre-processed image was divided into eight sub-images along the weld seam length with a uniform length of 280 × 105 pixels. This increased the size of the training data set. The authors stated that the images could have been divided into more than eight sub-regions in the welding direction, but the images should not be too thin, as less than 50 pixels would have divided defective parts into several regions. The images of the sub-regions were then analyzed using the DWT. Contrary to the Fourier transform, the time and the frequency information of the signal can be captured using a wavelet transform, which makes it an efficient tool for the analysis of irregular and non-stationary signals (GROSSMANN & MORLET 1984). Three different statistical image parameters, namely *energy*, *variance*, and *entropy*, were calculated for every sub-image by applying the DWT.

Subsequently, the training and testing data sets were created containing images of “good” welds and “defective” welds, respectively. The data set consisted of 14 images each for “good” and “defective” welds. Further divided into eight sub-regions, 112 samples for “good” welds and 112 samples for “defective” welds were available. Of these, 70 samples each were employed for training and 42 each for testing. The SVM discriminated the data samples into the two classes using a so-called *hyperplane* that is placed with a maximum margin between the two classes. The classification was conducted using two different sets of kernels for the SVM, Gaussian and polynomial kernels (VAPNIK 2010, pp. 138 – 146). Two different SVM classifications were performed using the three features energy, variance, and entropy. For the first classification, the two features energy and variance were used, and for the second classification, the two features variance and entropy were employed. The highest test accuracy of 98.5 % was achieved when applying the Gaussian kernel with the features energy and variance.

Two other ML methods were also tested by BHAT ET AL. (2015). With Naïve Bayes (ZHANG 2004), an average classification accuracy of the test samples of 90.5 % was achieved, and with a decision tree algorithm (QUINLAN 1986) an average classification accuracy of the test samples of 88.1 % was reached. The best results were therefore obtained when using the SVM with a Gaussian kernel.

SUDHAGAR ET AL. (2019) followed a similar approach as BHAT ET AL. (2015) did and also used SVMs. A total of 27 welds were produced while varying the welding speed, the tool rotational speed, the ratio of the shoulder diameter to the sheet thickness, and the ratio of the shoulder diameter to the probe diameter. Based on a human visual inspection of the weld surfaces, 18 of the 27 welds were labeled “good” and the remaining nine welds were labeled “defective.” The image pre-processing of the color images captured with a digital camera consisted of three steps. First, the ROI were defined, whereby only the weld face was considered and the flash was no longer contained in the images of the ROI. Second, the color images were converted into grayscale images, and third, the images were resized to a uniform dimension. For feature extraction, a *maximally stable extremal region algorithm* (MATAS ET AL. 2002) was used instead of the DWT employed by BHAT ET AL. (2015). The SVM was tested with four different kernels: linear, quadratic, polynomial, and RBF. The performance of each kernel was measured by five-fold cross-validation. That is, training and testing of the SVM were performed five times with different allocations of the data into the training and the test data set each. The best classification results of 95.8 % were achieved using the linear and the quadratic kernel.

Surface topography analysis

Along with the surface appearance of friction stir welds, another surface characteristic of friction stir welds is the surface topography. So far, there have been two studies in which primarily the influence of the welding speed and the tool rotational speed on the surface topography of welds was examined.

DENG ET AL. (2014) investigated the influence of welding speed, tool rotational speed, and the tool shoulder on the surface topography of friction stir welds. The semicircular arcs covering the surface, which are typical for FSW (see Figure 2.2 (b)), showed a sawtooth shape in the longitudinal-section of the joint line. It was found that for a fixed tool rotational speed n, the distance between the individual arc lines on the surface increases as the welding speed v increases and the relation is linear. Furthermore, for a fixed welding speed v, the arc line spacing decreases as the tool rotational speed n increases. However, this interrelation is not linear. Additionally, if the n/v ratio is constant, the distance between the arc lines on the surface remains the same. Figure 3.5 illustrates these relations, described in DENG ET AL. (2014), qualitatively.

Furthermore, the influence of the tool shoulder on the surface topography was examined. For this purpose, two welds were produced. One weld was made using a tool with a shoulder, and one weld was fabricated using a tool without a shoulder only containing a tool probe. The width of the former weld was approximately 21.1 mm. On the AS the flash formation was only slight, but on the RS it was pronounced with a mean height of 3.03 mm. Without a shoulder, the weld seam width was about 13.9 mm. The classic surface arc lines disappeared and were replaced by a structure with large arc patterns that contained smaller arc patterns. On the AS, the flash formation was again low, and on the RS, the flash formation was significant with a mean height of 4.13 mm. Thus, the shoulder widened the weld, refined the arc structure, and reduced the flash formation on the RS.

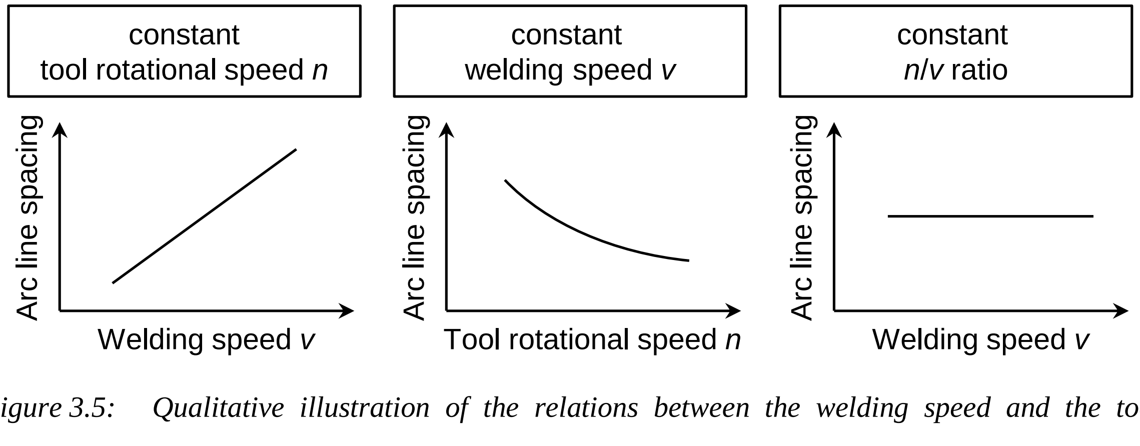

Figure 3.5: Qualitative illustration of the relations between the welding speed and the tool rotational speed with the arc line spacing (based on DENG ET AL. 2014)

ZUO ET AL. (2018) also investigated the influence of process parameters on the surface topography of friction stir welds. According to the authors, the surface topography plays an important role for the quality of the joints. Furthermore, it was stated that the main impacts regarding the profile of the arc texture can be divided into geometric factors and physical factors. The geometric factors primarily are the process parameters and the tool dimensions. The physical factors mainly include the hardness, the strength, the elastic modulus (Young's modulus), and the thermal conductivity of the material. The investigations confirmed the result from DENG ET AL. (2014) that the distance between the arc lines on the surface increases with rising welding speed v or decreasing tool rotational speed n (see Figure 3.5).

Interim conclusion

Since 2008, several investigations have already been performed in which a sequence of image processing steps were applied to extract features from images of friction stir welds and automatically classify the welds into the categories "good" and "defective." The work of RANJAN ET AL. (2016), in which an additional approach was presented to classify the types of surface defects that occurred, deserves special mention. To enable the classification of the defects, different image processing steps had to be executed depending on the surface defect. The computing time per frame was 3.9 s, whereby the computer architecture employed was not specified. BHAT ET AL. (2015) conducted the first work in which ML methods were used to classify the extracted surface features. However, the extraction of the surface features still required a high effort using image processing and a DWT. Algorithms from the field of deep learning, such as ANNs, which no longer require a manual feature extraction, have not yet been applied.

Concerning the surface topography, first systematic investigations on the influence of the process parameters on the surface topography exist. However, there are no studies that investigate how surface properties can be quantified and thus surface defects can be detected automatically by evaluating the surface topography.

3.3 Prediction of weld seam properties using supervised learning algorithms

There have been some efforts in the field of FSW to predict the weld quality by using non-destructively recorded process data. Among others, analytical models (YUNUS & ALSOUFI 2018) and empirical models, for example, ANNs (PATHAK & JAISWAL 2014), have been applied to extract the relevant information from the data sets. Empirical models in the form of ML approaches have already proven suitable for this purpose, whereby exclusively supervised learning methods have been used. In most cases, the process parameters, and in a few studies the inline measureable process variables (cf. Subsection 2.3.3), were employed as input variables. The predicted target variables were primarily mechanical properties, such as the tensile strength, or weld defects, such as cavities.

Evaluation of process parameters

OKUYUCU ET AL. (2007) used an FCNN (cf. Subsection 2.4.2) with two input neurons, seven neurons in the hidden layer, and five output neurons to predict five different mechanical properties of the friction stir welds based on the welding speed and the tool rotational speed (see Figure 3.6). Data from 20 welds were available, using 15 samples for training and five samples for testing. The inputs and the outputs were normalized to values between 0 and 1. The back-propagation algorithm with the scaled conjugate gradient optimizer (MØLLER 1993) was used. The mean relative error between the predictions and the true targets was always below 8 %. For the tensile strength, the mean relative error was 1.7 %.

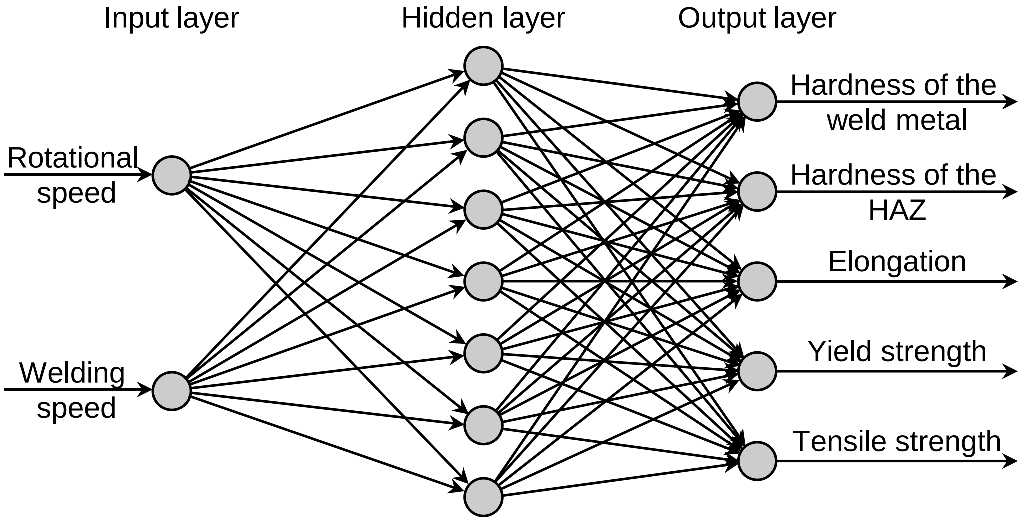

Figure 3.6: The structure of the three-layered FCNN applied in OKUYUCU ET AL. (2007)

This approach of using FCNNs to predict mechanical properties based on process parameters was similarly pursued and extended several times. For example, YOUSIF ET AL. (2008) used a FCNN with two hidden layers and achieved better results using the Levenberg-Marquardt optimizer (MARQUARDT 1963) instead of a gradient-descent-based optimizer.

VERMA ET AL. (2018) investigated the potential of ML methods other than ANNs for the prediction of the tensile strength of friction stir welded joints. The GPR (cf. Subsection 2.4.3), a SVM, and the multi-linear regression (FAHRMEIR ET AL. 2013, p. 26) were applied. Two different covariance functions were used for the GPR and the SVM: the RBF (cf. Subsection 2.4.3) and the Pearson VII universal kernel (UESTUEN ET AL. 2006). The welding speed and the tool rotational speed were employed as input variables for the models. The target variable was the tensile strength. In a full factorial experimental plan, the two factors welding speed and tool rotational speed were altered in five levels each. Of the 25 welds, 19 samples were grouped in the training data set, and the remaining six samples were grouped in the test data set. The Pearson correlation coefficient (PCC) and the root mean square error between the true and the forecasted tensile strength were used as performance indicators. The GPR, in combination with the RBF covariance function, performed best. Thereby, a PCC of 0.97 and a root mean square error of 5.94 MPa were reached for the six test samples. The multi-linear regression yielded the largest differences between the predicted and the true tensile strength. Consequently, VERMA ET AL. (2018) showed that the use of the GPR is well suited for non-destructively predicting the tensile strength in FSW.

Evaluation of process variables

Boldsaikhan et al. (2006) acquired the forces in the *x*-, *y*-, and *z*-directions (see Figure 2.6) and the spindle torque with a sampling rate of 51.2 Hz. The time series signals were converted into the frequency domain employing a 1024-point discrete Fourier transform (DFT). The areas below the DFT curve were employed as features for the FCNN inputs. Therefore, the frequency spectrum was cut into 32 equal sections, and the area below the curve was determined for each segment (see Figure 3.7). The peak at 4.16 Hz in the frequency spectrum of the *y*-force in Figure 3.7 results from the applied tool rotational speed of 250 min^{-1}, which corresponds to 4.16 Hz.

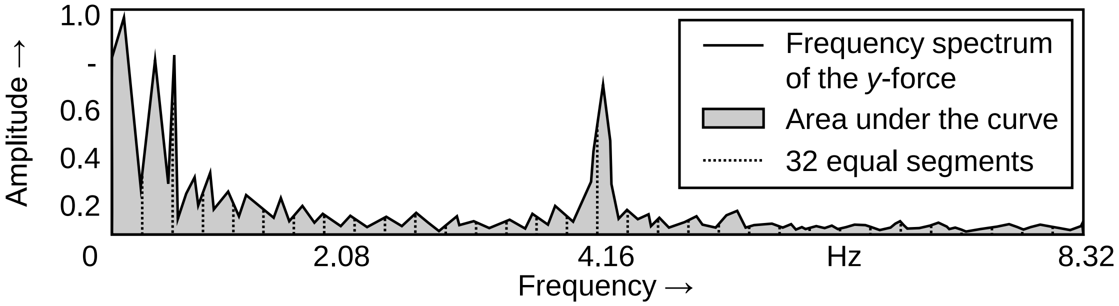

Figure 3.7: Schematic illustration of the feature extraction applied in Boldsaikhan et al. (2006)

The 32 values were utilized as feature vectors to train and test two different FCNNs:

- One FCNN forecasted whether the weld contained metallurgical failures. It was composed of 32 input neurons, 20 hidden neurons, and two output neurons (one output neuron for an occurring metallurgical defect and one output neuron for the case that there was no metallurgical defect). Cross sections of the welds were produced to determine the metallurgical defects. A total of 205 samples were available for the training and testing of the FCNN. The training data set contained 46 samples without a metallurgical imperfection and eight samples with a metallurgical imperfection. Regarding the test samples, 146 were “good” and five were “defective.” The classification accuracy for the three different forces and the spindle torque was at minimum 92.7 %. For the force in *y*-direction, the accuracy was the highest and reached 100 %.
- Another FCNN was deployed to test if it is possible to predict the tensile strength of the friction stir welds. The tensile strengths achieved were grouped into the three categories *high*, *medium*, and *low*. The architecture of this FCNN corresponded to that of the first FCNN, except that it had a total of three output neurons for the three categories instead of two output neurons. This time, a total of 198 data samples were available for training and testing of the FCNN. For the evaluation of the force in *x*-direction, the allocation of the test samples to the three classes was correct with 90.1 %. The lowest prediction accuracy of 78.1 % for the test data set was achieved for the spindle torque.

Boldsaikhan et al. (2011) evaluated feedback forces acquired during FSW experiments to identify cavities (cf. Subsection 2.3.2). During the experiments, aluminum sheets with a thickness of 6.4 mm and from the alloy EN AW-7075-T73 were butt-welded. To achieve a constant size of the cavities throughout the welds, a force-controlled mode was employed. The forces in the *x*-, *y*-, and *z*-directions were sampled at a rate of 68.2 Hz. One metallographic cross section was prepared from each weld, and the cavity diameters were measured from the metallographic samples. Depending on the cavity diameter, the welds were referred as "good" or "defective." Thereby, a threshold value of 0.08 mm was employed, which led to 14 welds labeled "good" and 16 welds labeled "defective." From each weld, eight consecutive x-force and eight consecutive y-force time intervals were extracted, with one time segment lasting 3 s and neighboring time spans overlapping by 50 %. Finally, a total of 240 data samples were available, which were divided into 180 training data samples and 60 test data samples. A DFT was employed to get the frequency spectra of the force signals. Afterwards, an FCNN was employed to classify the frequency spectra into the two categories. The initial weights were set arbitrarily in the range of -0.1 to +0.1, and the training was conducted over 500 epochs by applying a back-propagation algorithm (cf. Subsection 2.4.2). The training was always performed four times, because the random setting of the initial weights has an effect on the training of the ANNs (LEE ET AL. 2016). Afterwards, the mean of the four runs was calculated. It has been stated that, according to BOLDSAIKHAN ET AL. (2006) and LOGAR ET AL. (2007), the low-frequency bins up to 16 Hz contain sufficient information about the weld quality. Based on this knowledge, BOLDSAIKHAN ET AL. (2011) identified which portions of the frequency spectrum below 16 Hz had the greatest impact on the classification accuracy. The inputs extracted from the range of 4 Hz to 6 Hz, which corresponded to the vicinity of the spindle rotational speed of 5 Hz, had the smallest effect on the testing accuracy. Furthermore, the testing accuracy significantly increased up to a sampling rate of 12 Hz and then stayed fairly constant beyond 12 Hz. Therefore, the inputs in the range of 4 Hz to 6 Hz and the inputs beyond 12 Hz were omitted. This resulted in 60 inputs for the classification problem, which were divided into 30 inputs for the x-force and 30 inputs for the y-force. To find an adequate architecture for the FCNN, the number of neurons in the hidden layer was altered. The best architecture found consisted of 60 input neurons, nine neurons in the hidden layer, and one output neuron. It reached a mean classification accuracy of the test data set of 95 %.

DU ET AL. (2019) tested five different methods to predict the occurrence of voids in friction stir welds. In the five methods, two different ML algorithms (decision trees and FCNNs) and three different input data sets were applied:

- Process parameters, specimen geometry, tool geometry, and workpiece material properties
- Data from an analytical model
- Data from a numerical model

The construction, testing, and application of the analytical model and the numerical model were reported in six previous publications by the authors between 2006 and 2012 (NANDAN ET AL. 2006, NANDAN ET AL. 2007, ARORA ET AL. 2009, ARORA ET AL. 2011a, ARORA ET AL. 2011b, ARORA ET AL. 2012). The data extracted from the analytical model and the numerical model that were utilized as inputs for the ML algorithms were the normalized values for the local temperature, the local relative strain rate, the total torque at the probe, and the maximum shear stress. In total, 108 experimental data samples were collected from the literature (13 different references) and marked as welds with (43 samples) or without

(65 samples) void. In 12 of the 13 references, the experimental values for the axial force or the tilt angle were not reported, which then had to be estimated. The data was randomly selected for the training (63 samples), the validation (15 samples), and the testing (30 samples) of the ML models. The best results were achieved when using the data from the numerical model. A testing accuracy of 96.6 % was achieved for the FCNN and the decision tree algorithm. The neural-network-based analysis with process parameters, specimen and tool geometries, and workpiece material properties as input data predicted the void formation with an accuracy of 83.3 %.

The three studies described thus far for the evaluation of inline measurable process variables (BOLDSAIKHAN ET AL. 2006, BOLDSAIKHAN ET AL. 2011, and DU ET AL. 2019) have each dealt with the prediction of defects that were mainly the result of unsuitable process parameters. In contrast, FLEMING ET AL. (2009) determined the position of the FSW tool with respect to the center position in the T-joint configuration (see Figure 3.8). The cause of the weld defects was therefore not an inadequate choice of the process parameters but a geometrical reason.

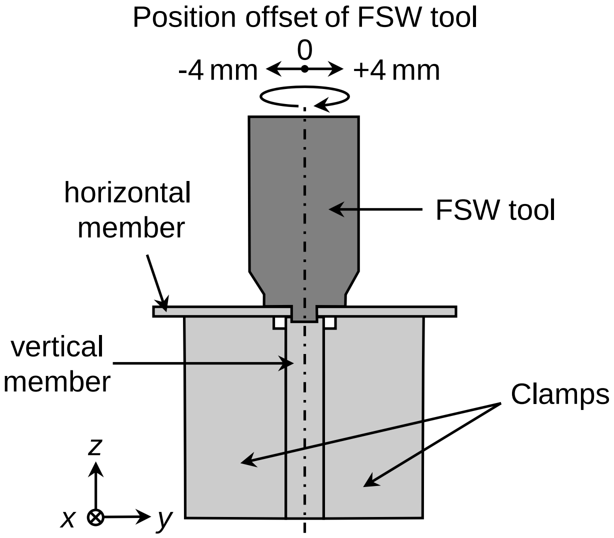

Figure 3.8: Schematic diagram of the T-joint configuration employed in FLEMING ET AL. (2009)

Welds that were produced with a larger position offset of the FSW tool tended to develop defects, which reduce the weld's strength. The forces in the *x*- and *z*-directions were employed as input data for a regression neural network (cf. Subsection 2.4.1). A total of 30 experiments were performed, each with a different offset of the FSW tool in the *y*-direction ranging from -4 mm to +4 mm from the center position. The neural network was trained and tested 30 times using leave-one-out cross-validation, that is, 29 samples were used for the training each, and the remaining sample was employed for testing. The network estimated the offset position with a mean absolute error of 0.42 mm and a standard deviation of 0.51 mm. The authors claimed that this result demonstrates the effectiveness of predicting the lateral tool position and suggested the developed system for online misalignment detection or as a position estimator for inline weld seam tracking for FSW or robotic FSW.

Interim conclusion

The presented studies on the application of supervised learning can be classified according to whether process parameters or process variables were evaluated.

The work on the evaluation of process parameters by supervised learning has been aimed primarily at determining the mechanical properties of the manufactured friction stir welds. FCNNs were mostly used for this purpose. VERMA ET AL. (2018) have already dealt with the application of GPR and have shown its effectiveness to non-destructively predict the tensile strength by data evaluation.

When evaluating process variables, the goal has been mainly the identification of weld defects, such as cavities. So far, FCNNs, which have a comparatively simple network architecture, have been used for this objective. More sophisticated types of ANNs, such as CNNs or RNNs (cf. Subsection 2.4.2), have not been employed yet. Furthermore, it is unknown if the prediction of the surface quality of friction stir welds based on process variables is possible.

3.4 Algorithm-based optimization in friction stir welding

In industrial applications, the suitable FSW process parameters are typically determined by trial and error or by manufacturers' recommendations. This selection may not result in proper welding performance and consequently causes additional energy and material consumption or results in low-quality welds (RAJAKUMAR ET AL. 2010). Various statistical and mathematical methods have already been utilized to investigate the influence of the process parameters on the mechanical properties (mostly the tensile strength), and subsequently optimize the mechanical properties by adjusting the process parameters (FARZADI ET AL. 2017). In many of the investigations, either the robust parameter design (RPD) method (MONTGOMERY 2017) or the response surface methodology (RSM; BOX & WILSON 1981) were applied. Some more recent approaches used evolutionary algorithms (YU & GEN 2010, p. 11) in combination with ANNs.

Taguchi method

The RPD method is focused on choosing levels of parameters in a process to ensure that the mean of the output response is at a desired target and to guarantee that the variability around the target value is as small as possible (MONTGOMERY 2017, p. 569). TAGUCHI (1986) proposed an approach to solve the RPD problem based on designed experiments and methods for analyzing the resulting data. A variant that has already been applied to FSW several times is the *Taguchi L9 orthogonal array,* which aims at understanding the influence of four independent factors with three levels each. With the L9 method, only nine experiments have to be performed to study four input variables at three levels. Consequently, this design reduces 81 (3^4) configurations to nine experimental evaluations (UNAL & DEAN 1991).

LAKSHMINARAYANAN & BALASUBRAMANIAN (2008) determined the optimum settings for the tool rotational speed n, the welding speed v, and the axial force F_z in FSW by adapting the Taguchi L9 orthogonal array method and maximizing the signal-to-noise (S/N) ratio. A higher S/N ratio corresponds to a better quality, and the optimal value of a process parameter is where the value of the highest S/N ratio is achieved (MONTGOMERY 2017, p. 573). To investigate non-linearities, each of the three process parameters was varied in three levels. Welding experiments were conducted for only nine out of the 27 (3^3) possible process parameter combinations. Three tensile specimens were prepared from each of the nine welds, and the mean of their tensile strength was determined. Based on the mean values for the S/N ratio and the tensile strength, an ideal process parameter setting was determined. The expected tensile strength $R_\mathrm{m}^\mathrm{exp}$ when this ideal process parameter setting was used was calculated with the formula

$$R_\mathrm{m}^\mathrm{exp} = \overline{R_\mathrm{m}^{n,\,L}} + \overline{R_\mathrm{m}^{v,\,L}} + \overline{R_\mathrm{m}^{F_z,\,L}} - 2 \cdot \overline{R_\mathrm{m}}\ , \tag{3.1}$$

whereby $\overline{R_\mathrm{m}^{n,\,L}}$, $\overline{R_\mathrm{m}^{v,\,L}}$, and $\overline{R_\mathrm{m}^{F_z,\,L}}$ are the mean tensile strengths at level L of the corresponding process parameters n, v, and F_z. $\overline{R_\mathrm{m}}$ is the overall mean of all 27 determined tensile strengths. Subsequently, the expected maximum tensile strength $R_\mathrm{m}^\mathrm{exp}$ was compared with the actual tensile strength obtained by applying the previously determined ideal process parameter setting. The deviation was 2.6 %.

The percentage contribution of the various process parameters for the resulting change of the tensile strength of the weld was also evaluated. It was observed that, within the investigated process parameter range, the rotational speed n had an influence on the tensile strength of 41 %, the welding speed v had an influence on the tensile strength of 33 %, and the axial force F_z had an influence on the tensile strength of 21 %. These percentage influences of the process parameters on the tensile strength are based upon the total variation that occurred between the highest and the lowest tensile strength. The remainder of 5 % was referred to as errors.

UGENDER ET AL. (2015) also used the Taguchi technique and the S/N ratio to find an optimum setting for the ratio of the diameter of the shoulder d_S to the diameter of the probe d_P, for the tilt angle, and for the welding speed. The results showed that the $d_\mathrm{S}/d_\mathrm{P}$ ratio and the welding speed are the most important factors, followed by the tilt angle, that determine the mechanical properties of friction stir welds of aluminum alloys. GANAPATHY ET AL. (2017) and MA ET AL. (2019), among others, have also adopted Taguchi's L9 orthogonal array design and maximized the S/N ratio by adjusting the process parameters.

Response surface methodology

RSM is an approach to solve the RPD problem that allows to employ Taguchi's robust design concept and simultaneously provides a sounder and more efficient approach to experiment design and experiment analysis (Montgomery 2017, p. 570). Furthermore, RSM is a collection of mathematical and statistical techniques for analyzing problems, in which several independent variables influence one or more dependent variables and the goal is to optimize the dependent variables (Cochran & Cox 1957, p. 335).

Rajakumar et al. (2010) applied the RSM and established an empirical relation between six independent variables (tool rotational speed, welding speed, axial force, tool shoulder diameter, tool probe diameter, and tool material hardness) and the dependent variable, which was the tensile strength of the joints. For this purpose, 52 welds were fabricated using a central composite face-centered design matrix, and a multiple regression model was developed, which was able to predict the tensile strength of the FSW joints within the 95 % confidence level. The quality of the developed model was tested applying the *analysis of variance* technique (Wahed & Tang 2010, p. 26), whereby a coefficient of determination R^2 of 0.97 indicated a good model performance. To attain the optimum tensile strength, the parameters were adjusted through five different response surfaces that revealed the optimal response points. Figure 3.9 (a) schematically illustrates a three-dimensional response surface plot exemplary for the tensile strength as a function of the welding speed and the tool rotational speed. As contour plots play an important role in the response surface analysis, the corresponding contour plots containing the contour lines, along which the response surface has a constant value, were also generated (see Figure 3.9 (b)). The maximum tensile strength estimated from the response surfaces and the contour plots was 375 MPa, when using the optimized settings for the six independent variables. Three joints were fabricated using the optimum process parameters, and the average tensile strength was 377 MPa, which was assessed as an excellent agreement with the predicted value. Similar studies were performed, among others, by Elatharasan & Kumar (2013) and Farzadi et al. (2017).

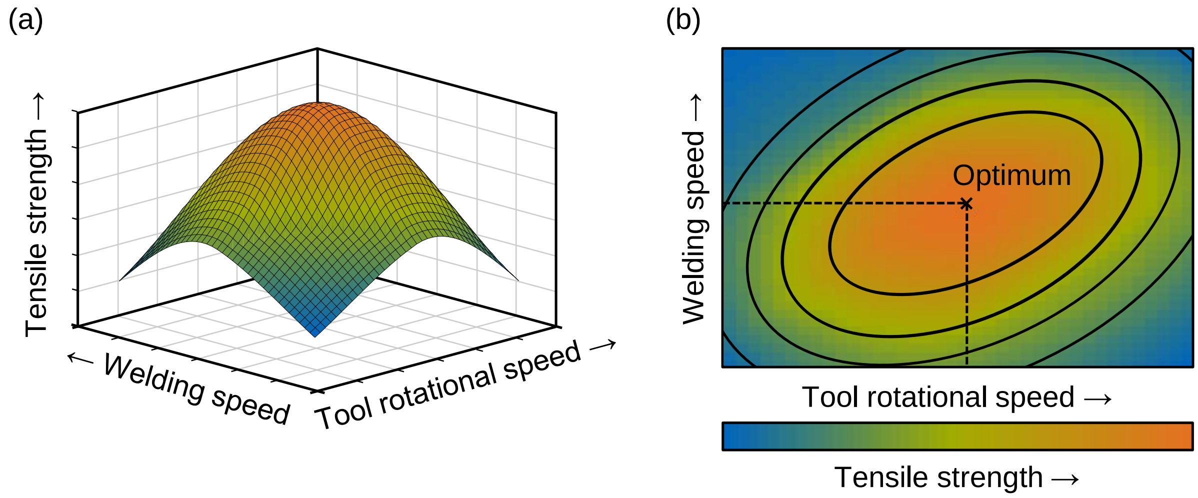

Figure 3.9: (a) Schematic response graph for the tensile strength and (b) the corresponding schematic contour graph (based on Rajakumar et al. 2010)

Additionally, the RSM was combined with other optimization methods for greater efficiency. KHANSARI ET AL. (2018) proposed a hybrid optimization methodology named GA-RSM, which is a combination of an RSM and a genetic algorithm (GA), to maximize the tensile strength by adjusting the welding speed and the tool rotational speed. GAs are iterative search procedures for the optimization of an objective function. They are based on the mechanics of natural genetics and natural selection (SIVANANDAM & DEEPA 2008, p. 15). KHANSARI ET AL. (2018) started the GA by creating a random initial population. Afterwards, the objective function was evaluated for each individual directly from the response surface, and two parents were selected to create individuals for the next population. This process was iterated until a stopping criterion was met.

Artificial neural networks coupled with evolutionary algorithms

TANSEL ET AL. (2010) applied a genetically optimized neural network system, which used five FCNNs and one GA. Figure 3.10 illustrates the genetically optimized neural network structure. The five separate neural networks with two identical inputs (welding speed and tool rotational speed) estimated mechanical properties of the welds.

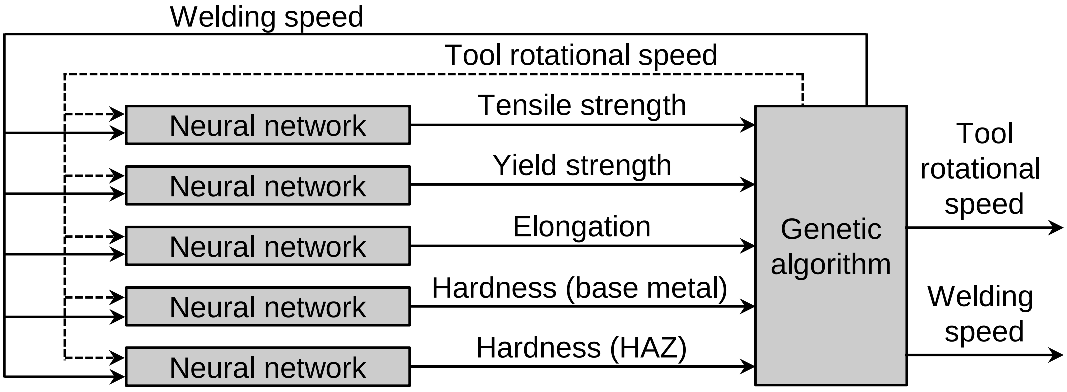

Figure 3.10: Genetically optimized neural network structure (based on TANSEL ET AL. 2010)

The FCNNs were trained with data from 20 welding experiments. Afterwards, a GA was employed to estimate the optimal welding speed and tool rotational speed. A graphical user interface (GUI) was developed to simplify the application of the algorithm. By using the GUI, search intervals could be specified by the user within which the two process parameters must be located. Through the GUI, it was also possible to define which of the five mechanical properties should be optimized and whether this feature should be minimized or maximized. For the remaining four characteristics, target intervals were defined. The genetically optimized neural network system was assessed as a viable option for modeling the FSW process and for searching for the optimal process parameters.

SHOJAEEFARD ET AL. (2013) trained an FCNN, which predicted the tensile strength and the Vickers hardness. The welding speed and the tool rotational speed were provided as inputs to the model. The FCNN included six neurons in the hidden layer. For data generation, 20 experiments were performed, using data from 16 experiments for training the FCNN and data from four experiments for testing the FCNN. The PCCs between the experimentally determined values and the predictions of the tensile strength and the Vickers hardness were 0.98 and 0.99. Subsequently, the two mechanical properties were maximized. As in many multi-objective optimizations, the objective functions were conflicting. One approach to resolve this conflict consists of a set of solutions that is Pareto optimal (MATHUR 1991). A Pareto optimal solution cannot be improved with respect to an objective unless at least one other objective is made worse. To optimize the tensile strength as well as the Vickers hardness, a hybrid multi-objective evolutionary algorithm consisting of two stages was proposed. The first stage contained the generation of a Pareto set by *multi-objective particle swarm optimization* (COELLO & LECHUGA 2002). In the second stage the *technique for order preference by similarity to ideal solution* (TOPSIS; LAI ET AL. 1994) was applied to rank the given alternatives obtained by the multi-objective particle swarm optimization and to find the best compromise solution from the Pareto set for optimizing the tensile strength and the Vickers hardness.

SHOJAEEFARD ET AL. (2014) extended the approach of SHOJAEEFARD ET AL. (2013). A finite element method (FEM) model was created that was used to calculated the peak temperature, the axial force, and the width of the HAZ dependent on of the welding speed and the tool rotational speed. An experimental validation of the simulation by evaluating the axial force and the temperatures demonstrated a high model performance. For data generation, 24 FEM simulations were performed, which required a total computing time of 450 hours. The computer architecture used for the simulation was not described. Subsequently, a meta-model based on an ANN was trained with the simulation data. The aim of the meta-model was to time-efficiently achieve the required results. An FCNN with two input neurons, eight neurons in the hidden layer, and three output neurons was used. The PCCs between the results of the FEM simulation and the FCNN were 0.97, 0.99, and 0.96 for the peak temperature, the axial force, and the width of the HAZ, which is why the FCNN's predictions were considered very accurate. To find optimum values for the welding speed and the tool rotational speed, as suggested by SHOJAEEFARD ET AL. (2013), a hybrid multi-objective evolutionary algorithm was applied. The peak temperature was maximized and the width of the HAZ and the axial force were minimized, while the two process parameters remained within defined boundaries. The first stage contained the generation of a Pareto set by a *non-dominated sorting genetic algorithm* (DEB ET AL. 2002). The second stage used the TOPSIS algorithm to obtain the best compromise solution from the Pareto set. Four FSW samples were then produced: two with optimal process parameters determined with the TOPSIS algorithm and two with non-optimal process parameters. One tensile test was performed for each of the four welds and the tensile strength of the welds was higher in case they were fabricated with the optimized process parameters.

ALKAYEM ET AL. (2016) compared four different evolutionary algorithms with respect to their suitability for optimizing the mechanical properties in FSW. For this purpose, they conducted 59 welding experiments, whereby eight different input parameters (plunge depth, tool rotational speed, welding speed, tool geometry, shoulder diameter, probe diameter, tool probe length, and dwell time) were varied and five different output parameters (tensile strength, yield strength, ductility, bending angle, and nugget zone hardness) were determined. The data from 40 experiments were used for training an FCNN and the data from 19 experiments were employed for testing the FCNN. The mean absolute percentage errors for predicting the mechanical properties from the welds contained in the test data set were all below 10 %, whereby for the tensile strength the error was the lowest with 1.9 %. The FCNN was thus able to predict the mechanical properties well. For the subsequent optimization of the input parameters, four evolutionary algorithms were tested: binary-coded GA (DEB 2001, p. 80), real-coded GA (DEB 2001, p. 106), differential evolution (STORN & PRICE 1997), and particle swarm optimization (KENNEDY & EBERHART 1995). The particle swarm optimization was the most suitable, because it led to accurate results and the optimal solution was found with a lower number of iterations compared to the other three evolutionary algorithms.

Interim conclusion

Initially, approaches to optimize process parameters in FSW were limited to the use of experimental design plans. The aim was to obtain as much information as possible about the influence of the independent variables on the dependent variables with as few experiments as possible.

Since 2010, ANNs have been increasingly applied in combination with evolutionary algorithms (primarily GAs). Thereby, the relation between the process parameters and the weld quality was modelled using ANNs, and evolutionary algorithms determined the process parameters for an optimized welding result. These investigations aimed at maximizing the mechanical properties (mostly the tensile strength) of the friction stir welds. Studies regarding the maximization of the surface quality have not been performed yet. Furthermore, with BO and RL (cf. Subsection 2.4.4 and 2.4.5), there are two promising optimization approaches from the field of ML that can handle the exploration-exploitation dilemma well and that have not yet been applied to FSW.

3.5 Correlations between surface properties and mechanical properties

Regarding the correlations between the surface properties and the mechanical properties of friction stir welds, qualitative statements can be found in state-of-the-art studies. The following are two examples:

- RAJASHEKAR & RAJAPRAKASH (2016): “The surface texture of friction stir welds is related to the internal structure of the weld.”
- SUDHAGAR ET AL. (2019): “The correlation between tensile strength and surface appearance reveals that weld joint[s] with irregular and defective surface[s] possess lower tensile strength.”

To the knowledge of the author, only one work exists, in which the correlations between the surface properties and the tensile strength have been quantified: DAS ET AL. 2016 tested both the fractal theory (MANDELBROT 1982) and the wavelet transform (GROSSMANN & MORLET 1984) to extract information from images of friction stir weld surfaces and correlated this information with the weld’s tensile strength.

Ten welding experiments were performed for this purpose, while the welding speed and the tool rotational speed were varied in three levels. One experiment was repeated to explore the process variability. Three tensile samples were cut out from each weld and their mean tensile strength was determined. A digital camera was used to capture a color image of each weld surface. The typical semicircular arcs on the weld surfaces (see Figure 2.2 (b)) varied for the different process parameters. This was taken as the central motivation to correlate the information gained from the semicircular arcs with the tensile strength.

Fractal theory provides methods for detecting irregular geometries. Figure 3.11 illustrates three well-known examples of fractals: an *Apollonian gasket* (BOURKE 2006), a *Mandelbrot set* (MANDELBROT 1982, p. 189), and a *Sierpiński triangle* (CONVERSANO & TEDESCHINI-LALLI 2011).

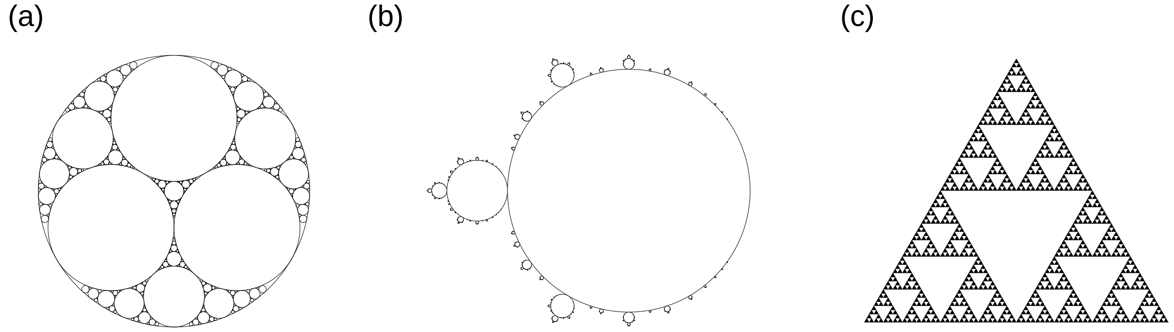

Figure 3.11: Three examples of fractals: (a) Apollonian gasket (based on BOURKE 2006 and JACQUENOT 2020), (b) Mandelbrot set (based on MANDELBROT 1982, p. 189, and MAJEWSKI 2010), and (c) Sierpiński triangle (based on CONVERSANO & TEDESCHINI-LALLI 2011 and MARTÍNEZ-CAGIGAL 2020)

The fractal dimension (FD) characterizes features of images obtained from nature (NAYAK & MISHRA 2016) and reflects the self-similar properties of objects (MUGUTHU & GAO 2013). The FD can be applied for distinguishing surfaces that provide a geometric configuration at different scale lengths (LING 1990). Various algorithms are available for calculating the FD of different objects. The calculation of the FD from images requires fewer calculation steps and therefore provides the information faster than other image processing techniques do, which involve more sub-steps and make the monitoring process more time-consuming (VALAVANIS & KOSMOPOULOS 2010).

In DAS ET AL. (2016), two methods were applied to determine the FDs: a *box counting algorithm* (RUSSELL ET AL. 1980) and *Katz's method* (KATZ 1988). For the application of Katz's method, the color images of the welds were converted into grayscale images, while for the box counting algorithm, binary black-and-white images were necessary. By using the box counting algorithm, a PCC between the FD and the tensile strength of -0.79 was reached. The larger the FD was, the lower the tensile strength tended to be. When employing Katz's method, the PCC between the FD and the tensile strength was -0.91. Consequently, Katz's method was rated as more suitable to extract intricate details of the weld surface images.

Apart from fractal theory, a two-dimensional wavelet transform was also applied to retrieve information from the images. The original weld images were first converted into binary images, to which the wavelet transform was then applied. A new indicator called CI was introduced based on the data generated by the wavelet transform. The PCC between CI and the tensile strength was -0.93. The higher the indicator CI was, the lower was the tensile strength.

Interim conclusion

DAS ET AL. (2016) demonstrated for the first time that it is possible to quantify the correlation between the surface properties of friction stir welds and their tensile strength. For this purpose, either fractal theory or the wavelet transform was used to extract suitable information from the weld images. Both techniques still require manual effort to obtain the surface features. Whether there are quantifiable correlations between the topography of friction stir welds and their mechanical properties has not yet been investigated.

3.6 Need for action

The critical review of thematically related research studies has revealed the current state of research prior to this thesis work, especially with regard to the automated detection of surface properties as well as the application of supervised learning methods and optimization algorithms in the field of FSW. On this basis, five crucial research areas (RAs) were derived for the present thesis:

RA1 FSW is increasingly applied in the production of battery trays for electromobility. Particularly in this industry, demand is rising for an automated surface inspection of friction stir welds, which also operates reliably at welding speeds of more than 1000 mm/min (cf. Section 1.2). In the studies conducted thus far, a large number of image processing steps such as filtering or histogram equalization were necessary to determine the surface features from the camera images. These methods are very sensitive, for example, with respect to camera position or illumination conditions. Furthermore, these methods require long computing times, which makes them unsuitable for weld surface monitoring in industrial applications, especially at higher welding speeds. Former investigations using ML methods for the classification of surface properties still require manual extraction of the surface features from the images. In addition, until now, only a binary classification of the welding surface into the categories “good” and “defective” has been conducted by applying ML methods. Consequently, the recognition of the various surface characteristics by utilizing an automated visual inspection system remains an issue for which suitable solutions must be found. To date, there are no investigations regarding the use of deep learning for the automated detection of surface defects of friction stir welds on the basis of image information (cf. Section 3.2). As described in Subsection 2.4.1, deep learning often requires less human data preprocessing and delivers more accurate results compared to traditional ML approaches.

RA2 There are studies that prove that the process parameters influence the weld topography (cf. Section 3.2). However, it has not yet been investigated how the surface properties of friction stir welds can be quantified and how surface defects can be detected automatically on the basis of the topography. This knowledge is a necessary pre-requisite for the realization of a monitoring system based on the surface topography.

RA3 Indirect monitoring systems are less sensitive to environmental influences, such as illumination conditions and pollution, in the production area than direct monitoring methods are (cf. Subsection 2.3.3). There are no examinations regarding the application of more sophisticated types of ANNs, such as CNNs and RNNs, for indirect monitoring in FSW. So far, FCNNs have exclusively been used to evaluate process variables such as forces or the spindle torque in FSW (cf. Section 3.3). CNNs and RNNs have proven to be quite powerful, especially for the analysis of images and time series (cf. Subsection 2.4.2). It must be explored whether these network architectures yield better results for indirect monitoring in FSW than FCNNs. Furthermore, there have been no studies yet to examine the prediction of the surface quality of friction stir welds on the basis of process variables.

RA4 Previous research primarily has aimed at optimizing mechanical properties by adjusting process parameters (cf. Section 3.4). The optimization of the surface quality has not yet been investigated. However, the surface of friction stir welds is important, because it is usually the first quality criterion evaluated when qualifying the FSW process for a new welding task. Only when the quality of the surface is satisfactory, further examinations such as tensile tests and metallography are usually conducted. The proper adjustment of the process parameters to improve the surface quality is typically determined by trial and error and on the basis of the experience of the manufacturer. This iterative process usually requires numerous preliminary tests and generates rejected parts (scrap). There are (apart from previously published own work) no studies in the field of FSW that explore the application of BO and RL that are capable of dealing with the exploration-exploitation dilemma well. This capability is necessary to replicate the decisions of experienced machine operators and thus to support less experienced FSW users in the search for suitable process parameters and the optimization of the weld quality. The algorithms can help to produce fewer rejected parts and save time during the qualification of FSW for new welding tasks. Particularly, enterprises with little experience in FSW or with frequently changing welding tasks, such as contract welders, would benefit from this. Manufacturers of FSW systems could integrate the algorithm into their already existing computer-aided manufacturing (CAM) software. Consequently, research is required to determine whether the surface quality of friction stir welds can be efficiently optimized using BO and RL.

RA5 To date, there are primarily qualitative or quite general statements regarding the relations between the surface properties and the mechanical properties of friction stir welds (cf. Section 3.5). The correlations have only been quantified in one study so far. Either fractal theory or the wavelet transform have been employed to process images of weld surfaces. These methods still require a manual effort to extract the features from the images. The evaluation of the surface topography to identify the surface characteristics demands fewer manual activities, as the data is available in the form of a three-dimensional point cloud, the analysis of which can be automated easily. However, the correlations between the surface topography and the mechanical properties have not been investigated yet. Together with the surface quality, the mechanical properties are important quality criteria for friction stir welds. The correlations between the surface topography and the mechanical properties must be analyzed to identify whether monitoring the topography can also yield information about the mechanical properties. Knowledge of these correlations is mandatory to estimate the potential of a non-destructive monitoring system based on the surface topography. Such a system could be of particular benefit to manufacturers in high-tech sectors with safety-critical applications such as aviation and aerospace.

The following chapter will outline the research approach dedicated to address this need for action in the mentioned five RAs.

4 Research Approach

4.1 Chapter overview

This chapter outlines the research approach of the thesis. Based on the review of the related literature (see Chapter 3), the scientific objective is derived and discussed in Section 4.2. The methodological approach to achieve the scientific objectives is explained in Section 4.3. Section 4.4 gives an overview of the embedded publications. Section 4.5 provides an overview of the experimental approach and the most important hardware and software components that were used.

4.2 Scientific objective

To date, when qualifying FSW for a new welding task, the process parameters usually have to be determined iteratively by trial and error. The efficiency of this procedure strongly depends on the experience of the manufacturer, that is, the machine user. In the first step, the quality of the weld surface is evaluated. Only when the weld's surface is defect-free and assessed satisfactory, further steps such as tensile tests and metallography follow to examine the mechanical properties and the internal weld structure. Due to this iterative procedure consisting of surface inspection and adjustment of the process parameters, finding suitable process parameters is often associated with a major experimental effort. Hence, the main objective of this work is to find an approach for automated monitoring and optimization of the surface quality of friction stir welds. The following three sub-targets (STs) are derived from this:

ST1 Surface properties are to be identified automatically and reliably. This should be realized directly on the basis of surface properties such as appearance (cf. RA1) and topography (cf. RA2). The direct detection of the surface with cameras or sensors based on laser triangulation is influenced by environmental conditions such as illumination and dust formation and by the position of the sensor relative to the weld seam on the workpiece. Therefore, alternatively, an indirect and more robust method also has to be developed, which allows drawing conclusions about surface properties by evaluating process variables such as the process forces (cf. RA3).

ST2 The surface quality is to be optimized efficiently by an algorithm-based adjustment of the process parameters. As such, the two most important process parameters, the welding speed and the tool rotational speed, are to be adjusted. The aim is to develop an algorithm that can reflect the knowledge of an experienced human operator who usually adjusts the process parameters efficiently. (cf. RA4)

ST3 The correlations between the surface topography and the mechanical properties of friction stir welds are to be determined. If significant correlations exist, an algorithm should evaluate the surface data of the friction stir welds and determine the mechanical properties. The uncertainty of the prediction has to be assessed, as it is important for safety-critical applications. (cf. RA 5)

4.3 Methodological approach

Since the use of AI and especially of ML methods has proven to be quite suitable for extracting patterns from data and modeling implicit knowledge (cf. Section 1.1), various ML methods were applied for this dissertation to achieve the defined STs (cf. Section 4.2). Furthermore, the quality of the weld surface produced during FSW was employed as the quality attribute for two reasons: First, the weld surface is an important criterion for the quality of friction stir welds. Second, compared to the evaluation of mechanical properties and microstructures, it is easier to obtain a sufficient amount of data for training the algorithms by evaluating the weld surface. The approach pursued for this thesis consists of three stages, whose results are documented in a total of six publications, referred to as P1 to P6 (see Figure 4.1):

Stage 1 In this stage, ST1 was addressed. An automated visual inspection of the weld surface was first implemented by means of deep learning (P1). For this purpose, CNNs were used, as these have proven to be particularly suitable for the recognition of patterns in images (cf. Subsection 2.4.2). By using a CNN-based object detection algorithm, the welds were first recognized before the surface properties of the welds were classified by another CNN. In P2, an approach was developed to efficiently process the point cloud generated by scanning the weld topography. Scalar topography indicators were defined, which can be calculated from the point cloud and which allow a quantification and detection of surface defects based on the topography. After the possibilities of direct detection of the surface properties were investigated in detail, the indirect monitoring of the surface quality was examined in the next step. For this purpose, different types of ANNs were tested and various process variables were evaluated (P3).

Stage 2 The goal in this stage was to reach ST2. Two algorithms were applied, which allow for the optimization of the surface quality by adjusting the process parameters. With RL and BO, two ML-based algorithms that are able to deal with the exploration-exploitation dilemma were utilized for this purpose. To quantify the surface quality, scalar topography indicators based on publication P2 were used. The results of Stage 2 were published in P4.

Stage 3 This stage aimed at achieving ST3. It began with the evaluation of correlations between the surface topography and the mechanical properties of friction stir welds (P5). Subsequently, the identified correlations were utilized to predict the tensile strength on the basis of the surface topography using GPR (P6).

The GPR was applied according to P6 for three reasons:

- Since the GPR is a non-parametric method, it provides high flexibility in modeling (cf. Subsection 2.4.3).
- The probabilistic approach allows a quantification of the prediction’s uncertainties (cf. Subsection 2.4.3).
- VERMA ET AL. (2018) compared the performance of the GPR to predict the tensile strength based on the process parameters with two other ML algorithms, and the GPR led to the best results. (cf. Section 3.3)

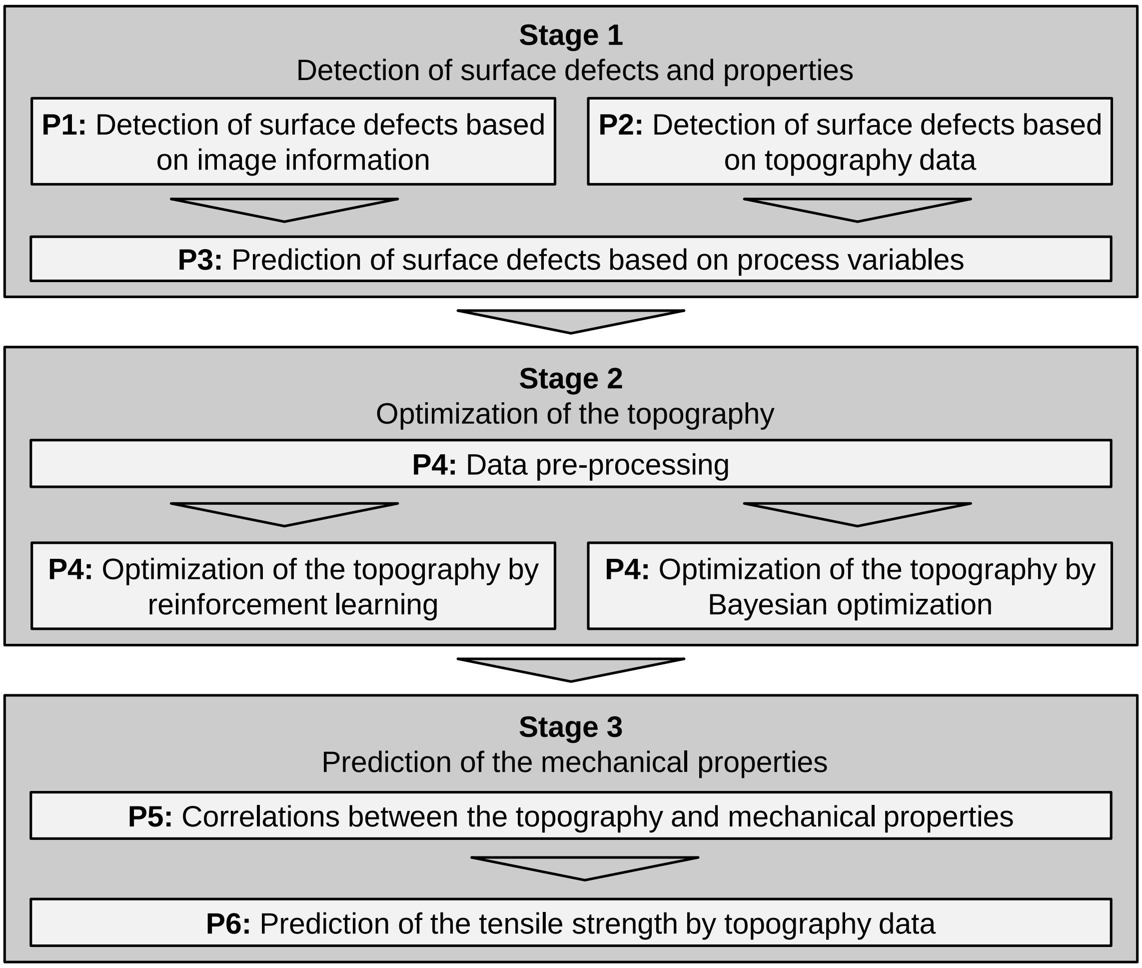

Figure 4.1: Holistic methodology, consisting of sequentially arranged stages to achieve the STs described in Section 4.2

In the publications P1, P3, P4, and P6, ML methods were used. The focus of the publications P2 and P5 was primarily on the analysis and understanding of the data. The application of the ML methods to extract useful knowledge from the recorded data was oriented toward the KDD process (cf. Subsection 2.4.1).

4.4 Embedded publications

Figure 4.2 contains an overview of the six publications P1 to P6 with the authors, the titles of the publications, and the publication media. A list of the publications embedded in this dissertation can be found in Appendix A.1.

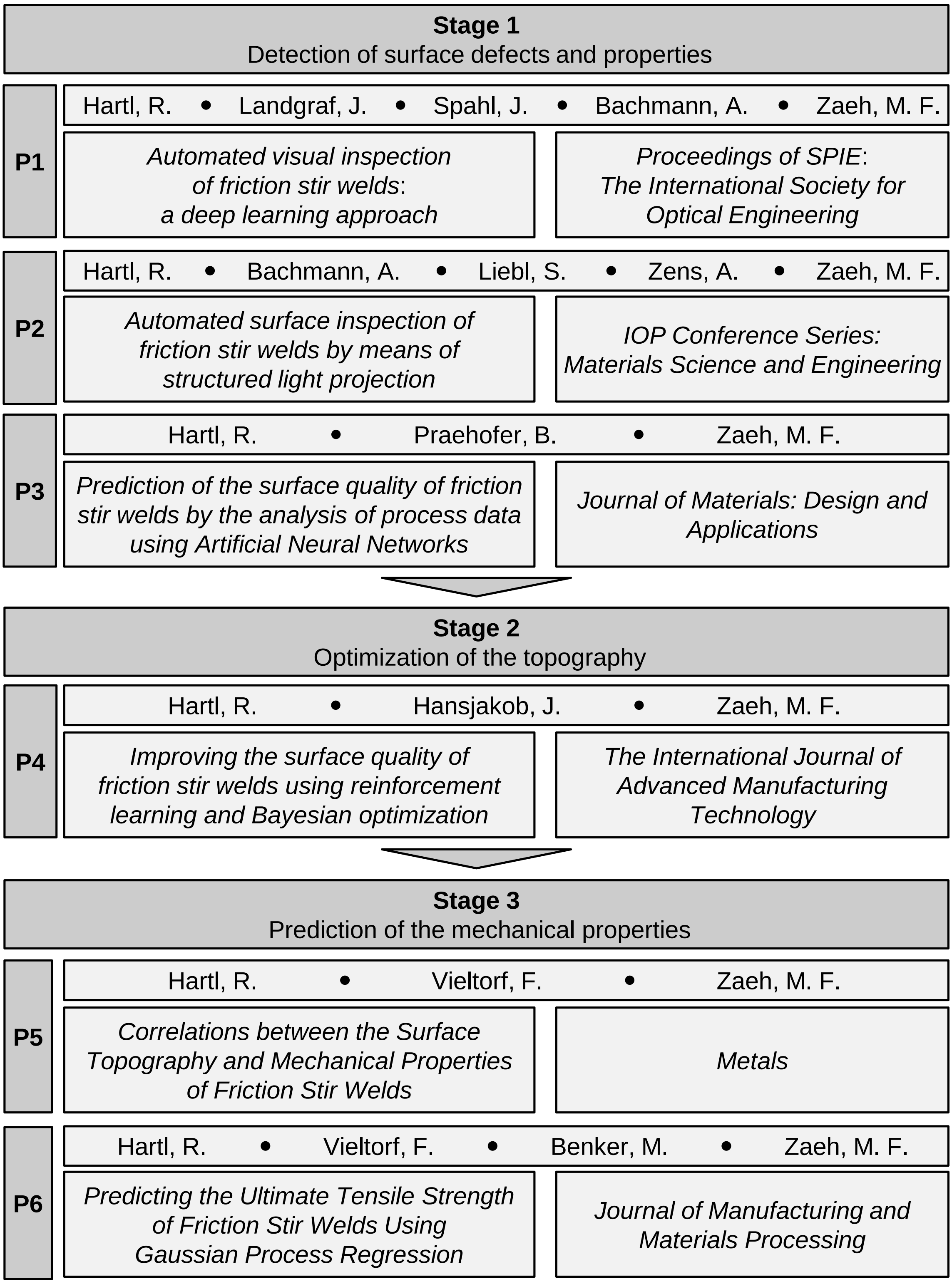

Stage 1
Detection of surface defects and properties

P1
Hartl, R. • Landgraf, J. • Spahl, J. • Bachmann, A. • Zaeh, M. F.
Automated visual inspection of friction stir welds: *a deep learning approach*
Proceedings of SPIE: *The International Society for Optical Engineering*

P2
Hartl, R. • Bachmann, A. • Liebl, S. • Zens, A. • Zaeh, M. F.
Automated surface inspection of friction stir welds by means of structured light projection
IOP Conference Series: Materials Science and Engineering

P3
Hartl, R. • Praehofer, B. • Zaeh, M. F.
Prediction of the surface quality of friction stir welds by the analysis of process data using Artificial Neural Networks
Journal of Materials: Design and Applications

Stage 2
Optimization of the topography

P4
Hartl, R. • Hansjakob, J. • Zaeh, M. F.
Improving the surface quality of friction stir welds using reinforcement learning and Bayesian optimization
The International Journal of Advanced Manufacturing Technology

Stage 3
Prediction of the mechanical properties

P5
Hartl, R. • Vieltorf, F. • Zaeh, M. F.
Correlations between the Surface Topography and Mechanical Properties of Friction Stir Welds
Metals

P6
Hartl, R. • Vieltorf, F. • Benker, M. • Zaeh, M. F.
Predicting the Ultimate Tensile Strength of Friction Stir Welds Using Gaussian Process Regression
Journal of Manufacturing and Materials Processing

Figure 4.2: Publications contributing to the three stages of the methodology outlined in Section 4.3

In all six publications, the author of this dissertation is also the main author. Andreas Bachmann, Maximilian Benker, Stefan Liebl, and Amanda Zens are or were research associates at the Institute for Machine Tools and Industrial Management (*iwb*) at the Technical University of Munich (TUM). They contributed to brainstorming as well as the validation and auditing of the research results. Furthermore, Stefan Liebl was head of the department for joining and cutting technologies, and Andreas Bachmann was head of the department for additive manufacturing. Julius Hansjakob, Johannes Landgraf, Benedikt Praehofer, Julian Spahl, and Fabian Vieltorf were students who supported the experimental work and programming activities. A list of the supervised student research projects is given in Appendix A.2. Prof. Dr.-Ing. Michael F. Zaeh is head of the *iwb* and supervisor of this work. A more detailed overview of the authors' individual contributions to the publications is provided in Chapter 5.

4.5 Experimental procedure

The description of the experimental procedure in the following paragraphs is based on the process characterization provided in Figure 2.5. Only the most important experimental conditions are explained. More detailed information is provided in the individual publications.

Workpiece: Either the aluminum alloy EN AW-5754-H111 or the aluminum alloy EN AW-6082-T6 were employed for the experiments (cf. Section 2.2). Aluminum alloys from the 5000 and 6000 series are frequently used for lightweight applications in industry, for example, in electromobility (RICHTER 2017). The chemical composition of the used materials was reported by the selected material supplier Bikar-Metalle GmbH (Bad Berleburg, Germany), as listed in Table 4.1. The sheet thickness t_S was either 2 mm, 3 mm, or 4 mm.

Table 4.1: Chemical compositions of the used materials EN AW-5754-H111 and EN AW-6082-T6 in % by mass (BIKAR-METALLE GMBH 2017). The rest in both alloys is aluminum.

Aluminum alloy	Si	Fe	Cu	Mn	Mg	Cr	Zn	Ti	Others
EN AW-5754-H111	0.30	0.34	0.06	0.30	3.20	0.04	0.06	0.04	max. 0.04
EN AW-6082-T6	0.90	0.42	0.10	0.44	0.70	0.03	0.13	0.03	max. 0.05

Welding machine: The welding experiments were conducted on a four-axis horizontal milling machine MCH 250 from Gebr. Heller Maschinenfabrik GmbH (Nuertingen, Germany), which had been adapted to perform FSW. The maximum axial force of the system was 30 kN. Only one-dimensional welds in butt-joint configuration were produced. In combination with the clamping system and the measuring equipment, the maximum possible weld seam length for a single weld was 205 mm on the employed welding machine.

Process parameters: Information on the performed experimental studies is listed in Table 4.2. Within 11 studies, a total of 316 welds with lengths between 100 mm and 205 mm were produced. The cumulative length of all welds was approximately 47 m. All experiments were conducted in position-controlled mode to prevent damage to the machine components, the welding tool, or the sensible measuring equipment. The tilt angle was 2° in all experiments. Within the studies, the two factors welding speed v and tool rotational speed n were varied. As high welding speeds are becoming increasingly important for industrial applications, especially for electromobility (RICHTER 2017), welding speeds of up to 1500 mm/min were employed. In Studies 1 to 8, the process parameters were adjusted with four levels each for the two factors with welding speeds from 500 mm/min to 1500 mm/min and tool rotational speeds from 1500 min^{-1} to 3500 min^{-1}. Study 9 was performed with only one welding speed and 13 different tool rotational speeds. In Study 10, the two factors were altered in 11 levels according to a full factorial experimental plan. In Study 11, three different welding speeds were investigated, whereby the number of different tool rotational speeds when applying the three welding speeds was 16, 18, and 20.

Table 4.2: Overview of the 11 experimental studies (based on HARTL ET AL. 2019b)

Study no.	Experiment no.	No. of exp.	Levels for ...v	...n	Aluminum alloy	Shoulder geometry	Sheet thickness	Used for publication
1	1 – 16	16	4	4	EN AW-5754-H111	concave	4 mm	P1, P2, P4
2	17 – 32	16	4	4	EN AW-5754-H111	spirals	4 mm	P1, P2, P4
3	33 – 48	16	4	4	EN AW-6082-T6	concave	4 mm	P1, P4
4	49 – 64	16	4	4	EN AW-5754-H111	rings	4 mm	P1, P4
5	65 – 80	16	4	4	EN AW-6082-T6	rings	4 mm	P1, P3, P4
6	81 – 96	16	4	4	EN AW-6082-T6	rings	4 mm	P1, P3, P4
7	97 – 112	16	4	4	EN AW-5754-H111	concave	2 mm	P1, P4
8	113 – 128	16	4	4	EN AW-5754-H111	rings	4 mm	P3, P4
9	129 – 141	13	1	13	EN AW-6082-T6	concave	4 mm	P4
10	142 – 262	121	11	11	EN AW-6082-T6	rings	3 mm	P4
11	263 – 316	54	3	16 – 20	EN AW-6082-T6	concave	4 mm	P5, P6

Welding tools: Two-piece tools consisting of a probe and a shoulder (see Figure 2.1) were used. This had the advantage that the probe length l_P, which primarily determines the weld penetration depth, could be adjusted to guarantee a complete penetration welding. The probes always had three lateral flats and a right-hand thread. As the tool spindle rotated counter-clockwise, the material was transported into the direction of the backing plate, which resulted in an additional compression of the material. The most important dimensions of the tools were the radii of the probe r_P and of the shoulder r_S as well as the probe length l_P (see Figure 4.3).

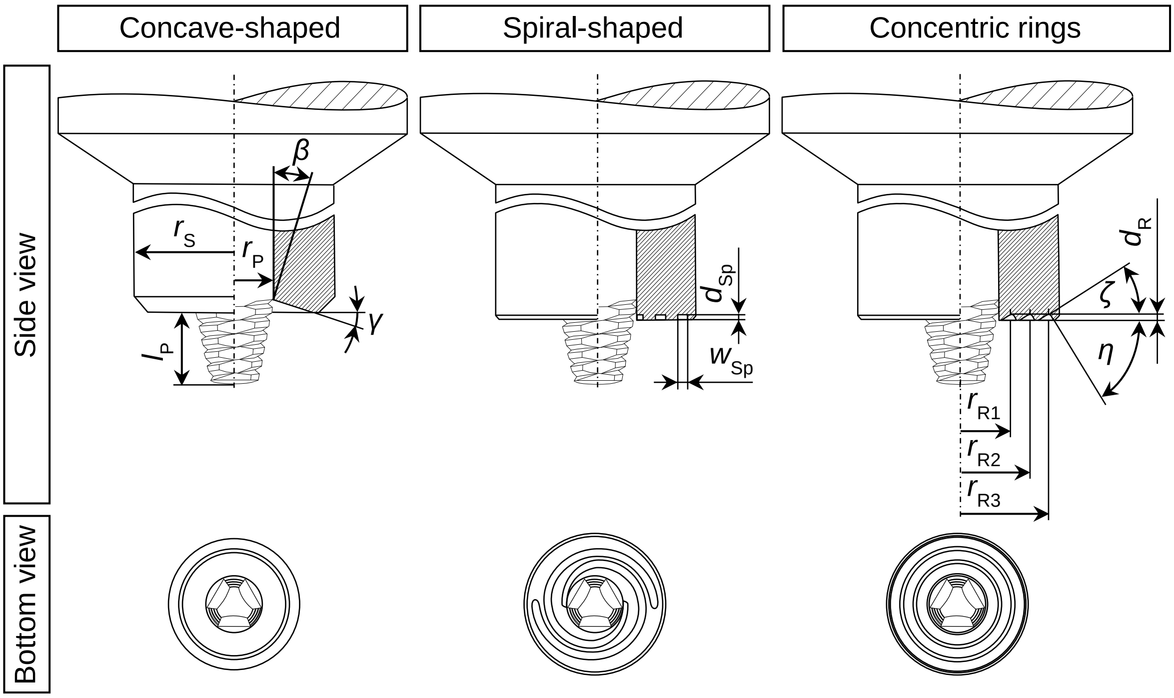

Figure 4.3: Schematic illustration of the employed tool geometries (based on HARTL ET AL. 2019b)

The probes were conical with an angle *ß* to reduce the process forces during the plunge phase and the main phase. To produce different surface characteristics, three different geometries were employed on the front side of the shoulders:

- Concave-shaped geometry: The concave tool was characterized by the angle γ.
- Spiral-shaped geometry: The two spirals were specified by the depth d_{Sp} and the width w_{Sp}.
- Concentric rings: The three concentric rings had the radii r_{R1}, r_{R2}, and r_{R3} and were further described by the depth d_{R} of the rings and the two angles ζ and η.

The geometric dimensions of the tools applied are specified in the respective publications.

Recording of the process variables: For the publications P3 and P6, the accelerations a_x, a_y, and a_z, the forces F_x, F_y, and F_z, the spindle torque M_z (see Figure 2.6), and the temperatures at the tool probe T_{P} and the shoulder T_{S} were recorded. Figure 4.4 schematically illustrates the experimental setup containing the real-time system for acquiring the process variables. The central unit of the real-time system was a MicroLabBox from dSPACE GmbH (Paderborn, Germany), which was equipped with several analog as well as digital input and output interfaces.

Accelerometers made by Kistler Instrumente GmbH (Winterthur, Switzerland) were used to quantify the vibrations with up to 20 kHz. Following the recommendation of PANZER ET AL. (2018), the accelerometer was positioned as close as possible to the process nearby the plunge point of the tool.

As the direct method to measure the process forces and the spindle torque provides a higher measuring accuracy compared with the indirect method via the motor currents of the tool spindle and the moving machine axes (SMITH 2007, p. 232), the former method was chosen. Therefore, a dynamometer that had been developed and implemented together with Hottinger Brüel & Kjaer GmbH (Darmstadt, Germany) was utilized to record the forces F_x, F_y, and F_z, and the spindle torque M_z with a sampling rate of 9.6 kHz. The dynamometer consisted of two parts: The *x*- and the *y*-component of the process force were determined through four force measuring sensors, which were mounted behind the backing plate. The *z*-component of the process force and the spindle torque were recorded by another sensor unit. The signal transmission from the rotating sensor (rotor) to the fixed receiver (stator) as well as the power supply were conducted wirelessly by induction. The utilized dynamometer is described in detail in KRUTZLINGER ET AL. (2015).

As the integration of thermocouples into the tool probe or the tool shoulder has proven to be suitable for research purposes (NISHIHARA & NAGASAKA 2004), this approach was applied. The temperatures T_P and T_S were gauged with the aid of a special measuring tool adapted from COSTANZI ET AL. (2017). The temperature signal processing unit was attached to the SK 50 tool holder. The unit digitalized the analog measurement signal of the thermocouples and sent it via wireless local area network (WLAN) to a receiver module that was connected to the real-time system. The sampling rate of the temperature was 221 Hz.

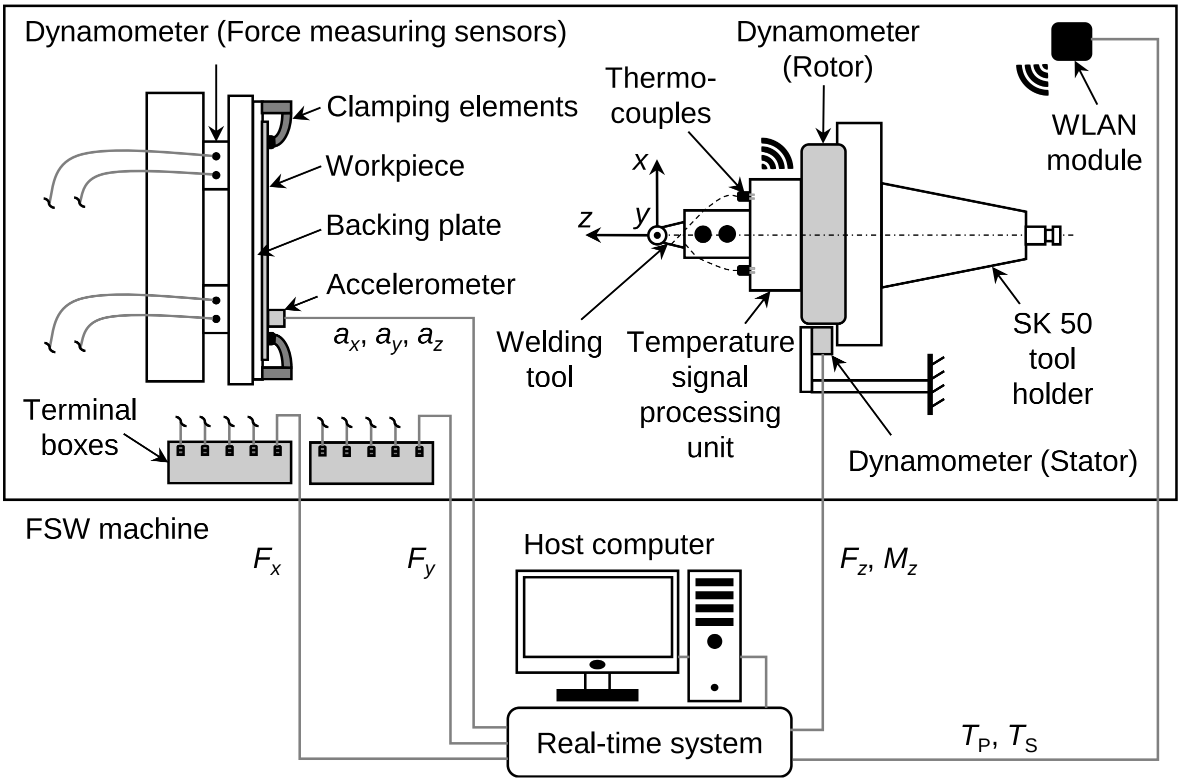

Figure 4.4: Schematic representation of the experimental setup with real-time system and host computer (based on KRUTZLINGER ET AL. 2015)

Non-destructive testing – surface properties: An EOS 60D digital camera from Canon Deutschland GmbH (Krefeld, Germany) with a CMOS sensor and a Canon EF-S 18 – 135 mm lens were employed to capture the images for publication P1. The images were acquired in a light tent. The camera was attached to a tripod to photograph the sheets containing the welds from above. The lateral and the rear illumination of the light tent were switched on. There was no illumination from above to avoid a pronounced shadow of the camera on the images. The image resolution was 5184 × 3456 pixels.
The recording of the topography of the welds, which was required for the investigations of all six publications, was conducted with a three-dimensional profilometer VR-3100 from Keyence Deutschland GmbH (Neu-Isenburg, Germany). The principle of operation of the profilometer was based on phase-coded structured light projection (cf. Subsection 2.3.3). The smallest measurable difference of the topography perpendicular to the sheet surface was 1 µm. The distance between the individual topography points in the plane of the sheet surface was approximately 24 µm. When using a sheet thickness of 4 mm, the weld seam width on the surface was about 14 mm, as the shoulder diameter was 14 mm. As the distance between the individual topography points on the plane of the sheet surface was around 24 µm, roughly 250,000 topography points were generated for each 10 mm long weld segment.

Destructive testing: Transverse tensile tests were performed utilizing the welds from Study 11 to determine the tensile strength of the welds for publications P5 and P6 as well as the elongation at break of the welds for publication P5. The aluminum alloy EN AW-6082-T6 was employed for P5 and P6. A period of 7.5 weeks was scheduled between the welding process and the tensile tests. It was assumed that potential post-weld aging was completed after this duration (BACHMANN ET AL. 2018). For the tensile tests, a Z050 AllroundLine material testing machine from the manufacturer ZwickRoell GmbH & Co. KG (Ulm, Germany) was utilized. A laserXtens 7-220 HP laser extensometer was used to measure the elongation at break. The geometry of the tensile specimens followed the specifications of DIN 50125, form E (see Figure 4.5). The sheet thickness t_S was 4 mm, the specimen width in the reduced area was 15 mm, and the length of the reduced area was 70 mm. The tensile tests were performed according to ISO 4136 and ISO 6892-1.

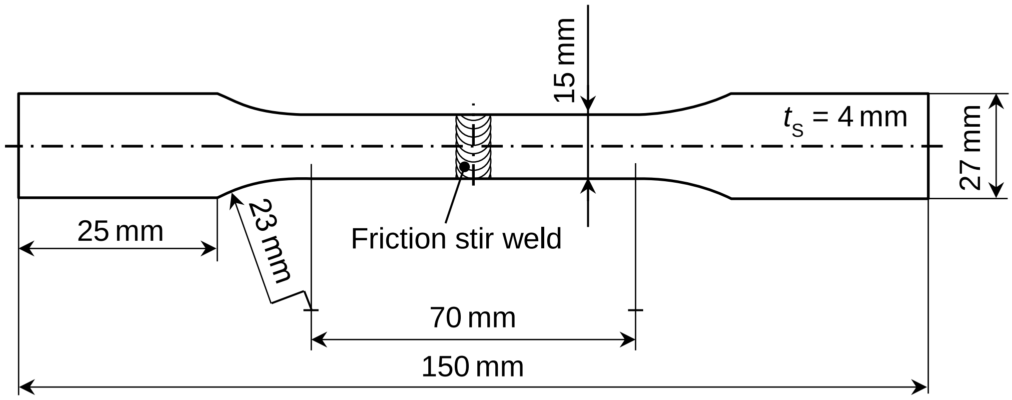

Figure 4.5: Geometry and dimensions of the tensile specimens (based on DIN 50125)

Metallographic examinations were conducted on individual welds to investigate the weld surface and internal properties more closely for publications P2, P5, and P6. Both cross sections and longitudinal sections were produced for this purpose. The samples were embedded in an epoxy system to stabilize the surface characteristics created during welding and to prevent damage during grinding and polishing. The embedded samples were wet planar ground with silica carbide abrasive paper and were polished by using fine diamond suspension. Finally, the samples were etched with Kroll's etchant, which is described in VANDER VOORT (2004). The cross sections were recorded using the image mode of the three-dimensional profilometer VR-3100 from Keyence Deutschland GmbH (Neu-Isenburg, Germany). The longitudinal sections were analyzed employing the MM-40 measuring microscope from Nikon (Tokyo, Japan).

Additional hardness tests were conducted for P5. Following SUENGER ET AL. (2014), the hardness measurements were performed according to Vickers and were placed along a centerline of the sheet thickness with a distance of 1 mm between the individual measuring points (see Figure 4.6). The microhardness tester LM-100AT from Leco Corporation (St. Joseph, MI, USA) was used. The tests were performed according to the requirements of the ISO 6507-1 standard.

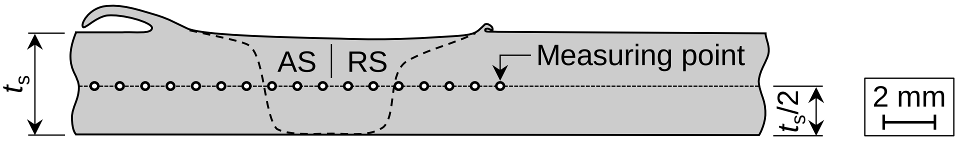

Figure 4.6: Schematic illustration of the locations of the hardness measuring points (based on SUENGER ET AL. 2014)

Data processing: For data processing, data transformation, data mining, and the evaluation of the performance of the algorithms according to the KDD process (cf. Subsection 2.4.1), primarily the software packages Matlab (MathWorks Inc., Natick, MA, USA) and Python (Python Software Foundation, DE, USA) were used. Appendix A.3 lists the most important software and frameworks employed for the various publications. The components of the computer architecture utilized for the training, validation, and testing of the computationally intensive ANNs are listed in Table 4.3.

Table 4.3: Workstation used for the computations of the ANNs (based on HARTL ET AL. 2019b)

Operating system	CPU	RAM	GPU	VRAM	CUDA compute capability
Windows 10 Education	AMD Ryzen 7 1700X Eight-Core Processor 3.40 GHz	32 GB	NVIDIA Quadro P5000	16 GB	6.1 (NVIDIA CORPORATION 2020)

5 Research Findings

5.1 Chapter overview

In this chapter, the research results are described, which were obtained following the methodological procedure outlined in Section 4.3. The research findings are presented in the form of embedded publications (P1 to P6). In Section 5.2, the publications P1, P2, and P3, which focus on the automated detection and prediction of surface properties, are briefly summarized, and the most important findings are mentioned. Section 5.3 contains a summary of the results of publication P4 on the optimization of the surface topography by using RL and BO. Section 5.4 provides information on the correlations between the surface topography and the tensile strength (P5) and on the prediction of the tensile strength through GPR (P6). Finally, the work performed is evaluated with respect to the scientific objectives defined in Section 4.2.

5.2 Detection of surface defects and properties

5.2.1 Publication 1: Detection of surface defects based on image information

For publication P1, deep learning methods were applied to detect friction stir welds and classify the surface defects by employing images. For this purpose, 112 welds with different surface properties and a total length of approximately 18.4 meters were produced (see Table 4.2). Color images of the welds were taken with a digital camera, and topography images were generated utilizing a three-dimensional surface profilometer (cf. Section 4.5). Figure 5.1 displays a comparison of a color image and a topography image of the same weld.

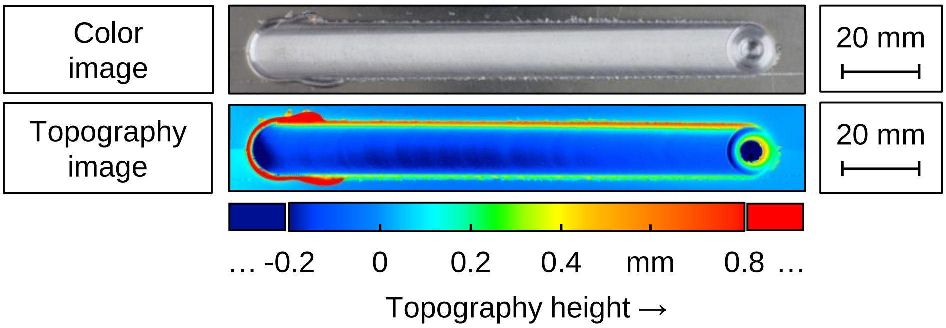

Figure 5.1: Color image and topography image of the same weld (based on Hartl et al. 2019b)

The pursued approach comprised two steps, *detection* and *classification*:

Detection: In the first step, the welds were recognized by utilizing the color images and applying the CNN-based object detection algorithm YOLOv2 (cf. Subsection 2.4.2). The topography images only contained the weld seam and no significant surrounding area. Thus, this first step was only necessary for the color images but not for the topography images. Both the tiny version and the full version of the YOLOv2 algorithm were tested to detect the welds. The former contained nine convolutional layers, and the latter contained 23 convolutional layers. To train and test the object detection algorithm, 40 images each containing none, one, or two welds were taken (on the images without a weld, the algorithm should not indicate a weld either). Out of the 120 images, 96 were used for training and 24 for testing the algorithm. Using this data set, better results were achieved by employing the tiny version, whereby an IOU of 82.4 % was reached. Afterwards, the amount of data available for training was increased by data augmentation (cf. Subsection 2.4.2) according to the following procedure:

1. Copying the original images containing one and two welds ten times to have a total of 736 images for training instead of initially 96 images
2. Randomly cutting the copied images (the welds were still completely contained in the images)
3. Randomly mirroring the copied and cut images horizontally

With the obtained larger amount of training data, the results could be improved using the YOLOv2 full version and an IOU of 89.5 % was achieved. For a benchmark, the human performance was also determined. The human repeatability in the detection of the welds, respectively in the attachment of the ground-truth bounding boxes (see Figure 2.14), was determined, and an IOU of 94.2 % was reached. After applying the data augmentation technique, the full version of the YOLOv2 object detection algorithm thus achieved 95.0 % of the human performance.

Classification: In the second step, the surface properties of the welds were classified. Both the color images and the topography images were used now, and the results were compared. For the classification, the images of the welds were divided into ROI (cf. Section 3.2) with a length of 100 pixels and a height of 300 pixels. This resulted in 8640 color images and 8640 topography images of the ROI that were available for training, validation, and testing of the CNNs. Each image of an ROI was assigned one property for each of the following three parent categories based on a human visual evaluation:

- Flash formation: Acceptable or excessive
- Weld face: Acceptable, surface galling, or surface lack of fill
- Welding temperature: Adequate, excessive, or insufficient

Seven different CNN architectures were tested (cf. Subsection 2.4.2): AlexNet (KRIZHEVSKY ET AL. 2013), DenseNet-121, ResNet-18 and ResNet-152 (HUANG ET AL. 2017), SqueezeNet 1.0 (IANDOLA ET AL. 2017), VGG-11 (SIMONYAN & ZISSERMAN 2015), and a custom-built CNN. As expected, better results were achieved with the topography images than by using the color images. The topography images contain information about the contour of the surface patterns and information regarding the height of the surface patterns; the color images show just the contours. The best classification results, when using the test data set, were achieved by the DenseNet-121 CNN. The accuracy for the color images contained in the test data set was 86.7 %, and the accuracy for the topography images was 92.1 %. Again, the human performance was determined for comparison. The human repeatability in the classification of the surface properties was 93.3 % for the color images and 93.9 % for the topography images. Thus, when classifying the surface properties of the friction stir welds on the basis of the topography images by using CNNs, 98.1 % of the human performance level was achieved. In Table 5.1, the results of the detection of the friction stir welds and the classification of surface properties by means of image information are summarized. To achieve a statement regarding the quality of the entire weld, the obtained categories for the individual weld segments (ROI) can be combined and evaluated by the FSW user.

Table 5.1: Results of the detection and classification of friction stir weld surfaces using images (based on HARTL ET AL. 2019b)

Detection (IOU)	**Without data augmentation**	**With data augmentation**
YOLOv2 (tiny version)	82.4 %	81.6 %
YOLOv2 (full version)	80.2 %	**89.5 %**
Human	94.2 %	
Classification (Accuracy)	**Color images**	**Topography images**
DenseNet-121 (best CNN)	86.7 %	**92.1 %**
Human	93.3 %	93.9 %

Finally, the two steps detection and classification were applied in cascade on color images, whereby the functionality of the automated visual inspection using CNNs was demonstrated. When using the workstation described in Table 4.3, the computation time required to detect a weld on a color image was 210 ms and the classification of an ROI took 10 ms. This constituted a significant improvement compared to the state of the art, according to which it took 3.9 s to classify one frame (cf. Section 3.2).

The most important findings in HARTL ET AL. (2019b) were the following:

- CNN-based object detectors are well suited for the recognition of friction stir welds on aluminum sheets and almost achieve human performance.
- CNNs are well suited for the classification of the surface properties of friction stir welds by color or topography images. By using topography images, the results obtained are comparable to human performance.

Contributions of the authors

Roman Hartl was the leading investigator and author of the published conference paper. He developed the idea of applying CNNs to detect the surface properties, defined the experimental plan for the welding experiments and supervised them, and selected the applied algorithms. He performed the calculations and evaluated the results. Additionally, he wrote the paper while receiving feedback from the co-authors. Finally, he presented the results within the scientific conference *SPIE Optical Metrology* (Volume 11059) in Munich, Germany. In an interdisciplinary student research project, Johannes Landgraf and Julian Spahl performed the programming of the software for the detection and classification of the welds. Andreas Bachmann originally proposed the concept of automatically detecting surface defects on friction stir welds. All authors discussed the findings and commented on the results.

5.2.2 Publication 2: Detection of surface defects based on topography data

The results from publication P1 only allowed a classification of the surface features, but no quantification. This constraint was resolved during the work leading to publication P2 by evaluating the weld topography. The surface topographies of 32 welds (see Table 4.2) with different surface properties were recorded using a three-dimensional profilometer. This resulted in point clouds containing about 1.5 million height information points for the evaluated 50 mm long surface segment, named Area A (see Figure 5.2 (a)). The aim was to define key indicators for the quantification of the surface features and defects of friction stir welds based on the topography. For this purpose, statistical operations, such as the calculation of maxima, minima, or standard deviations, along with indicators from surface metrology were employed to derive suitable key indicators from the three-dimensional point clouds. The following areas were found to be suitable for the calculation of the key indicators (see Figure 5.2 (a) and (b)):

- Area A was analyzed to quantify the flash formation, the surface lack of fill, and the weld seam width.
- Area B was used to specify the amount of surface galling.
- The weld centerline was evaluated to characterize the semicircular arc texture formation.

The weld seam width w was defined as the distance between the flash on the AS and the flash on the RS. A total of 2123 cross sections were available for the topography of each weld. This number resulted from the distance of the topography points in the x-y-plane of approximately 24 µm (cf. Section 4.5) and the length of the evaluated weld segment of 50 mm. From the corresponding 2123 values, the following indicators were calculated:

- For the flash height f, the maximum f_{max} and the standard deviation S_f were calculated to rate the amount and the regularity of the flash formation.
- For the seam underfill u, the standard deviation S_u was computed to assess the amount of the surface lack of fill.
- For the weld seam width w, the standard deviation S_w was determined to evaluate the regularity of the weld seam width.

Furthermore, it was discovered that the peak material volume V_{mp} according to ISO 25178-2 is suitable to quantify occurring surface galling on the weld surface.

Figure 5.2 (c) schematically depicts the topography along the weld centerline. Due to the seam underfill, the topography along the weld centerline is usually below the sheet surface. For each weld, the standard deviation S_d of the differences d_arc between the heights of the local valleys and the subsequent local peaks was calculated along the evaluated 50 mm long weld centerline. Additionally, the number of local peaks and local valleys along the weld centerline was counted (n_count) and compared with the theoretical number (n_theoret), which led to a ratio that was called r_arc:

$$r_\mathrm{arc} = \frac{n_\mathrm{count}}{n_\mathrm{theoret}} \; . \tag{5.1}$$

The theoretical number of local peaks and local valleys n_theoret corresponds to the number of semicircular arcs according to Equation 2.2. The evaluation of the semicircular arc texture along the weld centerline proved to be particularly suitable for the evaluation of the surface topography. If the ratio r_arc was 1, then the surface arc texture was regular and the surface quality of the weld was high. If r_arc was higher than 1, then the ratio of the tool rotational speed n to the welding speed v was small, which correlates to an insufficient welding temperature. If r_arc was smaller than 1, then the ratio of the tool rotational speed n to welding speed v was high, which corresponds to an excessively high welding temperature (cf. Subsection 2.3.3). The seven topography indicators defined in P2, to characterize the topography, are listed in Table 5.2.

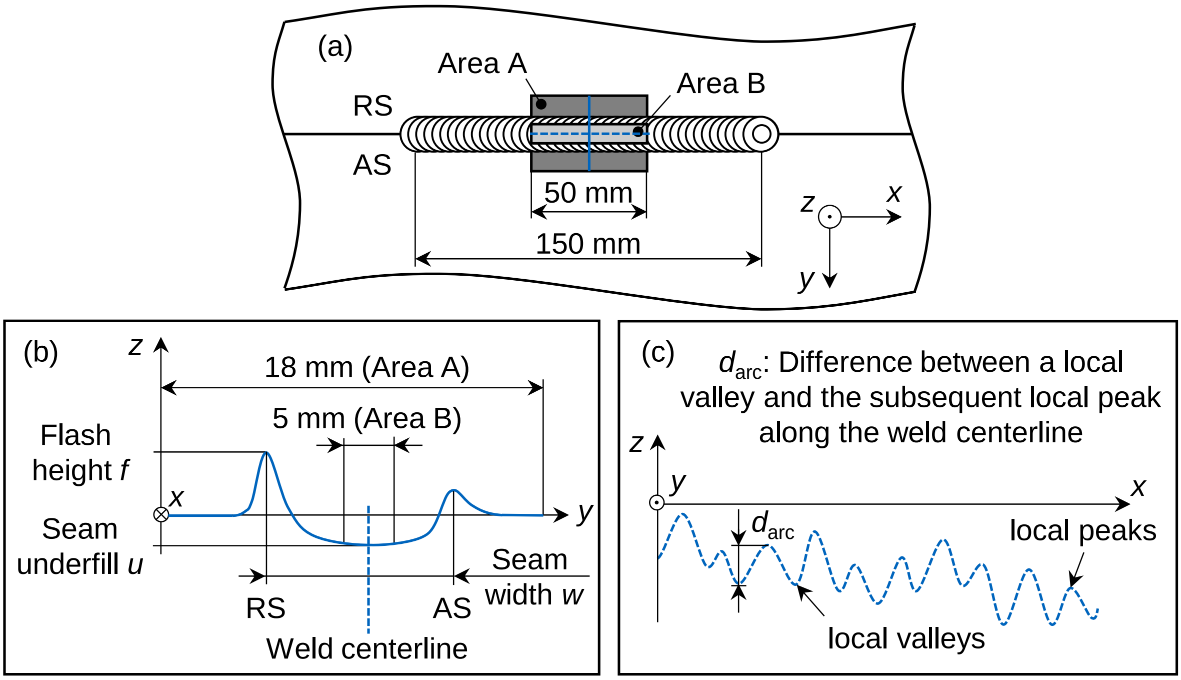

Figure 5.2: (a) Section of the sheet surface containing the friction stir weld; (b) exemplary cross section of the surface topography; (c) topography along the weld centerline (based on HARTL ET AL. *2019a)*

Table 5.2: Summary of the defined scalar key indicators to quantify and detect surface properties and defects of friction stir welds (based on HARTL ET AL. *2019a)*

Surface defect	Key indicator 1	Key indicator 2
Flash formation	Maximum flash height: f_{max}	Standard deviation of the flash height: S_f
Surface lack of fill	Standard deviation of the seam underfill: S_u	–
Irregular weld seam width	Standard deviation of the weld seam width: S_w	–
Surface galling	Peak material volume: V_{mp}	–
Irregular arc texture formation	Standard deviation of the differences between the heights of the local peaks over the subsequent local valleys along the weld centerline: S_d	Ratio between the counted number and the theoretical number of local peaks and local valleys along the weld centerline: r_{arc}

The key indicators in Table 5.2 enable a quantification of the surface properties of friction stir welds. By defining threshold values for the indicators, it is possible to automatically detect surface defects.

The most important findings in HARTL ET AL. (2019a) were the following:

- The surface properties and defects of friction stir welds can be quantified and detected on the basis of scalar key indicators derived from the three-dimensional point cloud of the surface topography.
- The ratio r_{arc}, which was defined as the ratio between the counted number and the theoretical number of local peaks and local valleys along the weld centerline, is well suited for the evaluation of the surface quality.

Contributions of the authors

Roman Hartl was the primary investigator and author of the published conference paper. He developed the idea of quantifying the surface properties on the basis of the topography and defined the required welding experiments, which were conducted under his supervision. He recorded and evaluated the topography data. Roman Hartl wrote the paper, while receiving feedback from the co-authors. Finally, he presented the results within the *21st Chemnitz Seminar on Materials Engineering 2019* in Chemnitz, Germany. All authors discussed the findings and commented on the results.

5.2.3 Publication 3: Prediction of surface defects based on process variables

In publication P3, it is described how the surface properties and defects can be predicted by evaluating the process variables. This represents an indirect approach for monitoring the surface quality, in contrast to the methods outlined in the publications P1 and P2, which are based on the direct recording of the weld surface. Indirect monitoring via the process variables offers the advantage that it is not sensitive to external influences such as different illumination conditions or dust formation (cf. Subsection 2.3.3).

Studies 5, 6, and 8 (see Table 4.2) were utilized for the investigations in publication P3. During the welding experiments, a total of nine different process variables were recorded (see Figure 4.4):

- Accelerations in three spatial directions: a_x, a_y, and a_z
- Process forces in three spatial directions: F_x, F_y, and F_z
- Spindle torque: M_z
- Temperatures at the tool probe and shoulder: T_P and T_S

The labeling of the data was performed in two ways. The placement into “good” and “defective” was based either on a simple human visual inspection of the welds (Case 1) or on the following eight topography key indicators that were based on the findings from publication P2 (Case 2):

- Mean flash height: f_m
- Mean seam underfill: u_m
- Standard deviation of the flash height: S_f
- Standard deviation of the seam underfill: S_u
- Standard deviation of the differences between the heights of the local peaks over the subsequent local valleys along the weld centerline: S_d
- Ratio between the counted number and the theoretical number of local peaks and local valleys along the weld centerline: r_arc
- Peak material volume: V_mp
- Standard deviation of the weld seam width: S_w

Each weld was divided into 17 ROI, each with a length of 10 mm. In contrast to Case 1, where all 17 ROI of the same weld were labeled identically on the basis of the human visual inspection, in Case 2, the labeling was performed individually for each ROI. The labeling of the data in Case 1 was thus simpler, but less accurate. First, three different main types of ANNs were tested for their ability to predict the surface properties through evaluation of the axial process force F_z (see Figure 2.6): FCNNs, RNNs, and CNNs (cf. Subsection 2.4.2). The information value of the input data for these three major types of ANNs increased in this order from the FCNNs to the RNNs and to the CNNs:

- **One-dimensional:** The FCNNs only received scalar values derived from the time course of the process variables in the respective 10 mm long weld segment, for example, the mean temperature at the tool shoulder.
- **Two-dimensional:** The RNNs received the complete time series of the process variables.
- **Three-dimensional:** For the CNNs, the time series of the process variables were converted into spectrograms using the fast Fourier transform. Spectrograms are images that contain the signal density as a function of time and frequency (RAO & SWAMY 2018, p. 747).

The best results were achieved using the CNNs. It was assumed that the reason for this is the higher information value of the inputs compared to the FCNNs and RNNs. In the next step, not only the axial force F_z but also the eight remaining process variables were evaluated using the CNNs. The result of the human visual inspection (Case 1) was best predicted with an accuracy of 99.1 % by evaluating the F_y signal. When predicting the quality of the topography (Case 2), the spindle torque M_z led to the best result with an accuracy of 87.4 %. It was assumed that the better result for the prediction of the human visual inspection compared to the prediction of the topography analysis was due to the simpler, but also less accurate way of labeling the data. Further investigations regarding the classification included the influence of the sampling rate of the process variables on the prediction accuracy and a test of a trained CNN on welds produced using a different aluminum alloy. It was shown that the variation of the sampling rate between 40 Hz and 9600 Hz has no significant influence on the accuracy when CNNs are used. The application of the trained network to a different aluminum alloy revealed itself to be a problem, whereby the results can be improved with a deeper CNN that contains more layers.

Finally, it was investigated how well the topography indicators can be predicted using a regression CNN. As stated in Subsection 2.4.1, regression allows the prediction of real values associated with the input instead of categories. Mean PCCs higher than 0.80 were obtained for the prediction of the mean flash height f_m and the semicircular arc texture ratio r_arc. These topography key indicators can therefore be predicted most accurately.

The most important findings in HARTL ET AL. (2020d) were the following:

- CNNs are well suited for the evaluation of process variables in FSW. For this purpose, spectrograms can be generated from the time series of the process variables.
- It is possible to predict the surface quality by evaluating the process variables.
- The mean flash height f_m and the ratio r_arc can be predicted well by evaluating process variables.

Contributions of the authors

Roman Hartl was the major investigator and author of the published journal article. He developed the idea for the indirect monitoring of the surface quality of friction stir welds by means of process variables and defined the experimental plan for the welding experiments, which were performed under his supervision. Roman Hartl wrote the article while receiving feedback from the co-authors. Additionally, he presented the results within the *1st International Conference on Advanced Joining Processes* in Ponta Delgada, Portugal. In his master's thesis work, Benedikt Praehofer conducted the welding experiments and contributed significantly to the programming for the application of the ANNs. Based on his idea to generate spectrograms, the utilization of CNNs in this publication became possible. All authors discussed the findings and commented on the results.

5.3 Optimization of the topography

5.3.1 Publication 4: Data pre-processing

After the focus in publications P1 to P3 was on the automated recognition and prediction of surface properties, in publication P4, the surface topography was optimized by applying ML-based algorithms that are able to deal with the exploration-exploitation dilemma (cf. Subsection 2.4.4). A total of 262 welds from ten different experimental studies were utilized for P4 (see Table 4.2). Before the topography could be optimized, it was necessary to define a suitable single scalar key indicator, which quantifies the surface quality. For this purpose, the same eight topography indicators as in publication P3 (f_m, u_m, S_f, S_u, S_d, r_arc, V_mp, and S_w) were selected, scaled to values N between 0 and 1 (whereby 0 was the ideal value, i. e. no surface defect appeared, and 1 was the worst occurring value, i. e. a pronounced surface defect appeared), summed up, and divided by the number of topography indicators:

$$def = \frac{N_{f_\mathrm{m}} + N_{u_\mathrm{m}} + N_{S_\mathrm{f}} + N_{S_\mathrm{u}} + N_{S_\mathrm{d}} + N_{r_\mathrm{arc}} + N_{V_\mathrm{mp}} + N_{S_\mathrm{w}}}{8} \tag{5.2}$$

The eight topography indicators were thus combined into one single scalar value that took into account the various surface features. This key indicator is a dimensionless measure for the amount of surface defects of a friction stir weld and was called *def*. The values for *def* varied between 0.021 (best occurring value) and 0.603 (worst occurring value) for the 262 welds from the ten conducted studies. Figure 5.3 depicts color and topography images of these two welds.

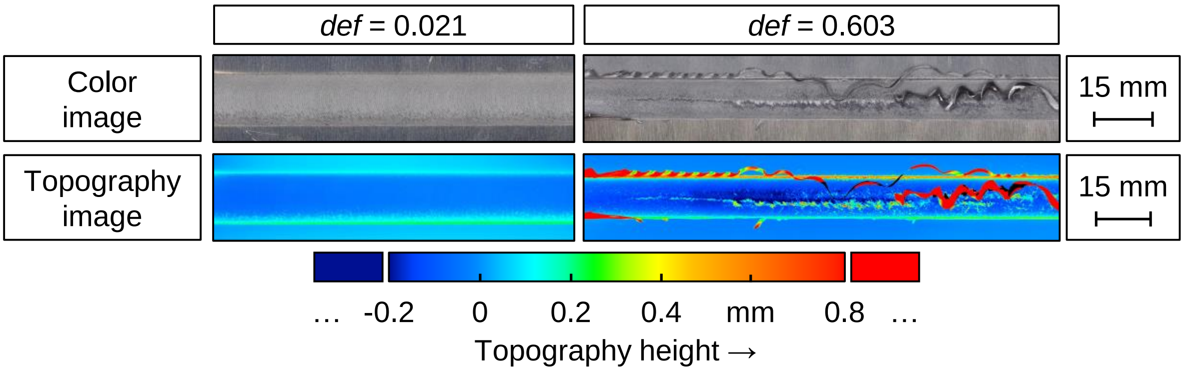

Figure 5.3: Color image and topography image of the welds with the best and the worst values for def (based on HARTL ET AL. 2020b)

The aim in publication P4 was to minimize the function for the surface defects $def(v, n)$ as efficiently as possible, that is, by testing as few parameter combinations of the welding speed v and the tool rotational speed n as possible. For this purpose, RL and BO were tested.

5.3.2 Publication 4: Optimization of the topography by reinforcement learning

The algorithm initially used was RL, and the optimization problem was modeled as an MDP (cf. Subsection 2.4.5). Two formulations were implemented, which differed in the state transition functions and the possible actions. In Formulation 1, in each action, the welding speed or the tool rotational speed could be increased or decreased by only one step, as with the agent in Figure 2.23 (b). In Formulation 2, any combination of the two process parameters could be tested next. Both formulations were solved by value iteration. The fact that the optimization problem can be solved with both Formulation 1 and Formulation 2 was demonstrated in publication P4 by using Study 1 (the findings for the other nine experimental studies correlated well with that). Figure 5.4 (a) shows the 16 values for *def* from Study 1. The optimum, meaning the best surface topography in Study 1, is reached at a welding speed *v* of 500 mm/min and a tool rotational speed *n* of 1500 min^{-1}. For Formulation 1, the algorithm terminated after five iterations, and for Formulation 2, it terminated after two iterations. In Figure 5.4 (b), the respective actions for the various states are displayed for Formulation 1, after the value iteration algorithm terminated. The optimal path leading from the parameter set with a welding speed of 1500 mm/min and a tool rotational speed of 3500 min^{-1} to the optimum ("○" sign) is marked in gray.

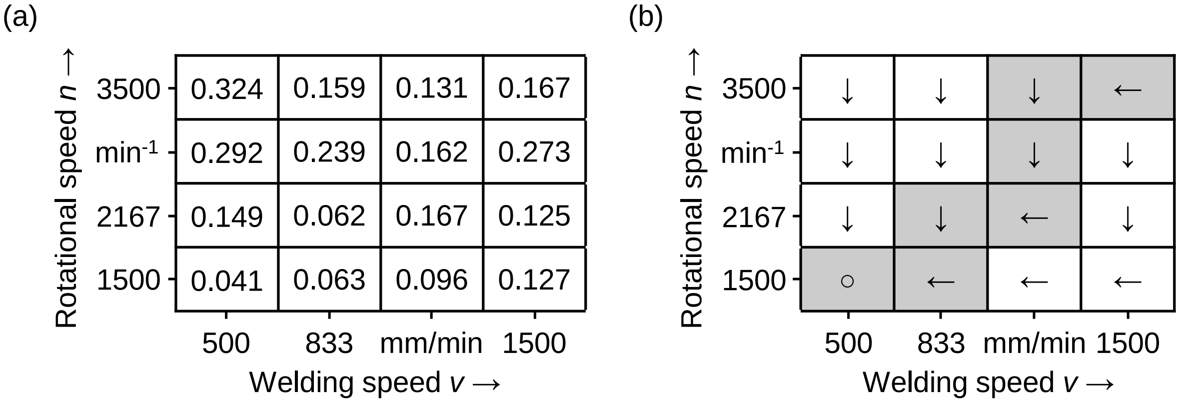

(a)

	500	833	mm/min	1500
3500	0.324	0.159	0.131	0.167
min^{-1}	0.292	0.239	0.162	0.273
2167	0.149	0.062	0.167	0.125
1500	0.041	0.063	0.096	0.127

(b)

	500	833	mm/min	1500
3500	↓	↓	↓	←
min^{-1}	↓	↓	↓	↓
2167	↓	↓	←	↓
1500	○	←	←	←

Figure 5.4: *(a) Values for the scaled and averaged surface topography indicator def for Study 1; (b) corresponding optimal actions according to Formulation 1 (based on* HARTL ET AL. *2020b)*

The optimization problem can therefore be solved by using RL. However, this approach was not efficient. Since all states and all actions were reiterated, the function *def* had to be evaluated for all parameter combinations of welding speeds *v* and tool rotational speeds *n*.

5.3.3 Publication 4: Optimization of the topography by Bayesian optimization

After the solution of the optimization problem through RL resulted in inefficiency, subsequently BO (cf. Subsection 2.4.4) was used to optimize the topography, that is, to minimize the function *def* by finding suitable values for the welding speed *v* and the tool rotational speed *n* for each of the ten employed studies. Both the *expected improvement* and the *probability of improvement* were tested as acquisition functions. Two different approaches, called single-task and multi-task, were developed:

- In the single-task approach, the algorithm received no information regarding the other nine studies. As one consequence, the algorithm had no information for the initial selection of a parameter set, and this first selection had to be made randomly.
- For the multi-task approach, the information from the nine other studies (the aluminum alloy, the sheet thickness, the tool shoulder geometry, the study number, the tool welding and rotational speed, and the corresponding values for *def* for each experiment) was provided. Already at the first trial in each study, the algorithm was able to make use of information from the nine other studies. The selection of the first parameter set to be tested was therefore no longer random as in the single-task approach.

In Figure 5.5, the GP and the expected improvement acquisition function are visualized for Study 1, after three process parameter sets were tested with the multi-task approach. The optimum at a welding speed of 500 mm/min and a tool rotational speed of 1500 min^{-1} was already found in the first three steps. A full three-dimensional surface plot can be found in Appendix A.4.

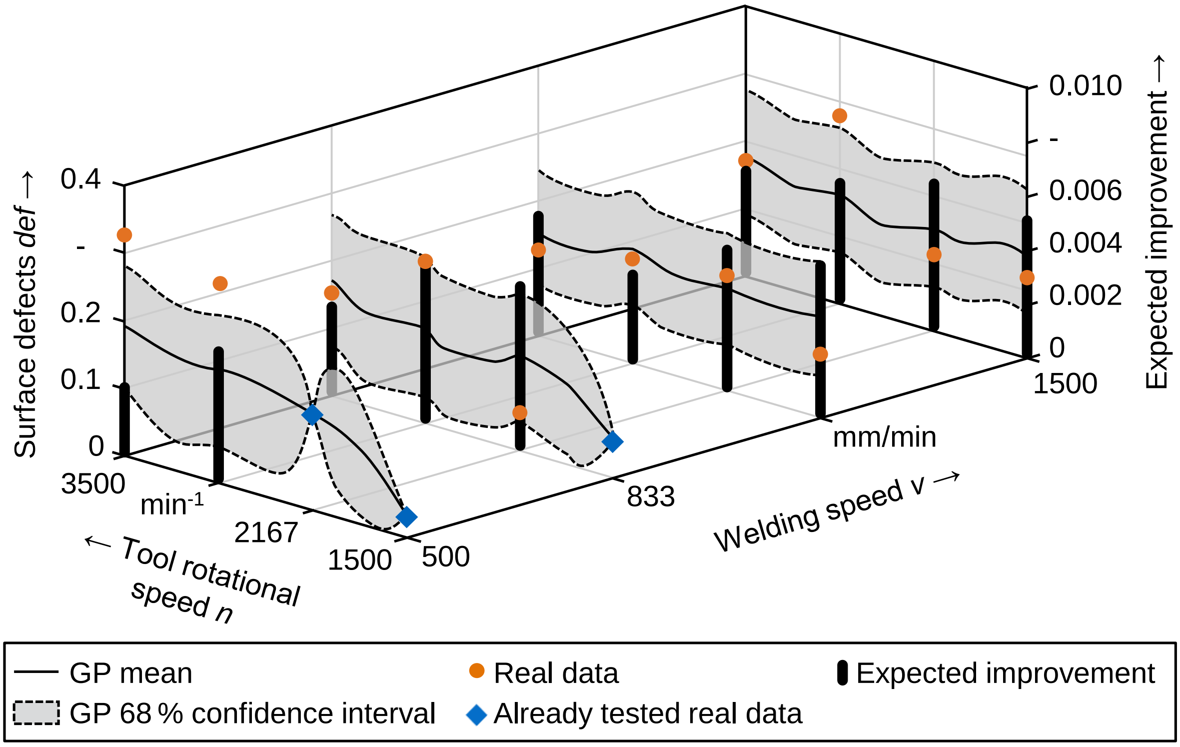

Figure 5.5: Visualization of the GP and the acquisition function after three tested parameter sets in Study 1 with the multi-task approach (based on HARTL ET AL. 2020b)

A random search algorithm was used as a benchmark to evaluate the performance of the BO algorithms. Overall, the single-task approach found suitable parameter sets approximately 30 % faster than the random search algorithm. The multi-task approach was about 50 % faster than the random search algorithm. Thus, the functionality and suitability of BO for the optimization of the surface topography could be demonstrated. The differences between the two applied acquisition functions were negligible.

Additionally, through penalizing low welding speeds, a possibility to balance between the two requirements of a high surface quality and a high welding speed was realized. This allows for a more economical production of friction stir welds.

The most important findings in HARTL ET AL. (2020b) were the following:

- The surface topography can be optimized by RL or BO.
- In contrast to RL, BO is quite efficient for finding suitable process parameters and outperforms random search algorithms.
- By providing information from other experimental studies that have already been conducted, the BO algorithm can find suitable parameters even faster.
- In addition to the surface quality, the welding speed can also be accounted for to produce welds more economically when applying the BO.

Contributions of the authors

Roman Hartl was the leading investigator and author of the published journal article. He proposed optimizing the surface topography of friction stir welds by using ML-based algorithms. He planned and supervised the welding experiments, performed the calculations, and interpreted the results. He wrote the article while receiving feedback from the co-authors. In an interdisciplinary student research project, Julius Hansjakob performed the programming of the optimization algorithms. He had the idea of applying BO. All authors discussed the findings and commented on the results.

5.4 Prediction of the mechanical properties

5.4.1 Publication 5: Correlations between the topography and mechanical properties

The objective within publication P5 was to determine, if there are correlations between the surface topography and the mechanical properties of friction stir welds. For this purpose, a total of 54 welds were produced at three different welding speeds using the aluminum alloy EN AW-6082-T6: 500 mm/min, 1000 mm/min, and 1500 mm/min (see Table 4.2). Four tensile specimens and one cross section were removed from each weld, which resulted in a total of 216 tensile specimens and 54 cross sections. The correlations between topography indicators based on publication P2 and the three mechanical properties tensile strength, elongation at break, and Vickers hardness were investigated.

Pronounced correlations were discovered for the tensile strength when a welding speed of 500 mm/min was applied and extremely low and extremely high tool rotational speeds, which are not relevant for industrial applications, were excluded from the data set. The highest correlation was found between the mean seam underfill u_m and the tensile strength R_m, whereby a PCC of -0.90 was achieved (see Figure 5.6 (a)). The higher the seam underfill is, the lower is the tensile strength. That relation is reasonable: The higher the seam underfill of the friction stir weld is, the smaller is the joining cross section and the weaker is the welded joint. For the mean flash height f_m, the correlation was -0.84. The more pronounced the flash formation is, the lower is the tensile strength of the friction stir weld. Additionally, it was discovered that the highest tensile strength of friction stir welds is achieved when the ratio r_{arc}, which is defined in publication P2, is in the vicinity of 1. This is valid independent of the welding speed (see Figure 5.6 (b)) and is a necessary condition for achieving a high tensile strength. In publication P2, it was already shown that visually good welds are produced when the r_{arc} ratio is close to 1.

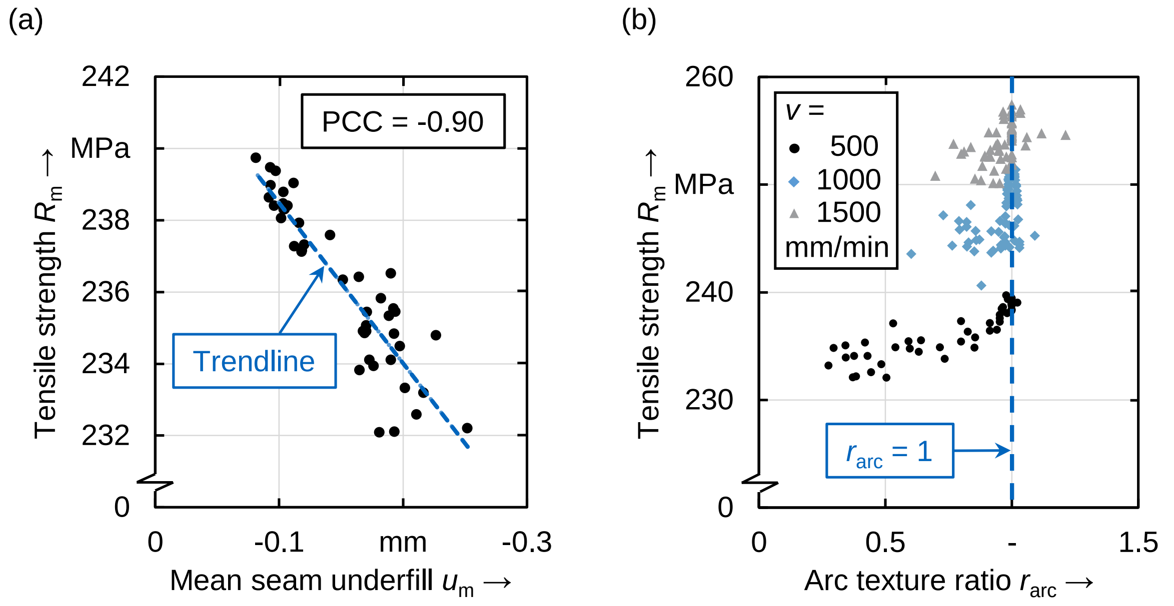

Figure 5.6: *(a) Tensile strength R_m dependent on the seam underfill u_m at a welding speed of 500 mm/min; (b) tensile strength R_m dependent on the arc texture ration r_{arc} at different welding speeds (based on HARTL ET AL. 2020a)*

In summary, there are correlations between the surface topography and the tensile strength of friction stir welds, especially at low welding speeds. At the higher welding speeds of 1000 mm/min and 1500 mm/min, the correlations were much less pronounced. The correlations between the topography and the other two mechanical properties, elongation at break and Vickers hardness, were low for all three investigated welding speeds.

The most important findings in HARTL ET AL. (2020a) were the following:

- For low welding speeds, there are pronounced relations between the surface topography and the tensile strength for a large interval of tool rotational speeds. These correlations can be quantified using scalar key indicators for the topography. The strongest correlation prevails between the seam underfill and the tensile strength.
- The highest tensile strength of friction stir welds is achieved when the ratio r_{arc} is in the vicinity of 1. This is valid independently of the welding speed. In addition, as discovered in publication P2, the surface quality is good if r_{arc} is close to 1.

Contributions of the authors

Roman Hartl was the primary investigator and author of the published journal article. He developed the idea to analyze the relations between the surface topography and the mechanical weld properties. He also defined the experimental plan, supervised the welding experiments, analyzed the data, and interpreted the results. Roman Hartl wrote the article while receiving feedback from the co-authors. In his master's thesis work, Fabian Vieltorf performed the welding experiments and the tensile tests. Additionally, he prepared the topography data and the data obtained from the tensile tests. All authors discussed the findings and commented on the results.

5.4.2 Publication 6: Prediction of the tensile strength by topography data

Once it was demonstrated in publication P5 that there are pronounced correlations between the surface topography of friction stir welds and their tensile strength, the objective for publication P6 was to enable the prediction of the tensile strength by evaluating the surface topography.

The 54 welds produced for publication P5 were also utilized in publication P6 (see Table 4.2). A five-fold cross-validation was performed, resulting in a division of the data into 80 % training data and 20 % test data. This means that the data set was divided into five parts, and in each of the five loops, a different part was employed as the test data set. Additionally, five different covariance functions were tested (cf. Subsection 2.4.3): the RBF (RASMUSSEN & WILLIAMS 2006, p. 14), the rational quadratic covariance function (RASMUSSEN & WILLIAMS 2006, p. 86), the Matérn 5/2 covariance function (RASMUSSEN & WILLIAMS 2006, pp. 84 f.), an additive covariance function according to DUVENAUD ET AL. (2012), and the spectral mixture covariance function by WILSON & ADAMS (2013).

The PCC between the true and the predicted tensile strength was identified to be the most appropriate performance indicator to assess and compare the results. Taking into account the data from the experiments with all three welding speeds, the mean PCC from the five-fold cross-validation was 0.76 when using the spectral mixture covariance function. By removing a few outliers at extremely low and extremely high tool rotational speeds, which are not of importance for industrial applications, the result improved to a PCC of 0.96 by using the spectral mixture covariance function. In Figure 5.7, the worst and the best results from the five-fold cross-validation are depicted. The five results ranged from a PCC of 0.95 to a PCC of 0.98, which was assessed as a high reproducibility.

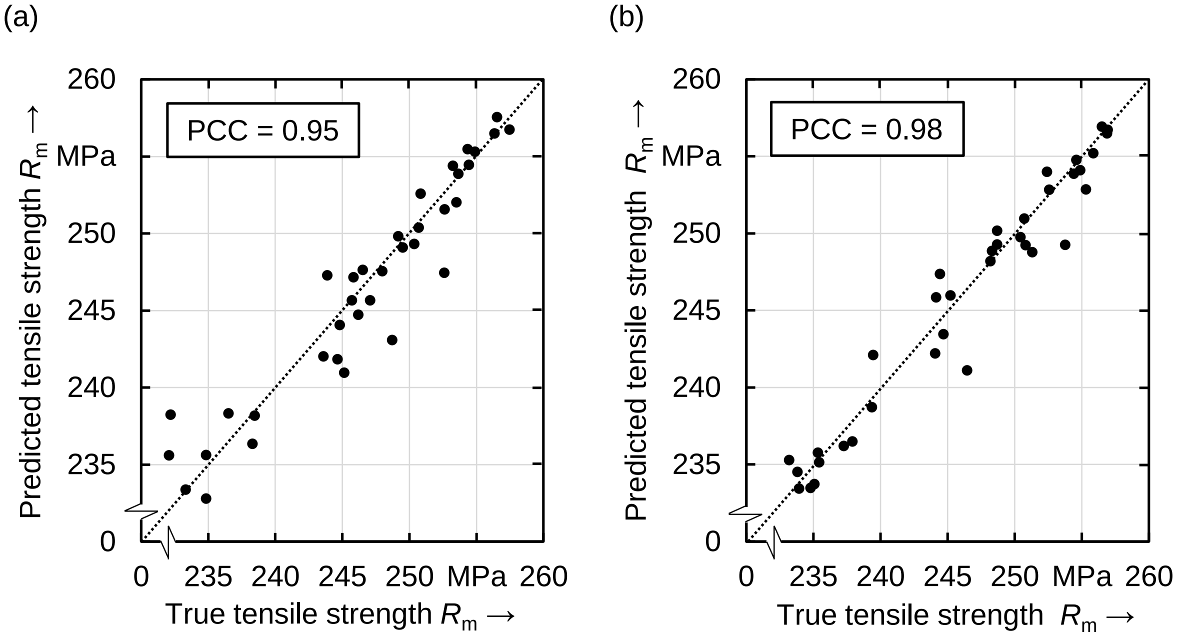

Figure 5.7: *Results with (a) the lowest and (b) the highest PCC out of the five-fold cross-validation to predict the tensile strength R_m based on the weld topography (based on HARTL ET AL. 2020c)*

This behavior correlates well with the result from publication P5, wherein the highest correlations between the topography and the tensile strength were found for a welding speed of 500 mm/min when some outliers were removed for extremely low and extremely high tool rotational speeds. As described in Subsection 2.3.3, low tool rotational speeds correlate with low welding temperatures, and high tool rotational speeds lead to high welding temperatures. If the tool rotational speed is too low or too high and thus the welding temperature is insufficient or excessive, internal weld seam defects occur. These reduce the tensile strength and cannot be detected via the surface topography. For this reason, the prediction accuracies decrease when extremely low or extremely high tool rotational speeds are applied.

When the three welding speeds were investigated individually, the correlations decreased as the welding speed increased. For 500 mm/min, the PCC was 0.94, and for 1500 mm/min, it was 0.83. This is probably due to the decreasing regularity of the material flow around the welding probe at higher welding speeds. Overall, it was demonstrated that the tensile strength can be forecasted by evaluating the surface topography, with the exception of extremely low or extremely high tool rotational speeds.

The PCCs for the prediction of the tensile strength were also determined when the process variables or the process parameters were used as input variables for the GPR model. The results were better compared to the results when evaluating the surface topography. Even experiments conducted with extremely low and extremely high tool rotational speeds did not have to be excluded from the data set to achieve good results. For both the process variables and the process parameters, the PCC between the true and the predicted tensile strength was 0.99 when considering the data from all three welding speeds.

The most important findings in HARTL ET AL. (2020c) were the following:

- The GPR is well suited for the prediction of the tensile strength of friction stir welds.
- Except under insufficient or excessive welding temperatures, the tensile strength can be predicted well by evaluating the surface topography. The prediction accuracy tends to decrease with increased welding speeds.
- By evaluating the process variables or the process parameters, the tensile strength can be predicted even better than it can be by evaluating the surface topography.

Contributions of the authors

Roman Hartl was the main investigator and author of the published journal article. He developed the idea of predicting the tensile strength based on topography data by applying the GPR and defined the methods used. He also planned and supervised the conducted welding experiments, performed the computations and evaluated the results thereof. Finally, Roman Hartl wrote the article and received feedback from the co-authors. In his master's thesis, Fabian Vieltorf conducted the welding experiments, and recorded and pre-processed the topography data and the process variables data. Additionally, he provided a large contribution to the programming of the algorithm. Maximilian Benker was consulted concerning the application of the GPR. Also in this case, all authors discussed the findings and commented on the results.

5.5 Assessment of the achievement of the scientific objective

The main objective of this thesis was an approach for automated monitoring and optimization of the surface quality of friction stir welds (see Section 4.2). This scientific objective was divided into three STs (sub-targets), the achievement of which is evaluated below:

ST1 In publications P1 to P3, three different approaches were presented to automatically and reliably identify surface properties. This was enabled by evaluating image information of the weld surface (P1), based on the surface topography (P2), and by analyzing the process variables (P3). ST1 was thus fulfilled.

ST2 In publication P4, two solutions were presented to optimize the surface quality. Both RL and BO can be applied to represent the knowledge of an experienced machine operator. The BO algorithm in particular was found to be efficient for finding suitable process parameters. ST2 can therefore also be considered as achieved.

ST3 In publication P5, it was demonstrated that at low welding speeds pronounced correlations exist between the surface topography and the tensile strength of friction stir welds. For the other two investigated mechanical properties (elongation at break and Vickers hardness), no significant interrelations with the surface topography were observed. In publication P6, GPR was successfully applied to determine the tensile strength based on the surface topography and to quantify the uncertainty of the prediction. ST3 can thus also be regarded as achieved.

In the six publications, the technical aspects of the approaches were addressed. In Chapter 6, the economic potentials will be discussed to give the reader a complete overview and provide manufacturers with guidance to make decisions regarding possible investments.

6 Analysis of the Potential of the Proposed Approaches

6.1 Chapter overview

The economic potential was analyzed separately for each of the three stages of the thesis work (cf. Section 4.3). In Section 6.2, the economic advantages resulting from the automated surface inspection of friction stir welds are described. In Section 6.3, it is then examined which economic benefits arise from the algorithm-based and efficient determination of suitable process parameters. Finally, in Section 6.4, an estimation of the economic benefits resulting from the non-destructive prediction of the tensile strength is given. It is explicitly mentioned that the stated costs and other variables were estimated with information from the literature or with information offered by manufacturers. The actual values depend on a variety of factors and may differ from the values given in this chapter. Additionally, the improved possibilities for the data-based quality control and optimization in this thesis create further advantages that cannot be quantified directly. For example, a continuous documentation of the welding quality leads to a more sound liability protection and an improved traceability of workpieces.

6.2 Advantages through automated surface inspection

Considering an increasing application of FSW on possibly up to 400,000 km of weld seam length per year until 2030 in the production of electric vehicles and especially in the production of the battery trays (PARRATT & MARTIN 2019), the automated surface inspection of friction stir welds is economically valuable especially for the automotive industry. In the following paragraphs, it is shown by calculation what the static payback period (SPP) of the rationalization measure would be, if the manual inspections of the weld surfaces were replaced by the automated surface inspection system developed in Stage 1 of this work. The SPP can be calculated based on average figures or on total figures (GOETZE ET AL. 2015, p. 42). As the cash flow surpluses are assumed to be constant over the expected economic life of the investment, the average cost method is used here. According to GOETZE ET AL. (2015, p. 42), the payback period is then defined as “the period after which the capital invested is regained from the average cash flow surpluses generated by the project.” Various assumptions were made for its calculation:

- The initial investment costs $\mathbf{C_S}$ for the automated surface inspection system were estimated to be **€30,000** in a stable market. According to a worldwide operating supplier of components for automation technology, this is approximately the price for a complete surface inspection system including the hardware (light section sensor or line scan camera), the software, and the implementation.

- The running costs for the maintenance and the service of the sensor system $\mathbf{M_S}$ were assumed to be 10 % of the investment cost (HUBER 2017, p. 145), which is **€3,000** per year.
- According to the guidelines for their expected economic lifetime (GERMAN FEDERAL MINISTRY OF FINANCE 1995), the depreciation period for optical and electronic testing equipment for production is five years, which leads to an imputed depreciation $\mathbf{D_S}$ of **€6,000** per year for a linear depreciation and no liquidation value, based on the total investment cost C_S of 30,000 €.
- The imputed interest rate R is 2 % (STOPKA & URBAN 2017, p. 388), which, **according to the average method** (ROEHRICH 2014, pp. 14 f.) and corresponding to the initial investment cost C_S of €30,000, results in imputed interests $\mathbf{I_S}$ of

$$\mathbf{I_S} = \frac{C_S}{2} \cdot R = \frac{30{,}000\,€}{2} \cdot 0.02 = \mathbf{300\,\frac{€}{a}}\ . \tag{6.1}$$

The annual costs for the automated surface inspection system thus add up to

$$\mathbf{A_S} = M_S + D_S + I_S = 3{,}000\,\frac{€}{a} + 6{,}000\,\frac{€}{a} + 300\,\frac{€}{a} = \mathbf{9{,}300\,\frac{€}{a}}\ . \tag{6.2}$$

For comparison, it is calculated how much two employees cost per year to perform the surface inspection manually in a two-shift operation. Consequently, further assumptions were necessary:

- The hourly labor costs $\mathbf{C_E}$ are assumed to be **€27**, which according to PALEN (2019) were approximately the average labor costs for the industry in the European Union in 2018.
- The number of working days per year $\mathbf{D_E}$ is assumed to be **250 days**, and the daily working time $\mathbf{H_E}$ is supposed to be **16 hr** for a two-shift operation.

Thus, the annual labor costs for a two-shift operation are

$$\mathbf{A_E} = C_E \cdot D_E \cdot H_E = 27\,\frac{€}{h} \cdot 250\,\frac{d}{a} \cdot 16\,\frac{h}{d} = \mathbf{108{,}000\,\frac{€}{a}}\ . \tag{6.3}$$

This results in an annual monetary benefit $B_{S/E}$ of the automated system of

$$\mathbf{B_{S/E}} = A_E - A_S = 108{,}000\,\frac{€}{a} - 9{,}300\,\frac{€}{a} = \mathbf{98{,}700\,\frac{€}{a}}\ . \tag{6.4}$$

The SPP is calculated by dividing the capital allocation by the average cash flow surpluses. The capital allocation is equivalent to the initial investment costs C_S. However, the average cash flow is not the same as the average benefit. For investment appraisal, the depreciation is the most relevant difference, since it is considered as a cost but is not a cash outflow. Thus, the average cash flow is determined by adding the depreciation cost back into the average benefit value. The inclusion of interest payments in the cash flows depends on whether it represents a relevant cash outflow or not. Here, it is assumed that the project is financed by debt and not by internal funds. Consequently, the interest payments represent a cost as well as a cash outflow, and thus there is no adjustment required to convert the benefit into cash flow (GOETZE ET AL. 2015, p. 42). The SPP of the automated system is calculated as follows:

$$\mathbf{SPP} = \frac{\text{Capital allocation}}{\text{Average cash flow surpluses}} = \frac{C_S}{B_{S/E} + D_S} = \frac{30{,}000\,€}{98{,}700\,\frac{€}{a} + 6{,}000\,\frac{€}{a}} = \mathbf{0.29\,a}\,. \tag{6.5}$$

This results in an SPP of 0.29 years for the initial investment of €30,000 for the automated surface inspection system for a two-shift operation. The profitability of an investment is achieved if the payback period is shorter than the set target period of time (GOETZE ET AL. 2015, p. 42). Thus, it depends on the defined targeted period of the individual enterprise whether the calculated SPP of 0.29 years is considered profitable. Figure 6.1 illustrates the dependencies of Equations 6.1 to 6.5 as well as the break-even point at which the initial investment in the automated system is amortized.

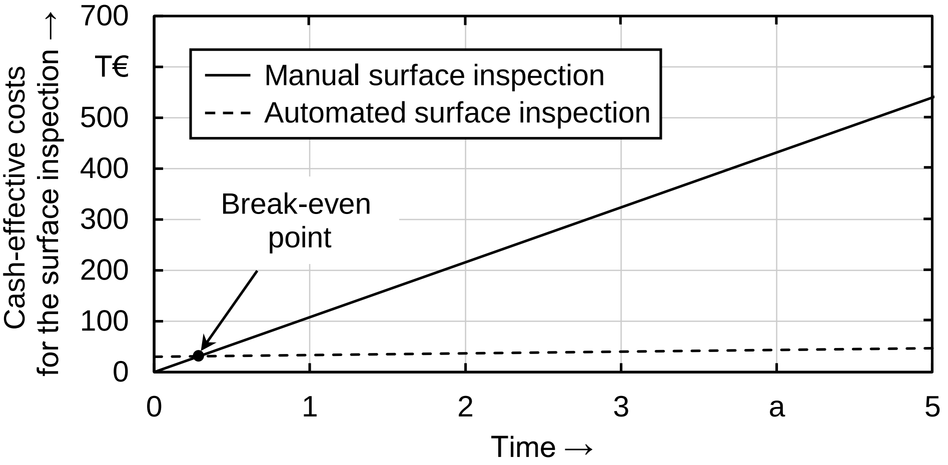

Figure 6.1: Cash-effective costs for the surface inspection performed manually and by using the automated system over the expected economic lifetime of the automated system

6.3 Advantages through automated process parameter determination

A further economic advantage results from the automated and more efficient determination of suitable process parameters (especially the welding speed and the tool rotational speed) for a given welding task. The results obtained in Stage 2 of this work are of particular interest for enterprises with frequently changing welding tasks, such as contract manufacturers, and for corporations with little experience in the field of FSW. To calculate how many different welding tasks per year are necessary so that the application of the developed BO algorithm for an automated process parameter determination is profitable, the following assumptions were made:

- The required time for one welding task $\mathbf{T_{WT}}$ is **0.25 hr**. According to the author’s experience in research operations, this is approximately the time required to unclamp the previous workpiece, clamp a new workpiece, and set the process parameters.
- The hourly labor costs $\mathbf{C_E}$ are **€27** as already assumed in Section 6.2.
- An unexperienced FSW system operator needs **nine steps** $\mathbf{St_E}$ to find suitable process parameters. This number corresponds to the number of steps the random search algorithms needed on average in publication P4 to find satisfactory settings for the welding speed and the tool rotational speed.

- If the BO approach, which is described in publication P4, is applied in the multi-task variant, the average number of steps required to find suitable process parameters $\mathbf{St_{BO}}$ is **five steps**.
- The costs $\mathbf{C_{WP}}$ for a workpiece that is used for testing one parameter set and thus gets destroyed if unsuitable process parameters are applied is **€100**.

The costs $C_{E/WT}$ for finding suitable parameters for one welding task without the algorithm-based system and purely by trial and error thus amount to

$$\mathbf{C_{E/WT}} = T_{WT} \cdot C_E \cdot St_E + C_{WP} \cdot St_E = 0.25\,\text{h} \cdot 27\,\frac{€}{\text{h}} \cdot 9 + 100€ \cdot 9 = \mathbf{€961}\,, \tag{6.6}$$

and the costs $C_{BO/WT}$ for finding good parameters when using the algorithm-based system are

$$\mathbf{C_{BO/WT}} = T_{WT} \cdot C_E \cdot St_{BO} + C_{WP} \cdot St_{BO} = 0.25\,\text{h} \cdot 27\,\frac{€}{\text{h}} \cdot 5 + 100€ \cdot 5 = \mathbf{€534}\,. \tag{6.7}$$

Thus, the monetary benefit per welding task $\mathbf{B_{WT}}$ when using the developed BO algorithms is

$$\mathbf{B_{WT}} = C_{E/WT} - C_{BO/WT} = €961 - €534 = \mathbf{€427}\,. \tag{6.8}$$

The annual costs of the automated surface inspection system $\mathbf{A_S}$, including the BO algorithm for determining the appropriate process parameters, are assumed to be **€9,300** per year, which is analogous to the performed calculation described in Section 6.2. Consequently, the number of necessary welding tasks per year N_{WT} for the algorithm-based process parameter determination to be profitable is

$$\mathbf{N_{WT}} = \frac{A_S}{B_{WT}} = \frac{9{,}300\,\frac{€}{\text{a}}}{427€} = \mathbf{21.8\,\frac{1}{a}}\,. \tag{6.9}$$

This means that the use of the developed system for the identification of suitable process parameters, under the assumptions, is profitable after 22 different welding tasks per year. Figure 6.2 shows the dependencies resulting from Equations 6.6 to 6.9 for the determination of suitable process parameters.

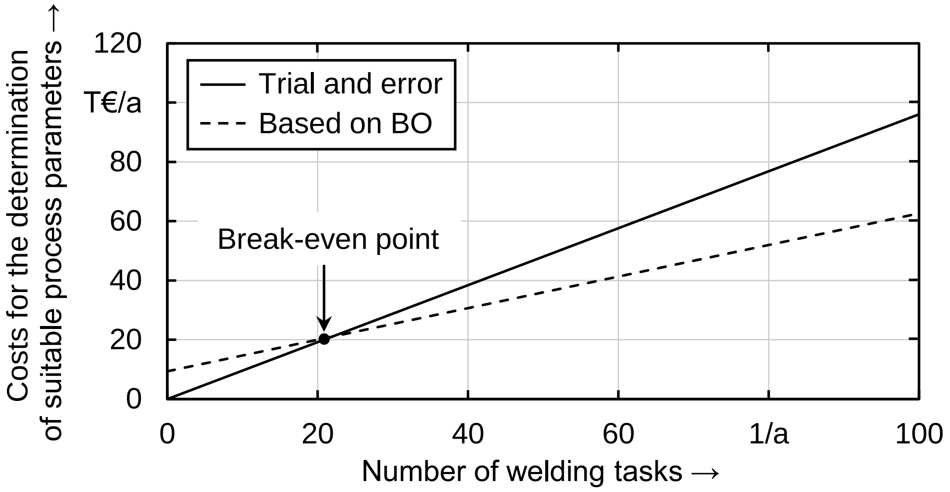

Figure 6.2: Annual costs for determining suitable process parameters depending on the number of welding tasks by trial and error and by BO

Additionally, in Figure 6.2, the break-even point is indicated, beyond which the use of the automated system containing the BO algorithm is amortized. To provide further economic advantages, a possibility was developed in Stage 2 not only to optimize the quality of the weld seam surface, but also to take the welding speed into account.

6.4 Advantages through non-destructive prediction of the tensile strength

The possibility of non-destructively estimating the tensile strength by GPR and of evaluating the surface topography is of particular relevance for industries with high-tech applications, such as aerospace, where the destruction of a component to perform a tensile test is expensive. Additionally, small and medium-sized enterprises, which often do not have the necessary equipment to execute material tests, can also take advantage. A corresponding algorithm was developed in Stage 3. The following assumptions are made to estimate the benefits of the data-based estimation of the tensile strength:

- Based on an enquiry to a manufacturer specialized in the production of materials testing machines, the price for a tensile testing machine $\mathbf{C_T}$ with a maximum tensile force of 50 kN is **€85,000**.
- Analogous assumptions as in Section 6.2 are employed for the level of the maintenance and service costs M_T (10 % of C_T per year), the expected economic lifetime that is given as 6 years for material testing facilities (GERMAN FEDERAL MINISTRY OF FINANCE 2001), and the imputed interest rate R, which is assumed to be 2 %. Thus, the maintenance and service costs for the tensile testing machine $\mathbf{M_T}$ are **€8,500** per year, the imputed depreciation $\mathbf{D_T}$ is **€14,167** per year, and the imputed interest $\mathbf{I_T}$ is **€850** per year according to the average method.

The annual costs of the tensile testing machine thus add up to

$$\mathbf{A_T} = M_T + D_T + I_T = 8{,}500\,\frac{€}{a} + 14{,}167\,\frac{€}{a} + 850\,\frac{€}{a} = \mathbf{23{,}517\,\frac{€}{a}}\ . \tag{6.10}$$

When accounting for the annual costs for the system $\mathbf{A_S}$ to monitor the surface topography and calculate the tensile strength as **€9,300** per year (cf. Section 6.2), this results in an annual monetary benefit $\mathbf{B_{S/T}}$ of

$$\mathbf{B_{S/T}} = A_T - A_S = 23{,}517\,\frac{€}{a} - 9{,}300\,\frac{€}{a} = \mathbf{14{,}217\,\frac{€}{a}} \tag{6.11}$$

by substituting the tensile testing machine through an algorithm-based prediction of the tensile strength. In addition, each tensile test that is substituted results in further savings. To calculate these, the following assumptions were necessary:

- The time $\mathbf{T_T}$ required to remove a test part from the workpiece, prepare a tensile specimen, and perform the tensile test is **1 hr**.
- The labor costs $\mathbf{C_E}$ for 1 hr in the industry are again assumed to be **€27** (cf. Section 6.2).
- The cost for one destroyed workpiece $\mathbf{C_{WP}}$ for the execution of the tensile test is **€100**.

Thus, the benefit for one substituted tensile test B_{TT} adds up to

$$\mathbf{B_{TT}} = T_T \cdot C_E + C_{WP} = 1\,\text{h} \cdot 27\,\frac{€}{\text{h}} + €100 = \mathbf{€127}\,. \tag{6.12}$$

This extra monetary benefit comes in addition to that from the replacement of the tensile testing machine for each individual material test replaced. Figure 6.3 shows the dependencies resulting from Equations 6.10 to 6.12 for the determination of the tensile strength. Since the data-based estimation by means of the GPR is from the beginning economically more favorable than the execution of tensile tests on a material testing machine, there is no break-even point. However, it should not be neglected that the non-destructive and data-based prediction based on the GPR is an estimation accompanied by uncertainty, whereas in tensile testing the actual value is determined.

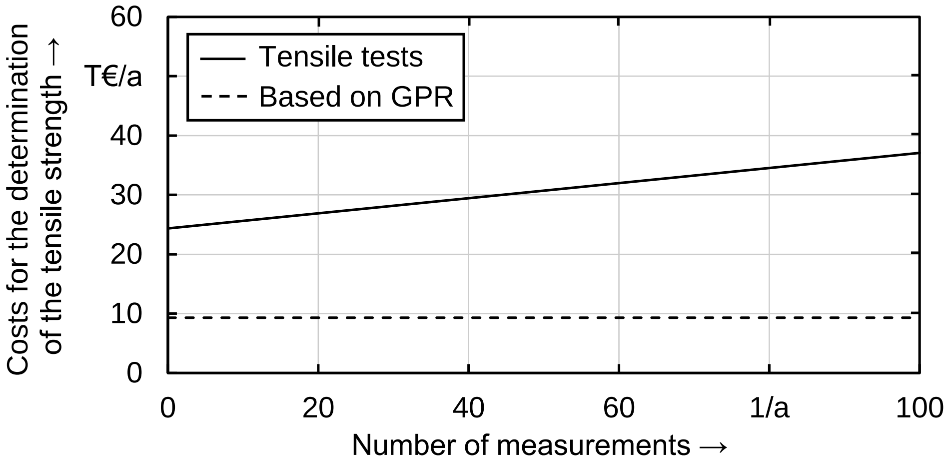

Figure 6.3: Annual costs for determining the tensile strength depending on the number of measurements by tensile tests and by the GPR

In summary, for each of the three main stages of this thesis it was shown that there are not only technological but also economic advantages. Different industries such as the automotive industry and aerospace can therefore benefit. Furthermore, large corporations as well as small and medium-sized enterprises can profit from the proposed approaches. However, it must be taken into account that the calculations explained in this chapter are only a direct cost calculation, since not all aspects were taken into account. To get a complete overview, further cost drivers must be considered before introducing an innovation in manufacturing. These include the re-training of employees, the creation of new operating instructions, or required post-audits of the innovation project, for instance (GOETZE ET AL. 2015, p. 16).

7 Concluding Remarks, Discussion, and Outlook

7.1 Concluding remarks

The objective of this thesis has been the automated monitoring and optimization of the surface quality of friction stir welds. By applying current knowledge from the field of ML, significant progress has been achieved compared to the state of the art. The focus has been on the weld surface for two reasons: the surface is an important quality feature of friction stir welds and the data acquisition via the analysis of the weld surface requires less effort than by mechanical-technological testing or metallography. The examinations were divided into three stages. In the first stage, an automated detection of surface features and defects was realized. In the second stage, an optimization of the surface topography was implemented. In the third stage, the correlations between the topography and the weld's mechanical properties were analyzed and the findings were applied to non-destructively predict the tensile strength of the welds. Since this dissertation is publication-based, the results of the corresponding investigations are only briefly summarized in Chapter 5. The bibliography of the publications is provided in Appendix A.1.

The most important findings from Stage 1 were the following:

- CNNs are well suited to detect friction stir welds on images and to classify a weld's surface properties.
- From the point cloud of the topography of friction stir welds, scalar key indicators can be derived, which allow the surface properties to be quantified. By defining threshold values for the key indicators, surface defects can be recognized.
- With the generating of spectrograms from the time series of the process variables recorded during FSW (e. g. process forces or temperatures), CNNs are also well suited to predict the weld surface quality based on process variables.

The most important findings from Stage 2 were the following:

- BO is well suited for optimizing the topography of friction stir welds.
- The optimization of the surface topography becomes even more efficient by incorporating information from other already conducted experimental studies.
- In addition to the surface quality, the welding speed can be considered at the same time, and it is possible to balance between the two requirements of a high surface quality and a high welding speed (trade-off).

The most important findings from Stage 3 were the following:

- For low welding speeds, there are pronounced correlations between the surface topography and the tensile strength of friction stir welds over a large interval of tool rotational speeds.
- By applying the GPR, these correlations can be utilized to predict the tensile strength of friction stir welds non-destructively on the basis of the weld topography. The uncertainty of the forecasts can also be quantified by providing a confidence interval. However, predictions based on the process variables and the process parameters lead to even better results.

7.2 Discussion and outlook

In this section, the scientific contribution of this cumulative dissertation is reflected on the basis of the three stages and in relation to the state of the art. Additionally, industrial applications of the knowledge gained are outlined, and an outlook on possible future research activities is provided.

The relation of the findings to the state of the art: Due to the direct mechanical contact of the FSW tool to the workpiece, friction stir welds have a quite characteristic surface. The automated evaluation and optimization of the weld surface therefore hold great potential for FSW. To ensure the full exploitation of this potential, methods of ML were applied in this work. In comparison to the state of the art, the following research progress (RP) has been made in the three stages:

RP1 The first attempt to automatically assess friction stir weld surface quality dates back to SINHA ET AL. (2008). With the use of a high number of image processing steps in sequence, efforts were made to extract features from weld surface images and to subsequently classify the surface by defining threshold values for these features. Besides the large manual effort to obtain the features, another problem was posed by the high processing times of several seconds to recognize the surface characteristics (RANJAN ET AL. 2016). Additionally, the state-of-the-art image processing algorithms used were not robust, as they depended strongly on environmental influences such as the illumination conditions. Regarding the evaluation of the surface topography and process variables to determine the surface quality of friction stir welds, there have been no studies to date. The methods proposed in this thesis for the evaluation of surface image information (cf. Subsection 5.2.1), topography data (cf. Subsection 5.2.2), and process variables (cf. Subsection 5.2.3) extend the previous approaches and allow a more reliable recognition of the surface quality of friction stir welds that requires less manual effort and is less prone to environmental conditions. Using the direct monitoring method with CNNs and topography images, a classification accuracy of 92.1 % was achieved (cf. Subsection 5.2.1). With the indirect monitoring method using CNNs and the spindle torque as a measurable, a classification accuracy of 87.4 % was reached (cf. Subsection 5.2.3; Case 2). These two results were each attained with a segment-based labeling of the welds and can therefore be compared. As described in Subsection 2.3.3, it is common that higher accuracies are achievable with direct monitoring methods, while indirect methods are less sensitive to environmental influences. The processing times of the three approaches presented in Stage 1 are in the millisecond range. This enables their application even at high welding speeds of more than 1000 mm/min that are required, for example, for electromobility parts to increase productivity (RICHTER 2017).

RP2 Up to 2010, approaches to optimize the quality of friction stir welds were based primarily on methods of statistical experimental design, such as the Taguchi method (TAGUCHI 1986). The goal was to discover how the independent variables influence the dependent variables by conducting the smallest possible number of experiments (LAKSHMINARAYANAN & BALASUBRAMANIAN 2008). Since 2010 algorithms from the field of ML have been applied, whereby usually ANNs were combined with evolutionary algorithms (TANSEL ET AL. 2010). In this dissertation, two algorithms that are able to effectively address the exploration-exploitation dilemma, which is also an important concept in human decision-making (COHEN ET AL. 2007), were utilized for the first time to determine suitable process parameters in FSW: RL (cf. Subsection 5.3.2) and BO (cf. Subsection 5.3.3). These algorithms make it possible to imitate the decisions of an experienced machine operator and thus to find suitable process parameters for a new welding task with high efficiency. Especially the BO algorithm was found to be suitable. With modeling the objective function through a GP (BROCHU ET AL. 2010), both the mean value and the variance of the weld quality prediction are taken into account by using BO.

RP3 In the literature, there were indications that there are relations between the surface properties of friction stir welds and friction stir welds' mechanical properties. An example was taken from SUDHAGAR ET AL. (2019): "The correlation between tensile strength and surface appearance reveals that weld joint[s] with irregular and defective surface[s] possess lower tensile strength." To the best of the author's knowledge, DAS ET AL. (2016) is the only work to date in which correlation coefficients between surface properties and mechanical properties have been determined. The surface properties were extracted from images of friction stir welds through manual effort using fractal theory or wavelet transform. The method for evaluating the surface topography presented in Stage 1 provided a way to quantify the surface characteristics with less effort. It was possible to reveal pronounced correlations between the topography and the tensile strength (cf. Subsection 5.4.1). The suitability of the GPR to predict the tensile strength by the evaluation of process parameters was already outlined by VERMA ET AL. (2018). Based on the findings described in Subsection 5.4.1, it was demonstrated for the first time that it is also possible to predict the tensile strength of friction stir welds by evaluating the surface topography by using GPR (cf. Subsection 5.4.2). However, by evaluating the process variables or the process parameters, the tensile strength could be predicted even more accurately than by evaluating the surface topography. Therefore, other monitoring systems, such as force or torque monitoring, should not be replaced by a topography monitoring. However, especially for safety-critical applications, such as aviation or electromobility, it might be interesting to monitor the weld's topography and supplement other systems to determine the tensile strength non-destructively.

Industrial applications of the findings: The results show that data sets with several million training samples are not always required to achieve good results when using CNNs. In addition to the quantity of the data, the quality of the data is also of great importance. For example, the human assignment of labels based on visual inspection often includes a certain degree of fuzziness. However, the results should encourage manufacturers to use machine-learning-based algorithms for FSW process monitoring and optimization. Three possible application fields (AFs) of the findings are given in the following:

AF1 The application of FSW is increasing in the automobile industry, and electromobility is particularly a driver for this trend (RICHTER 2017). Probably large quantities of friction stir welds will be produced in the next few decades in this sector (PARRATT & MARTIN 2019). Therefore, the results for the automated determination of the surface quality (cf. Section 5.2) are particularly interesting for the automotive industry. Which one of the three methods proposed in Stage 1 should be employed in an industrial environment cannot be stated in a general way and depends on the specific application. Also a combination of the presented approaches is conceivable.

AF2 The results of the algorithm-based optimization of the surface topography (cf. Section 5.3) can be useful for a more efficient identification of suitable process parameters for contract welding enterprises with frequently changing welding tasks and for manufacturers with little experience in the field of FSW. Additionally, manufacturers of FSW systems could integrate the developed optimization algorithms into their already existing CAM system for FSW. For example, the FSW system manufacturer Grenzebach Maschinenbau GmbH (Asbach-Baeumenheim, Germany) offers a CAM software that facilitates the creation of the welding program for FSW (GRENZEBACH MASCHINENBAU GMBH 2020). Among others, the software supports the programming of the welding path, the FSW process parameters, and the clamping elements. By integrating the BO-based method developed in Stage 2 for optimizing the process parameters, this software could be further improved.

AF3 The results for the non-destructive, data-based prediction of the tensile strength using the GPR could be of particular interest to manufacturers in high-tech industries with safety-critical applications, such as aerospace. Especially the specification of a confidence interval within which the tensile strength is located with a certain probability constitutes a benefit for this industry.

Outlook on future research activities: The results of the work presented in this thesis provide several possibilities for further investigations. Four promising potential research fields (PRFs) are described in the following:

PRF1 In the publications P1 to P3, weld seam defects were recognized that are mainly caused by unsuitable process parameters. For industrial applications, however, the detection of weld seam defects, which are due to geometric reasons, is also of interest. These include, for example, linear and angular misalignments of the sheets in butt-joints. These defects can probably also be detected using the approaches presented in Stage 1 (cf. Section 5.2).

Since CNNs have proven to be suitable for evaluating images of friction stir weld surfaces (cf. Subsection 5.2.1), this approach should be further pursued. Presumably, it will not only be feasible to recognize patterns in images of weld surfaces, but also images of the root side of butt-joints could be evaluated successfully. In this way, the detection of incomplete penetration welding could become possible.

Furthermore, it was discovered that the derivation of spectrograms from the process variables and the subsequent evaluation of the spectrograms by means of CNNs is suitable for determining friction stir weld characteristics. The approach for predicting the weld surface quality (cf. Subsection 5.2.3) can probably be transferred to other quality criteria as well. For example, JENE ET AL. (2008) demonstrated that the presence of cavities causes an alteration of the forces in x- and y- direction, which might be recognized using CNNs and could be the basis for a precise prediction of cavities.

PRF2 Another promising concept that should be pursued based on the findings of this work is the direct control of the friction stir weld surface. For this purpose, the ratio r_{arc} between the counted number and the theoretical number of local peaks and local valleys of the topography along the weld centerline (cf. Subsection 5.2.2) should be employed. With the aid of a light section sensor (cf. Subsection 2.3.3), which is placed inside the FSW machine as close as possible behind the rotating welding tool, the r_{arc} ratio could be determined inline. The mentioned ratio could be the target value of the control with a setpoint of 1. According to the findings of this work, the best surface quality is reached for an r_{arc} of 1 (cf. Subsection 5.2.2), and a maximum tensile strength is only achieved if this necessary condition is fulfilled (cf. Subsection 5.4.1). The recommended variable to be manipulated is the tool rotational speed. After the successful introduction of force control and temperature control in FSW, this could be the next step.

PRF3 For the prediction of mechanical properties, which are currently determined by destructive testing, the GPR has proven to be suitable, whereby the focus of the examinations in this work was on the prediction of the tensile strength by evaluating topography data. In future research, it should be attempted to predict further mechanical properties. Since a significant effect of surface defects on the fatigue behavior has already been reported in the literature (WIDENER ET AL. 2008), examining the prediction of the fatigue behavior by using ML-based methods would be particularly interesting.

PRF4 Finally, it is emphasized that the approaches presented in this dissertation are likely to be transferable to other welding technologies:

- The automated surface inspection methods for friction stir welds based on image information (cf. Subsection 5.2.1) or topography data (cf. Subsection 5.2.2) could be transferred to further welding techniques. The transfer to other material groups is also likely to be possible. In this thesis, only aluminum alloys were considered. However, an application of the approaches for joining copper or steel materials is also conceivable.
- Spectrograms can also be derived from the time series data recorded for other welding techniques. For example, voltage and current data in gas metal arc welding or optical coherence tomography data in laser beam welding might be evaluated applying CNNs to monitor the weld quality (cf. Subsection 5.2.3).
- The adjustment of process parameters using BO (cf. Subsection 5.3.3) to optimize the weld quality is probably also suitable for welding processes apart from FSW.

Finally, it can be concluded that through the work for this thesis, a decisive step has been taken towards a reliable and efficient monitoring and optimization of FSW processes using ML. The application of the presented approaches in other welding techniques is also highly promising.

References

ADELSON ET AL. 1984

Adelson, E. H.; Anderson, C. H.; Bergen, J. R.; Burt, P. J.; Ogden, J. M.: Pyramid methods in image processing. RCA Engineer vol. 29 (1984) 6, pp. 33 – 41.

ALFRED 1995

Alfred, U.: Einsatzmöglichkeiten von Neuronalen Netzen im Umweltbereich (Translated title: „Possible applications of neural networks in the environmental field“). In: Page, B. et al. (Eds.): Umweltinformatik (Translated title: „Environmental informatics“). Informatikmethoden für Umweltschutz und Umweltforschung (Translated subtitle: „Informatics methods for environmental protection and environmental research“). Munich, Germany: Oldenbourg 1995, pp. 219 – 244. ISBN: 3-486-23505-2.

ALKAYEM ET AL. 2016

Alkayem, N. F.; Parida, B.; Pal, S.: Optimization of friction stir welding process parameters using soft computing techniques. Soft Computing vol. 21 (2016) 23, pp. 7083 – 7098.

ARBEGAST 2007

Arbegast, W. J.: Chapter 13: Application of Friction Stir Welding and Related Technologies. In: Mahoney, M. W. et al. (Eds.): Friction stir welding and processing. Materials Park, OH, USA: ASM International 2007, pp. 273 – 308. ISBN: 978-0-87170-848-9.

ARORA ET AL. 2009

Arora, A.; Zhang, Z.; De, A.; DebRoy, T.: Strains and strain rates during friction stir welding. Scripta Materialia vol. 61 (2009) 9, pp. 863 – 866.

ARORA ET AL. 2011a

Arora, A.; DebRoy, T.; Bhadeshia, H. K. D. H.: Back-of-the-envelope calculations in friction stir welding – Velocities, peak temperature, torque, and hardness. Acta Materialia vol. 59 (2011) 5, pp. 2020 – 2028.

Wherever an issue number is not indicated, it does not exist or is unknown to the author of this thesis.

ARORA ET AL. 2011b

Arora, A.; De, A.; DebRoy, T.: Toward optimum friction stir welding tool shoulder diameter. Scripta Materialia vol. 64 (2011) 1, pp. 9 – 12.

ARORA ET AL. 2012

Arora, A.; Mehta, M.; De, A.; DebRoy, T.: Load bearing capacity of tool pin during friction stir welding. The International Journal of Advanced Manufacturing Technology vol. 61 (2012) 9 – 12, pp. 911 – 920.

BACHMANN ET AL. 2017

Bachmann, A.; Gamper, J.; Krutzlinger, M.; Zens, A.; Zaeh, M. F.: Adaptive model-based temperature control in friction stir welding. The International Journal of Advanced Manufacturing Technology vol. 93 (2017), pp. 1157 – 1171.

BACHMANN ET AL. 2018

Bachmann, A.; Krutzlinger, M.; Zaeh, M. F.: Influence of the welding temperature and the welding speed on the mechanical properties of friction stir welds in EN AW-2219-T87. IOP Conference Series: Materials Science and Engineering vol. 373 (2018), 012016.

BENKER 2018

Benker, M. (2018): Time Series Modelling with Gaussian Processes for Supply Chain Management. Unpublished manuscript. Master‘s Thesis. TECHNICAL UNIVERSITY OF BERLIN.

BHAT ET AL. 2015

Bhat, N. N.; Kumari, K.; Dutta, S.; Pal, S. K.; Pal, S.: Friction stir weld classification by applying wavelet analysis and support vector machine on weld surface images. Journal of Manufacturing Processes vol. 20 (2015), pp. 274 – 281.

BIKAR-METALLE GMBH 2017

Bikar-Metalle GmbH: Quality Certificate EN 10204 – 3.1. Bad Berleburg, Germany 2017.

BOLDSAIKHAN ET AL. 2006

Boldsaikhan, E.; Corwin, E.; Logar, A.; Arbegast, W.: Neural Network Evaluation of Weld Quality using FSW Feedback Data. In: TWI (Ed.): Proceedings of 6th International Symposium on Friction Stir Welding. Saint Sauveur, QC, Canada, October 10 – 13, 2006. Cambridge, UK: TWI 2006. ISBN: 1-903761-05-0.

BOLDSAIKHAN ET AL. 2011

Boldsaikhan, E.; Corwin, E. M.; Logar, A. M.; Arbegast, W. J.: The use of neural network and discrete Fourier transform for real-time evaluation of friction stir welding. Applied Soft Computing vol. 11 (2011), pp. 4839 – 4846.

BOURKE 2006

Bourke, P.: An introduction to the Apollonian fractal. Computers & Graphics vol. 30 (2006) 1, pp. 134 – 136.

BOX & WILSON 1981

Box, G. E. P.; Wilson, K. B.: On the Experimental Attainment of Optimum Conditions. Journal of the Royal Statistical Society vol. 13 (1981) 1, pp. 1 – 45.

BROCHU ET AL. 2010

Brochu, E.; Cora, V. M.; Freitas, N.: A Tutorial on Bayesian Optimization of Expensive Cost Functions, with Application to Active User Modeling and Hierarchical Reinforcement Learning. arXiv:1012.2599v1 (2010).

CANNY 1986

Canny, J.: A Computational Approach to Edge Detection. IEEE Transactions on Pattern Analysis and Machine Intelligence vol. 8 (1986) 6, pp. 679 – 698.

CHOLLET 2018

Chollet, F.: Deep learning with Python. Shelter Island, NY, USA: Manning Publications 2018. ISBN: 978-1-61729-443-3.

CIRESAN ET AL. 2013

Ciresan, D. C.; Giusti, A.; Gambardella, L. M.; Schmidhuber, J.: Deep Neural Networks Segment Neuronal Membranes in Electron Microscopy Images. In: Bartlett, P. L. et al. (Eds.): Advances in neural information processing systems, 26th Conference on Neural Information Processing Systems (NIPS). Lake Tahoe, NV, USA, December 3 – 8, 2012. Red Hook, NY, USA: Curran Associates 2013, pp. 2852 – 2860. ISBN: 978-1-62748-003-1.

COCHRAN & COX 1957

Cochran, W. G.; Cox, G. M.: Experimental designs. Hoboken, NJ, USA: John Wiley & Sons 1957. ISBN: 978-0471162049.

COELLO & LECHUGA 2002

Coello, C. A.; Lechuga, M. S.: MOPSO: a proposal for multiple-objective particle swarm optimization. In: Institute of Electrical and Electronics Engineers (Ed.): Proceedings of the Congress on Evolutionary Computation. Honolulu, HI, USA, May 12 – 17, 2002. Piscataway, NJ, USA: IEEE Press 2002, pp. 1051 – 1056. ISBN: 0-7803-7282-4.

COHEN ET AL. 2007

Cohen, J. D.; McClure, S. M.; Yu, A. J.: Should I stay or should I go? How the human brain manages the trade-off between exploitation and exploration. Philosophical transactions of the Royal Society: Biological sciences vol. 362 (2007) 1481, pp. 933 – 942.

COLEGROVE ET AL. 2007

Colegrove, P. A.; Shercliff, H. R.; Zettler, R.: Model for predicting heat generation and temperature in friction stir welding from the material properties. Science and Technology of Welding and Joining vol. 12 (2007) 4, pp. 284 – 297.

COLLIGAN 2010

Colligan, K. J.: The friction stir welding process: an overview. In: Lohwasser, D. et al. (Eds.): Friction stir welding. From basics to applications. Oxford, UK: CRC Press 2010, pp. 15 – 41. ISBN: 978-1-4398-0211-3.

CONIGLIO 2008

Coniglio, N.: Aluminium alloy weldability. Identification of weld solidification cracking mechanisms through novel experiment technique and model development. Dissertation. OTTO-VON-GUERICKE-UNIVERSITÄT MADGEBURG. Berlin, Germany: Federal Institute for Materials Research and Testing 2008. ISBN: 978-3-9812354-3-2.

CONVERSANO & TEDESCHINI-LALLI 2011

Conversano, E.; Tedeschini-Lalli, L.: Sierpinsky Triangles in Stone, on Medieval Floors in Rome. Journal of Applied Mathematics vol. 4 (2011) 4, pp. 113 – 122.

COSTANZI ET AL. 2017

Costanzi, G.; Bachmann, A.; Zaeh, M. F.: Entwicklung eines FSW-Spezialwerkzeugs zur Messung der Schweißtemperatur (Translated title: „Development of a special FSW tool for measuring the welding temperature“). In: Research Association on Welding and Allied Processes of the DVS (Ed.): DVS Congress. Duesseldorf, Germany, September 26 – 29, 2017. Duesseldorf, Germany: DVS Media 2017, pp. 119 – 125. ISBN: 978-3-96144-008-5.

COTTER ET AL. 2012

Cotter, A.; Shamir, O.; Srebro, N.; Sridharan, K.: Better Mini-Batch Algorithms via Accelerated Gradient Methods. In: Shawe-Taylor, J. et al. (Eds.): Advances in neural information processing systems, 25th Conference on Neural Information Processing Systems (NIPS). Granada, Spain, December 12 – 17, 2011. Red Hook, NY, USA: Curran Associates 2012, arXiv:1106.4574v1. ISBN: 978-1-61839-599-3.

DAS ET AL. 2016

Das, B.; Pal, S.; Bag, S.: Monitoring of friction stir welding process using weld image information. Science and Technology of Welding and Joining vol. 21 (2016) 4, pp. 317 – 324.

DEB 2001

Deb, K.: Multi-objective optimization using evolutionary algorithms. Chichester, UK: John Wiley & Sons 2001. ISBN: 0-471-87339-X.

DEB ET AL. 2002

Deb, K.; Pratap, A.; Agarwal, S.; Meyarivan, T.: A fast and elitist multiobjective genetic algorithm: NSGA-II. IEEE Transactions on Evolutionary Computation vol. 6 (2002) 2, pp. 182 – 197.

DEISENROTH 2010

Deisenroth, M. P.: Efficient reinforcement learning using Gaussian processes. Dissertation. KARLSRUHE INSTITUTE FOR TECHNOLOGY. Karlsruhe, Germany: KIT Scientific Publishing 2010. ISBN: 978-3-86644-569-7.

DENG ET AL. 2014

Deng, Y.; Zuo, D.; Song, B.: Analysis of the main factors affecting the surface morphology of FSJ joint. Advanced Materials Research vol. 1027 (2014), pp. 183 – 186.

DIN 50125

DIN 50125: Testing of metallic materials – Tensile test pieces. Berlin, Germany: Beuth 2016.

DIN EN 573-1

DIN EN 573-1: Aluminium and aluminium alloys – Chemical composition and form of wrought products – Part 1: Numerical designation system. Berlin, Germany: Beuth 2005.

DIN EN 515

DIN EN 515: Aluminium and aluminium alloys – Wrought products – Temper designations. Berlin, Germany: Beuth 2017.

DORNBERGER ET AL. 2018

Dornberger, R.; Inglese, T.; Korkut, S.; Zhong, V. J.: Digitalization: Yesterday, Today and Tomorrow. In: Dornberger, R. (Ed.): Business Information Systems and Technology 4.0. Cham, Switzerland: Springer International Publishing 2018, pp. 1 – 11. ISBN: 978-3-319-74321-9.

DU ET AL. 2019

Du, Y.; Mukherjee, T.; DebRoy, T.: Conditions for void formation in friction stir welding from machine learning. Nature Partner Journals: Computational Materials vol. 5 (2019) 68.

DUDA & HART 1972

Duda, R. O.; Hart, P. E.: Use of the Hough transformation to detect lines and curves in pictures. Communications of the ACM vol. 15 (1972) 1, pp. 11 – 15.

DUVENAUD ET AL. 2012

Duvenaud, D.; Nickisch, H.; Rasmussen, C. E.: Additive Gaussian Processes. In: Shawe-Taylor, J. et al. (Eds.): Advances in neural information processing systems, 25th Conference on Neural Information Processing Systems (NIPS). Granada, Spain, December 12 – 17, 2011. Red Hook, NY, USA: Curran Associates 2012, arXiv:1112.4394v1. ISBN: 978-1-61839-599-3.

DUVENAUD ET AL. 2013

Duvenaud, D.; Lloyd, J. R.; Grosse, R.; Tenenbaum, J. B.; Ghahramani, Z.: Structure Discovery in Nonparametric Regression through Compositional Kernel Search. In: Dasgupta, S. et al. (Eds.): Proceedings of Machine Learning Research, PMLR 28(3), International Conference on Machine Learning (ICML). Atlanta, GA, USA, June 17 – 19, 2013. Brookline, MA, USA: Microtome Publishing 2013, pp. 1166 – 1174, arXiv: 1302.4922v4.

ELATHARASAN & KUMAR 2013

Elatharasan, G.; Kumar, V. S.: An Experimental Analysis and Optimization of Process Parameter on Friction Stir Welding of AA 6061-T6 Aluminum Alloy using RSM. Procedia Engineering vol. 64 (2013), pp. 1227 – 1234.

FAHRMEIR ET AL. 2013

Fahrmeir, L.; Kneib, T.; Lang, S.; Marx, B.: Regression. Models, Methods and Applications. Berlin, Germany: Springer 2013. ISBN: 978-3-642-34333-9.

FARZADI ET AL. 2017

Farzadi, A.; Bahmani, M.; Haghshenas, D. F.: Optimization of Operational Parameters in Friction Stir Welding of AA7075-T6 Aluminum Alloy Using Response Surface Method. Arabian Journal for Science and Engineering vol. 42 (2017) 11, pp. 4905 – 4916.

FAYYAD ET AL. 1996

Fayyad, U.; Piatetsky-Shapiro, G.; Smyth, P.: The KDD process for extracting useful knowledge from volumes of data. Communications of the ACM vol. 39 (1996) 11, pp. 27 – 34.

FLEMING ET AL. 2009

Fleming, P. A.; Lammlein, D. H.; Wilkes, D. M.; Cook, G. E.; Strauss, A. M.; Delapp, D. R.; Hartman, D. A.: Misalignment detection and enabling of seam tracking for friction stir welding. Science and Technology of Welding and Joining vol. 14 (2009) 1, pp. 93 – 96.

FORSYTH 2019

Forsyth, D.: Applied Machine Learning. Cham, Switzerland: Springer International Publishing 2019. ISBN: 978-3-030-18113-0.

FULLER 2007

Fuller, C. B.: Chapter 2: Friction Stir Tooling: Tool Materials and Designs. In: Mahoney, M. W. et al. (Eds.): Friction stir welding and processing. Materials Park, OH, USA: ASM International 2007, pp. 7 – 35. ISBN: 978-0-87170-848-9.

GANAPATHY ET AL. 2017

Ganapathy, T.; Lenin, K.; Pannerselvam, K.: Process Parameters Optimization of Friction Stir Welding in Aluminium Alloy 6063-T6 by Taguchi Method. Applied Mechanics and Materials vol. 867 (2017), pp. 97 – 104.

GEBHARD 2011

Gebhard, P.: Dynamisches Verhalten von Werkzeugmaschinen bei Anwendung für das Rührreibschweißen (Translated title: „Dynamic behavior of machine tools when used for friction stir welding“). Dissertation. TECHNICAL UNIVERSITY OF MUNICH. Munich, Germany: utzverlag 2011. ISBN: 978-3-8316-4129-1.

GERMAN FEDERAL MINISTRY OF FINANCE 1995

German Federal Ministry of Finance: AfA-Tabelle für den Wirtschaftszweig Feinmechanische und Optische Industrie (Translated title: „Depreciation table for the precision mechanical and optical industry“) (1995). juris. Available online at <https://www.bundesfinanzministerium.de/Content/DE/Standardartikel/Themen/Steuern/Weitere_Steuerthemen/Betriebspruefung/AfA-Tabellen/AfA-Tabelle_Feinmechanische-und-Optische-Industrie.html> – visited on October 25, 2020.

GERMAN FEDERAL MINISTRY OF FINANCE 2001

German Federal Ministry of Finance: AfA-Tabelle für den Wirtschaftszweig Maschinenbau (Translated title: „Depreciation table for the mechanical engineering sector“) (2001). juris. Available online at <https://www.bundesfinanzministerium.de/Content/DE/Standardartikel/Themen/Steuern/Weitere_Steuerthemen/Betriebspruefung/AfA-Tabellen/AfA-Tabelle_Maschinenbau.html> – visited on February 20, 2020.

GÉRON 2017

Géron, A.: Hands-on machine learning with Scikit-Learn and TensorFlow. Concepts, tools, and techniques to build intelligent systems. Sebastopol, CA, USA: O‘Reilly Media 2017. ISBN: 978-1-491-96229-9.

GOETZE ET AL. 2015

Goetze, U.; Northcott, D.; Schuster, P.: Investment Appraisal. Methods and Models. Berlin, Germany: Springer 2015. ISBN: 978-3-662-45850-1.

GOODFELLOW ET AL. 2016

Goodfellow, I.; Bengio, Y.; Courville, A.: Deep learning. http://www.deeplearningbook.org/. Cambridge, MA, USA: MIT Press 2016. ISBN: 978-0-262-03561-3.

GRENZEBACH MASCHINENBAU GMBH 2020

Grenzebach Maschinenbau GmbH: FSW CAD/CAM Professional. Quickly to the finished welding program (2020). Available online at <https://www.grenzebach.com/products-markets/friction-stir-welding-technology/fsw-cadcam-professional/> – visited on July 19, 2020.

GROSSMANN & MORLET 1984

Grossmann, A.; Morlet, J.: Decomposition of Hardy Functions into Square Integrable Wavelets of Constant Shape. SIAM Journal on Mathematical Analysis vol. 15 (1984) 4, pp. 723 – 736.

GUENTHER 2018

Guenther, J. (2018): Machine intelligence for adaptable closed loop and open loop production engineering systems. Dissertation. TECHNICAL UNIVERSITY OF MUNICH.

HAMMER 2019

Hammer, M.: Management Approach for Resource-Productive Operations. Design of a Time-Based and Analytics-Supported Methodology Grounded in Six Sigma. Wiesbaden, Germany: Springer Gabler 2019. ISBN: 978-3-658-22938-2.

HARALICK ET AL. 1973

Haralick, R. M.; Shanmugam, K.; Dinstein, I.‘H.: Textural Features for Image Classification. IEEE Transactions on Systems, Man, and Cybernetics vol. SMC-3 (1973) 6, pp. 610 – 621.

HARTL ET AL. 2019a

Hartl, R.; Bachmann, A.; Liebl, S.; Zens, A.; Zaeh, M. F.: Automated surface inspection of friction stir welds by means of structured light projection. IOP Conference Series: Materials Science and Engineering vol. 480 (2019), 012035.

HARTL ET AL. 2019b

Hartl, R.; Landgraf, J.; Spahl, J.; Bachmann, A.; Zaeh, M. F.: Automated visual inspection of friction stir welds: a deep learning approach. In: Stella, E. et al. (Eds.): Proceedings of SPIE Vol. 11059, Multimodal Sensing: Technologies and Applications. Munich, Germany, June 24 – 27, 2019. Bellingham, WA, USA: SPIE 2019, 1105909. ISBN: 9781510627970.

HARTL ET AL. 2020a

Hartl, R.; Vieltorf, F.; Zaeh, M. F.: Correlations between the Surface Topography and Mechanical Properties of Friction Stir Welds. Metals vol. 10 (2020) 7, 890.

HARTL ET AL. 2020b

Hartl, R.; Hansjakob, J.; Zaeh, M. F.: Improving the surface quality of friction stir welds using reinforcement learning and Bayesian optimization. The International Journal of Advanced Manufacturing Technology vol. 110 (2020) 11 – 12, pp. 3145 – 3167.

HARTL ET AL. 2020c

Hartl, R.; Vieltorf, F.; Benker, M.; Zaeh, M. F.: Predicting the Ultimate Tensile Strength of Friction Stir Welds Using Gaussian Process Regression. Journal of Manufacturing and Materials Processing vol. 4 (2020) 3, 75.

HARTL ET AL. 2020d

Hartl, R.; Praehofer, B.; Zaeh, M. F.: Prediction of the surface quality of friction stir welds by the analysis of process data using Artificial Neural Networks. Proceedings of the Institution of Mechanical Engineers, Part L: Journal of Materials: Design and Applications vol. 234 (2020) 5, pp. 732 – 751.

HESSE 2016

Hesse, W.: Key to aluminum alloys. GERMAN INSTITUTE FOR STANDARDIZATION. Berlin, Germany: Beuth 2016. ISBN: 978-3-410-26873-4.

HEUMANN ET AL. 2016

Heumann, C.; Schomaker, M.; Shalabh: Introduction to Statistics and Data Analysis. Cham, Switzerland: Springer International Publishing 2016. ISBN: 978-3-319-46160-1.

HITOMI 1996

Hitomi, K.: Manufacturing Systems Engineering. A Unified Approach to Manufacturing Technology, Production Management and Industrial Economics. London, UK: CRC Press 1996. ISBN: 9780748403240.

HUANG ET AL. 2017

Huang, G.; Liu, Z.; van der Maaten, L.; Weinberger, K. Q.: Densely Connected Convolutional Networks. In: Chellappa, R. et al. (Eds.): Conference Proceedings, Conference on Computer Vision and Pattern Recognition (CVPR). Honolulu, HI, USA, June 21 – 26, 2017. Los Alamitos, CA, USA: IEEE Computer Society 2017, pp. 2261 – 2269, arXiv:1608.06993v5.

HUANG & KOVACEVIC 2011

Huang, W.; Kovacevic, R.: A laser-based vision system for weld quality inspection. Sensors vol. 11 (2011), pp. 506 – 521.

HUBER 2017

Huber, J.: Verfahren zur Klassifikation von Ungänzen bei der optischen Prüfung von Batterieseparatoren (Translated title: „Method for classifying imperfections in the optical inspection of battery separators“). Dissertation. TECHNICAL UNIVERSITY OF MUNICH. Munich, Germany: utzverlag 2017. ISBN: 978-3-8316-4593-0.

HUGGETT 2017

Huggett, D. J. (2017): Friction Stir Welding Manufacturing Advancement by On-Line High Temperature Phased Array Ultrasonic Testing and Correlation of Process Parameters to Joint Quality. Dissertation. LOUISIANA STATE UNIVERSITY AND AGRICULTURAL AND MECHANICAL COLLEGE.

IANDOLA ET AL. 2017

Iandola, F. N.; Han, S.; Moskewicz, M. W.; Ashraf, K.; Dally, W. J.; Keutzer, K.: SqueezeNet: AlexNet-Level Accuracy with 50x Fewer Parameters And <0.5MB Model Size. arXiv:1602.07360v4 (2017).

IEA 2019

IEA: Global EV Outlook 2019 (2019). Available online at <https://www.iea.org/reports/global-ev-outlook-2019> – visited on Oktober 7, 2020.

ISO 17639

ISO 17639: Destructive tests on welds in metallic materials – Macroscopic and microscopic examination of welds. Geneva, Switzerland: ISO 2003.

ISO 4136

ISO 4136: Destructive tests on welds in metallic materials – Transverse tensile test. Geneva, Switzerland: ISO 2012.

ISO 25178-2

ISO 25178-2: Geometrical product specifications (GPS) – Surface texture: Areal – Part 2: Terms, definitions and surface texture parameters. Geneva, Switzerland: ISO 2012.

ISO 6507-1

ISO 6507-1: Metallic materials – Vickers hardness test – Part 1: Test method. Geneva, Switzerland: ISO 2018.

ISO 6892-1

ISO 6892-1: Metallic materials – Tensile testing – Part 1: Method of test at room temperature. Geneva, Switzerland: ISO 2019.

ISO 25239-1

ISO 25239-1: Friction stir welding – Aluminium – Part 1: Vocabulary. Geneva, Switzerland: ISO 2020.

ISO 25239-4

ISO 25239-4: Friction stir welding – Aluminium – Part 4: Specification and qualification of welding procedures. Geneva, Switzerland: ISO 2020.

ISO 25239-5

ISO 25239-5: Friction stir welding – Aluminium – Part 5: Quality and inspection requirements. Geneva, Switzerland: ISO 2020.

JACQUENOT 2020

Jacquenot, G.: 2D Apollonian gasket with *n* identical circles (2020). Available online at <https://www.mathworks.com/matlabcentral/fileexchange/15987-2d-apollonian-gasket-with-n-identical-circles> – visited on March 11, 2020.

JENE ET AL. 2008

Jene, T.; Dobmann, G.; Wagner, G.; Eifler, D.: Monitoring of the Friction Stir Welding Process to Describe Parameter Effects on Joint Quality. Welding in the World vol. 52 (2008) 9 – 10, pp. 47 – 53.

KALLEE 2010

Kallee, S. W.: Industrial applications of friction stir welding. In: Lohwasser, D. et al. (Eds.): Friction stir welding. From basics to applications. Oxford, UK: CRC Press 2010, pp. 118 – 163. ISBN: 978-1-4398-0211-3.

KALPIĆ & HLUPIĆ 2011

Kalpić, D.; Hlupić, N.: Multivariate Normal Distributions. In: Lovric, M. (Ed.): International encyclopedia of statistical science. Berlin, Germany: Springer 2011, pp. 907 – 910. ISBN: 978-3-642-04916-3.

KATZ 1988

Katz, M. J.: Fractals and the analysis of waveforms. Computers in Biology and Medicine vol. 18 (1988) 3, pp. 145 – 156.

KAUFMAN 2000

Kaufman, J. G.: Introduction to aluminum alloys and tempers. Materials Park, OH, USA: ASM International 2000. ISBN: 978-0-87170-689-8.

KEFERSTEIN & MARXER 2015

Keferstein, C. P.; Marxer, M.: Fertigungsmesstechnik (Translated title: „Production measurement technology“). Wiesbaden, Germany: Springer Vieweg 2015. ISBN: 978-3-8348-2582-7.

KENNEDY & EBERHART 1995

Kennedy, J.; Eberhart, R. C.: Particle swarm optimization. In: Institute of Electrical and Electronics Engineers (Ed.): Proceedings of ICNN‘95, International Conference on Neural Networks. Perth, Australia, November 27 – December 1, 1995. Piscataway, NJ, USA: IEEE 1995, pp. 1942 – 1948. ISBN: 9780780327702.

KHANSARI ET AL. 2018

Khansari, N. M.; Berto, F.; Karimi, N.; Ghoreishi, S.M.N.; Fakoor, M.; Mokari, M.: Development of an optimal process for friction stir welding based on GA-RSM hybrid algorithm. Frattura ed Integrità Strutturale vol. 12 (2018) 44, pp. 106 – 122.

KIM ET AL. 2006

Kim, Y. G.; Fujii, H.; Tsumura, T.; Komazaki, T.; Nakata, K.: Three defect types in friction stir welding of aluminum die casting alloy. Materials Science and Engineering: A vol. 415 (2006) 1 – 2, pp. 250 – 254.

KOPAS ET AL. 2017

Kopas, P.; Saga, M.; Baniari, V.; Vasko, M.; Handrik, M.: A Plastic Strain and Stress Analysis of Bending and Torsion Fatigue Specimens in the Low-cycle Fatigue Region Using the Finite Element Methods. Procedia Engineering vol. 177 (2017), pp. 526 – 531.

KREUTZER & SIRRENBERG 2020

Kreutzer, R. T.; Sirrenberg, M.: Understanding Artificial Intelligence. Cham, Switzerland: Springer International Publishing 2020. ISBN: 978-3-030-25270-0.

KRIZHEVSKY ET AL. 2013

Krizhevsky, A.; Sutskever, I.; Hinton, G. E.: Imagenet classification with deep convolutional neural networks. In: Bartlett, P. L. et al. (Eds.): Advances in neural information processing systems, 26th Conference on Neural Information Processing Systems (NIPS). Lake Tahoe, NV, USA, December 3 – 8, 2012. Red Hook, NY, USA: Curran Associates 2013, pp. 1106 – 1114. ISBN: 978-1-62748-003-1.

KRUTZLINGER ET AL. 2015

Krutzlinger, M.; Bachmann, A.; Wirth, F. X.; Roth, A.; Sünger, S.; Pieczona, S. J.; Zaeh, M. F.: Implementierung einer Messsensorik in ein Fräsbearbeitungszentrum zur Ermittlung der Prozesskräfte und des Prozessmoments beim Rührreibschweißen (Translated title: „Implementation of a measuring system in a milling machining center to determine the process forces and the process torque during friction stir welding“). In: Research Association on Welding and Allied Processes of the DVS (Ed.): DVS Congress. Nuremberg, Germany, September 15 – 17, 2015. Duesseldorf, Germany: DVS Media 2015, pp. 209 – 214. ISBN: 978-3-945023-46-4.

KWOK ET AL. 2015

Kwok, J. T.; Zhou, Z.-H.; Xu, L.: Machine Learning. In: Kacprzyk, J. et al. (Eds.): Springer Handbook of Computational Intelligence. Berlin, Germany: Springer 2015, pp. 495 – 522. ISBN: 978-3-662-43504-5.

LABIDI 2010

Labidi, C.: Multivariate Normal Distribution. In: Salkind, N. J. (Ed.): Encyclopedia of research design. Thousand Oaks, CA, USA: Sage Publications 2010, pp. 862 – 868. ISBN: 978-1-4129-6127-1.

LAI ET AL. 1994

Lai, Y.-J.; Liu, T.-Y.; Hwang, C.-L.: TOPSIS for MODM. European Journal of Operational Research vol. 76 (1994) 3, pp. 486 – 500.

LAKSHMINARAYANAN & BALASUBRAMANIAN 2008

Lakshminarayanan, A. K.; Balasubramanian, V.: Process parameters optimization for friction stir welding of RDE-40 aluminium alloy using Taguchi technique. Transactions of Nonferrous Metals Society of China vol. 18 (2008) 3, pp. 548 – 554.

LEE ET AL. 2016

Lee, A.; Geem, Z.; Suh, K.-D.: Determination of Optimal Initial Weights of an Artificial Neural Network by Using the Harmony Search Algorithm: Application to Breakwater Armor Stones. Applied Sciences vol. 6 (2016) 6, 164.

LING 1990

Ling, F. F.: Fractals, engineering surfaces and tribology. Wear vol. 136 (1990) 1, pp. 141 – 156.

LIU ET AL. 2016

Liu, W.; Anguelov, D.; Erhan, D.; Szegedy, C.; Reed, S.; Fu, C.-Y.; Berg, A. C.: SSD: Single Shot MultiBox Detector. In: Leibe, B. et al. (Eds.): Computer Vision – ECCV, 14th European Conference. Amsterdam, Netherlands, Octotber 11 – 14, 2016. Cham, Switzerland: Springer International Publishing 2016, pp. 21 – 37. ISBN: 978-3-319-46447-3.

LOGAR ET AL. 2007

Logar, A. M.; Corwin, E. M.; Boldsaikhan, E.; Woodward, D.; Arbegast, W. J.: Applications of artificial intelligence to friction stir welding. In: Unknown editor (Ed.): National Conference on Recent Advancements in Information Technology, National Conference on Recent Advancements in Information Technology. Coimbatore, India, Feburary 9 – 10, 2007, unknown pages.

LOHWASSER & CHEN 2010

Lohwasser, D.; Chen, Z.: Introduction. In: Lohwasser, D. et al. (Eds.): Friction stir welding. From basics to applications. Oxford, UK: CRC Press 2010, pp. 1 – 12. ISBN: 978-1-4398-0211-3.

MA ET AL. 2019

Ma, Z.; Li, Q.; Ma, L.; Hu, W.; Xu, B.: Process Parameters Optimization of Friction Stir Welding of 6005A-T6 Aluminum Alloy Using Taguchi Technique. Transactions of the Indian Institute of Metals vol. 72 (2019) 7, pp. 1721 – 1731.

MAHONEY 2007

Mahoney, M. W.: Chapter 5: Mechanical Properties of Friction Stir Welded Aluminium Alloys. In: Mahoney, M. W. et al. (Eds.): Friction stir welding and processing. Materials Park, OH, USA: ASM International 2007, pp. 71 – 110. ISBN: 978-0-87170-848-9.

MAJEWSKI 2010

Majewski, A.: Cactus model of Mandelbrot set (2010). Available online at <https://commons.wikimedia.org/wiki/File:Cactus_model_of_Mandelbrot_set.svg> – visited on March 11, 2020.

MANDELBROT 1982

Mandelbrot, B. B.: The fractal geometry of nature. New York City, NY, USA: Freeman 1982. ISBN: 978-0716711865.

MARQUARDT 1963

Marquardt, D. W.: An Algorithm for Least-Squares Estimation of Nonlinear Parameters. Journal of the Society for Industrial and Applied Mathematics vol. 11 (1963) 2, pp. 431 – 441.

MARTIN ET AL. 2017

Martin, C.; Snabe, J. H.; Nanterme, P.: Digital Transformation Initiative. Unlocking $100 Trillion for Business and Society from Digital Transformation (2017). World Economic Forum. Available online at <https://www.accenture.com/_acnmedia/accenture/conversion-assets/wef/pdf/accenture-dti-executive-summary.pdf> – visited on January 5, 2020.

MARTÍNEZ-CAGIGAL 2020

Martínez-Cagigal, V.: Sierpinski Fractal Triangle (2020). MATLAB Central File Exchange. Available online at <https://www.mathworks.com/matlabcentral/fileexchange/50417-sierpinski-fractal-triangle> – visited on March 11, 2020.

MATAS ET AL. 2002

Matas, J.; Chum, O.; Urban, M.; Pajdla, T.: Robust Wide Baseline Stereo from Maximally Stable Extremal Regions. In: Rosin, P. L. et al. (Eds.): Electronic proceedings of the 13th British Machine Vision Conference. Cardiff, UK, September 2 – 5, 2002. Cardiff, UK: BMVA 2002, pp. 384 – 396. ISBN: 1-901725-19-7.

MATHUR 1991

Mathur, V. K.: How Well Do We Know Pareto Optimality? The Journal of Economic Education vol. 22 (1991) 2, pp. 172 – 178.

MEHTA ET AL. 2013

Mehta, M.; Chatterjee, K.; De, A.: Monitoring torque and traverse force in friction stir welding from input electrical signatures of driving motors. Science and Technology of Welding and Joining vol. 18 (2013) 3, pp. 191 – 197.

MERINO ET AL. 2017

Merino, J.; Patzelt, A.; Steinacher, A.; Windisch, M.; Heinrich, G.; Forster, R.; Bauer, C.: Ariane 6 – Tanks and Structures for the New European Launcher. Bonn, Germany: Deutsche Gesellschaft für Luft- und Raumfahrt – Lilienthal-Oberth e.V. 2017.

MESSLER 2004

Messler, R. W.: Principles of welding. Processes, physics, chemistry, and metallurgy. Weinheim, Germany: Wiley-VCH 2004. ISBN: 978-0-471-25376-1.

MISHRA ET AL. 2018

Mishra, D.; Roy, R. B.; Dutta, S.; Pal, S. K.; Chakravarty, D.: A review on sensor based monitoring and control of friction stir welding process and a roadmap to Industry 4.0. Journal of Manufacturing Processes vol. 36 (2018), pp. 373 – 397.

MISHRA & MAHONEY 2007

Mishra, R. S.; Mahoney, M. W.: Chapter 1: Introduction. In: Mahoney, M. W. et al. (Eds.): Friction stir welding and processing. Materials Park, OH, USA: ASM International 2007, pp. 1 – 5. ISBN: 978-0-87170-848-9.

MØLLER 1993

Møller, M. F.: A scaled conjugate gradient algorithm for fast supervised learning. Neural Networks vol. 6 (1993) 4, pp. 525 – 533.

MONTGOMERY 2017

Montgomery, D. C.: Design and analysis of experiments. Hoboken, NJ, USA: John Wiley & Sons 2017. ISBN: 978-1-119-11347-8.

MOREIRA ET AL. 2009

Moreira, P. M. G. P.; Santos, T.; Tavares, S. M. O.; Richter-Trummer, V.; Vilaça, P.; Castro, P. M. S. T.: Mechanical and metallurgical characterization of friction stir welding joints of AA6061-T6 with AA6082-T6. Materials & Design vol. 30 (2009), pp. 180 – 187.

MUGUTHU & GAO 2013

Muguthu, J. N.; Gao, D.: Profile Fractal Dimension and Dimensional Accuracy Analysis in Machining Metal Matrix Composites (MMCs). Materials and Manufacturing Processes vol. 28 (2013) 10, pp. 1102 – 1109.

MURPHY 2011

Murphy, K. P.: pmtk3/gprDemoChangeHparams.m at master · probml/pmtk3 · GitHub (2011). Available online at <https://github.com/probml/pmtk3/blob/master/demos/gprDemoChangeHparams.m> – visited on October 29, 2020.

MURPHY 2017

Murphy, K. P.: pmtk3/gprDemoNoiseFree.m at master · probml/pmtk3 · GitHub (2017). Available online at <https://github.com/probml/pmtk3/blob/master/demos/gprDemoNoiseFree.m> – visited on October 30, 2020.

MUSTAFA & ABDUL KADER 2018

Mustafa, W. A.; Abdul Kader, M. M.: A Review of Histogram Equalization Techniques in Image Enhancement Application. Journal of Physics Conference Series vol. 1019 (2018) 012026.

NANDAN ET AL. 2006

Nandan, R.; Roy, G. G.; DebRoy, T.: Numerical simulation of three-dimensional heat transfer and plastic flow during friction stir welding. Metallurgical and Materials Transactions A vol. 37 (2006) 4, pp. 1247 – 1259.

NANDAN ET AL. 2007

Nandan, R.; Roy, G. G.; Lienert, T. J.; DebRoy, T.: Three-dimensional heat and material flow during friction stir welding of mild steel. Acta Materialia vol. 55 (2007) 3, pp. 883 – 895.

NAYAK & MISHRA 2016

Nayak, S. R.; Mishra, J.: An improved method to estimate the fractal dimension of colour images. Perspectives in Science vol. 8 (2016), pp. 412 – 416.

NISHIHARA & NAGASAKA 2004

Nishihara, T.; Nagasaka, Y.: Measurement of Tool Temperature during Friction Stir Welding. In: TWI (Ed.): Proceedings of 4th International Symposium on Friction Stir Welding. Park City, UT, USA, May 14 – 16, 2003. Cambridge, UK: TWI 2004. ISBN: 1-903761-01-8.

NVIDIA CORPORATION 2020

NVIDIA Corporation: CUDA GPUs | NVIDIA Developer (2020). Available online at <https://developer.nvidia.com/cuda-gpus> – visited on August 10, 2020.

OKUYUCU ET AL. 2007

Okuyucu, H.; Kurt, A.; Arcaklioglu, E.: Artificial neural network application to the friction stir welding of aluminum plates. Materials & Design vol. 28 (2007) 1, pp. 78 – 84.

PALEN 2019

Palen, R.: Hourly labour costs ranged from €5.4 to €43.5 across the EU Member States in 2018. Labour costs in the EU. April 11, 2019 EUROSTAT PRESS OFFICE. Luxemburg.

PANZER ET AL. 2018

Panzer, F.; Werz, M.; Weihe, S.: Experimental investigation of the friction stir welding dynamics of 6000 series aluminum alloys. Production Engineering vol. 12 (2018) 5, pp. 667 – 677.

PARRATT & MARTIN 2019

Parratt, B.; Martin, J.: International Symposium on FSW: E-mobility causing a stir (2019). TWI. Available online at <https://www.twi-global.com/media-and-events/press-releases/2019/international-symposium-on-fsw-e-mobility-causing-a-stir> – visited on November 26, 2020.

PATHAK & JAISWAL 2014

Pathak, M.; Jaiswal, D.: Applications of Artificial Neural Networks in Friction Stir Welding: A Review. International Journal of Technological Exploration and Learning vol. 3 (2014) 3, pp. 513 – 517.

PIETRAS & WEGLOWSKI 2014

Pietras, A.; Weglowski, M. S.: Imperfections in FSW joints and NDT methods of their detection. Biuletyn Instytutu Spawalnictwa w Gliwicach vol. 58 (2014) 2, pp. 23 – 32.

QIAN ET AL. 2013

Qian, J.; Li, J.; Sun, F.; Xiong, J.; Zhang, F.; Lin, X.: An analytical model to optimize rotation speed and travel speed of friction stir welding for defect-free joints. Scripta Materialia vol. 68 (2013) 3 – 4, pp. 175 – 178.

QUINLAN 1986

Quinlan, J. R.: Induction of decision trees. Machine Learning vol. 1 (1986) 1, pp. 81 – 106.

RAJAKUMAR ET AL. 2010

Rajakumar, S.; Muralidharan, C.; Balasubramanian, V.: Optimization of the friction-stir-welding process and tool parameters to attain a maximum tensile strength of AA7075–T 6 aluminium alloy. Proceedings of the Institution of Mechanical Engineers, Part B: Journal of Engineering Manufacture vol. 224 (2010) 8, pp. 1175 – 1191.

RAJASHEKAR & RAJAPRAKASH 2013

Rajashekar, R.; Rajaprakash, B. M.: Digital Image Processing Of Friction Stir Weld Bead Surface Using Profiling and Contouring For Weld Quality Assessment. Journal of Mechanical and Civil Engineering vol. 5 (2013) 5, pp. 54 – 64.

RAJASHEKAR & RAJAPRAKASH 2016

Rajashekar, R.; Rajaprakash, B. M.: Development of a model for friction stir weld quality assessment using machine vision and acoustic emission techniques. Journal of Materials Processing Technology vol. 229 (2016), pp. 265 – 274.

RANJAN ET AL. 2016

Ranjan, R.; Khan, A. R.; Parikh, C.; Jain, R.; Mahto, R. P.; Pal, S.; Pal, S. K.; Chakravarty, D.: Classification and identification of surface defects in friction stir welding: An image processing approach. Journal of Manufacturing Processes vol. 22 (2016), pp. 237 – 253.

RAO 2011

Rao, R. V.: Advanced Modeling and Optimization of Manufacturing Processes. London, UK: Springer 2011. ISBN: 978-0-85729-014-4.

RAO & SWAMY 2018

Rao, K. D.; Swamy, M.N.S.: Digital Signal Processing. Singapore: Springer 2018. ISBN: 978-981-10-8080-7.

RASMUSSEN & WILLIAMS 2006

Rasmussen, C. E.; Williams, C. K.: Gaussian processes for machine learning. Cambridge, MA, USA: MIT Press 2006. ISBN: 978-0-262-18253-9.

RECORD ET AL. 2004

Record, J. H.; Convintion, J. L.; Nelson, T. W.; Sorensen, C. D.; Webb, B. W.: Fundamental Characterization of Friction Stir Welding. In: TWI (Ed.): Proceedings of 5th International Symposium on Friction Stir Welding. Metz, France, September 14 – 16, 2004. Cambridge, UK: TWI 2004. ISBN: 1-903761-04-2.

REDMON ET AL. 2016

Redmon, J.; Divvala, S.; Girshick, R.; Farhadi, A.: You Only Look Once: Unified, Real-Time Object Detection. In: Bajscy, R. et al. (Eds.): Proceedings of the Conference on Computer Vision and Pattern Recognition (CVPR). Las Vegas, NV, USA, June 27 – 30, 2016. Los Alamitos, CA, USA: IEEE Computer Society 2016. ISBN: 978-1-4673-8851-1.

RELF 2004

Relf, C. G.: Image acquisition and processing with LabVIEW. Boca Raton, FL, USA: CRC Press 2004. ISBN: 0-8493-1480-1.

REN ET AL. 2017a

Ren, J.; Chen, X.; Liu, J.; Sun, W.; Pang, J.; Yan, Q.; Tai, Y.-W.; Xu, L.: Accurate Single Stage Detector Using Recurrent Rolling Convolution. In: Chellappa, R. et al. (Eds.): Conference Proceedings, Conference on Computer Vision and Pattern Recognition (CVPR). Honolulu, HI, USA, June 21 – 26, 2017. Los Alamitos, CA, USA: IEEE Computer Society 2017, pp. 752 – 760.

REN ET AL. 2017b

Ren, S.; He, K.; Girshick, R.; Sun, J.: Faster R-CNN: Towards Real-Time Object Detection with Region Proposal Networks. IEEE Transactions on Pattern Analysis and Machine Intelligence vol. 39 (2017) 6, pp. 1137 – 1149.

REYNOLDS 2007

Reynolds, A. P.: Chapter 4: Microstructure Development in Aluminum Alloy Friction Stir Welds. In: Mahoney, M. W. et al. (Eds.): Friction stir welding and processing. Materials Park, OH, USA: ASM International 2007, pp. 51 – 70. ISBN: 978-0-87170-848-9.

RICHTER 2017

Richter, B.: Robot-based Friction Stir Welding for E-mobility and General Applications. Biuletyn Instytutu Spawalnictwa vol. 61 (2017) 5, pp. 103 – 110.

ROCHESTER ET AL. 1956

Rochester, N.; Holland, J.; Haibt, L.; Duda, W.: Tests on a cell assembly theory of the action of the brain, using a large digital computer. IEEE Transactions on Information Theory vol. 2 (1956) 3, pp. 80 – 93.

ROEHRICH 2014

Roehrich, M.: Fundamentals of Investment Appraisal. An Illustration based on a Case Study. Berlin, Germany: de Gruyter 2014. ISBN: 978-3-11-034718-0.

ROSENBLATT 1958

Rosenblatt, F.: The perceptron: A probabilistic model for information storage and organization in the brain. Psychological Review vol. 65 (1958) 6, pp. 386 – 408.

ROTH 2016

Roth, A.: Modellierung des Rührreibschweißens unter besonderer Berücksichtigung der Spalttoleranz (Translated title: „Modelling of friction stir welding with special consideration of the gap tolerance“). Dissertation. TECHNICAL UNIVERSITY OF MUNICH. Munich, Germany: utzverlag 2016. ISBN: 978-3-8316-4639-5.

RUHSTORFER 2012

Ruhstorfer, M.: Rührreibschweißen von Rohren (Translated title: „Friction stir welding of pipes“). Dissertation. TECHNICAL UNIVERSITY OF MUNICH. Munich, Germany: utzverlag 2012. ISBN: 978-3-8316-4197-0.

RUMELHART ET AL. 1986

Rumelhart, D. E.; Hinton, G. E.; Williams, R. J.: Learning representations by back-propagating errors. Nature vol. 323 (1986) 6088, pp. 533 – 536.

RUSSELL ET AL. 1980

Russell, D. A.; Hanson, J. D.; Ott, E.: Dimension of Strange Attractors. Physical Review Letters vol. 45 (1980) 14, pp. 1175 – 1178.

RUSSELL & NORVIG 2016

Russell, S. J.; Norvig, P.: Artificial intelligence. A modern approach. Hoboken, NJ, USA: Pearson Education 2016. ISBN: 978-0-13-604259-4.

SCHMIDT & HATTEL 2005

Schmidt, H.; Hattel, J.: Modelling heat flow around tool probe in friction stir welding. Science and Technology of Welding and Joining vol. 10 (2005) 2, pp. 176 – 186.

SCHNEIDER 2007

Schneider, J. A.: Chapter 3: Temperature Distribution and Resulting Metal Flow. In: Mahoney, M. W. et al. (Eds.): Friction stir welding and processing. Materials Park, OH, USA: ASM International 2007, pp. 37 – 49. ISBN: 978-0-87170-848-9.

SCHOELKOPF & SMOLA 2002

Schoelkopf, B.; Smola, A. J.: Learning with kernels. Support vector machines, regularization, optimization, and beyond. Cambridge, MA, USA: MIT Press 2002. ISBN: 978-0-262-19475-4.

SHERCLIFF & COLEGROVE 2007

Shercliff, H. R.; Colegrove, P. A.: Chapter 10: Process Modeling. In: Mahoney, M. W. et al. (Eds.): Friction stir welding and processing. Materials Park, OH, USA: ASM International 2007, pp. 187 – 217. ISBN: 978-0-87170-848-9.

SHOJAEEFARD ET AL. 2013

Shojaeefard, M. H.; Behnagh, R. A.; Akbari, M.; Givi, M. K.; Farhani, F.: Modelling and Pareto optimization of mechanical properties of friction stir welded AA7075/AA5083 butt joints using neural network and particle swarm algorithm. Materials & Design vol. 44 (2013), pp. 190 – 198.

SHOJAEEFARD ET AL. 2014

Shojaeefard, M. H.; Akbari, M.; Asadi, P.: Multi objective optimization of friction stir welding parameters using FEM and neural network. International Journal of Precision Engineering and Manufacturing vol. 15 (2014) 11, pp. 2351 – 2356.

SICILAN & KUMAR 2014

Sicilan, M. A.; Kumar, S. S.: Analysis of Surface Quality of Friction Stir Welding Joints using Image Processing Techniques,. In: Sainulabdeen Poonthottam, A. et al. (Eds.): Proceedings of the International Conference on Emerging Trends in Engineering & Technology. Kollam, India, March 31 – April 1, 2014: Travancore Engineering College 2014, pp. 1 – 4.

SIDHU & CHATHA 2012

Sidhu, M. S.; Chatha, S. S.: Friction Stir Welding – Process and its Variables: A Review. International Journal of Emerging Technology and Advanced Engineering vol. 2 (2012) 12, pp. 275 – 279.

SIMONYAN & ZISSERMAN 2015

Simonyan, K.; Zisserman, A.: Very Deep Convolutional Networks for Large-Scale Image Recognition. In: Bengio, Y. et al. (Eds.): Conference Track Proceedings, 3rd International Conference on Learning Representations. San Diego, CA, USA, May 7 – 9, 2015. La Jolla, CA, USA: ICLR 2015, arXiv:1409.1556v6.

SINHA ET AL. 2008

Sinha, P.; Muthukumaran, S.; Sivakumar, R.; Mukherjee, S. K.: Condition monitoring of first mode of metal transfer in friction stir welding by image processing techniques. The International Journal of Advanced Manufacturing Technology vol. 36 (2008), pp. 484 – 489.

SIVANANDAM & DEEPA 2008

Sivanandam, S. N.; Deepa, S. N.: Introduction to Genetic Algorithms. Berlin, Germany: Springer 2008. ISBN: 978-3-540-73189-4.

SMITH 2007

Smith, C. B.: Chapter 11: Robots and Machines for Friction Stir Welding/Processing. In: Mahoney, M. W. et al. (Eds.): Friction stir welding and processing. Materials Park, OH, USA: ASM International 2007, pp. 219 – 233. ISBN: 978-0-87170-848-9.

SMITH & HINRICHS 2011

Smith, C. B.; Hinrichs, J. F.: Friction Stir Welding and Related Processes. In: Schwartz, M. M. (Ed.): Innovations in materials manufacturing, fabrication, and environmental safety. Boca Raton, FL, USA: CRC Press 2011, pp. 241 – 303. ISBN: 978-1-4200-8215-9.

STEINMETZ & NAHRSTEDT 2002

Steinmetz, R.; Nahrstedt, K.: Multimedia fundamentals. Upper Saddle River, NJ, USA: Prentice Hall PTR 2002. ISBN: 0-13-031399-8.

STOPKA & URBAN 2017

Stopka, U.; Urban, T.: Investition und Finanzierung (Translated title: „Investment and financing“). Berlin, Germany: Springer 2017. ISBN: 978-3-642-01691-2.

STORN & PRICE 1997

Storn, R.; Price, K.: Differential Evolution – A Simple and Efficient Heuristic for global Optimization over Continuous Spaces. Journal of Global Optimization vol. 11 (1997) 4, pp. 341 – 359.

SUDHAGAR ET AL. 2019

Sudhagar, S.; Sakthivel, M.; Ganeshkumar, P.: Monitoring of friction stir welding based on vision system coupled with Machine learning algorithm. Measurement vol. 144 (2019), pp. 135 – 143.

SUENGER ET AL. 2014

Suenger, S.; Kreissle, M.; Kahnert, M.; Zaeh, M. F.: Influence of Process Temperature on Hardness of Friction Stir Welded High Strength Aluminum Alloys for Aerospace Applications. Procedia CIRP vol. 24 (2014), pp. 120 – 124.

SUTTON & BARTO 2018

Sutton, R. S.; Barto, A.: Reinforcement learning. An introduction. Cambridge, MA, USA: MIT Press 2018. ISBN: 978-0-262-03924-6.

TAGUCHI 1986

Taguchi, G.: Introduction to quality engineering. Designing quality into products and processes. Tokyo, Japan: Asian Productivity Organization 1986. ISBN: 92-833-1084-5.

TAHERI ET AL. 2019

Taheri, H.; Kilpatrick, M.; Norvalls, M.; Harper, W. J.; Koester, L. W.; Bigelow, T.; Bond, L. J.: Investigation of Nondestructive Testing Methods for Friction Stir Welding. Metals vol. 9 (2019) 6, 624.

TANER & BOESCH 2018

Taner, S.; Boesch, L.: Audi optimizes quality inspections in the press shop with artificial intelligence. October 15, 2018 AUDI MEDIAINFO. Ingolstadt, Germany.

TANSEL ET AL. 2010

Tansel, I. N.; Demetgul, M.; Okuyucu, H.; Yapici, A.: Optimizations of friction stir welding of aluminum alloy by using genetically optimized neural network. The International Journal of Advanced Manufacturing Technology vol. 48 (2010), pp. 95 – 101.

THREADGILL ET AL. 2009

Threadgill, P. L.; Leonard, A. J.; Shercliff, H. R.; Withers, P. J.: Friction stir welding of aluminium alloys. International Materials Reviews vol. 54 (2009) 2, pp. 49 – 93.

TINO ET AL. 2015

Tino, P.; Benuskova, L.; Sperduti, A.: Artificial Neural Network Models. In: Kacprzyk, J. et al. (Eds.): Springer Handbook of Computational Intelligence. Berlin, Germany: Springer 2015, pp. 455 – 471. ISBN: 978-3-662-43504-5.

TURING 1950

Turing, A. M.: Computing machinery and intelligence. Mind vol. 59 (1950) 236, pp. 433 – 460.

UESTUEN ET AL. 2006

Uestuen, B.; Melssen, W. J.; Buydens, L. M.: Facilitating the application of Support Vector Regression by using a universal Pearson VII function based kernel. Chemometrics and Intelligent Laboratory Systems vol. 81 (2006), pp. 29 – 40.

UGENDER ET AL. 2015

Ugender, S.; Kumar, A.; Somi Reddy, A.: Effect of Friction Stir Welding Process Parameters on the Mechanical Properties of AA 6061 Aluminum Alloy Using Taguchi Orthogonal Technique. Applied Mechanics and Materials vol. 813 – 814 (2015), pp. 431 – 437.

UNAL & DEAN 1991

Unal, R.; Dean, E. B.: Taguchi Approach to Design Optimization for Quality and Cost: An Overview. In: International Society of Parametric Analysts (Ed.): Proceedings of the 13th Annual Conference of the International Society of Parametric Analysts. New Orleans, LA, USA, May 21 – 24, 1991. Vienna, VA, USA: International Society of Parametric Analysts 1991, pp. 1 – 10.

VALAVANIS & KOSMOPOULOS 2010

Valavanis, I.; Kosmopoulos, D.: Multiclass defect detection and classification in weld radiographic images using geometric and texture features. Expert Systems with Applications vol. 37 (2010) 12, pp. 7606 – 7614.

VANDER VOORT 2004

Vander Voort, G. F.: Metallography and Microstructures. Metals Park, OH, USA: American Society for Metals 2004. ISBN: 0-87170-706-3.

VAPNIK 2010

Vapnik, V.: The Nature of Statistical Learning Theory. New York City, NY, USA: Springer 2010. ISBN: 978-1-4419-3160-3.

VERMA ET AL. 2018

Verma, S.; Gupta, M.; Misra, J. P.: Performance evaluation of friction stir welding using machine learning approaches. MethodsX vol. 5 (2018), pp. 1048 – 1058.

VINCENT 1993

Vincent, L.: Morphological grayscale reconstruction in image analysis: applications and efficient algorithms. IEEE Transactions on Image Processing vol. 2 (1993) 2, pp. 176 – 201.

VOELLNER 2010

Voellner, G.: Rührreibschweißen mit Schwerlast-Industrierobotern (Translated title: „Friction stir welding with heavy-duty industrial robots“). Dissertation. TECHNICAL UNIVERSITY OF MUNICH. Munich, Germany: utzverlag 2010. ISBN: 978-3-8316-0955-0.

WAHED & TANG 2010

Wahed, A. S.; Tang, X.: Analysis of Variance (ANOVA). In: Salkind, N. J. (Ed.): Encyclopedia of research design. Thousand Oaks, CA, USA: Sage Publications 2010, pp. 26 – 29. ISBN: 978-1-4129-6127-1.

WANG & CHEN 2017

Wang, S.; Chen, S.: A Novel Bayesian Optimization Framework for Computationally Expensive Optimization Problem in Tight Oil Reservoirs. In: Society of Petroleum Engineers (Ed.): Annual Technical Conference and Exhibition (ATCE). San Antonio, TX, USA, Oktober 9 – 11, 2017. Richardson, TX, USA: SPE 2017, SPE-187284-MS. ISBN: 978-1-5108-5164-1.

WIDENER ET AL. 2008

Widener, C. A.; Tweedy, B. M.; Burford, D. A.: An Investigation of the Effects of Tool Design and Welding Parameters on Fatigue Life in Friction Stir Welded 2024-T3. In: TWI (Ed.): Proceedings of 7th International Symposium on Friction Stir Welding. Awaji, Japan, May 20 – 22, 2008. Cambridge, UK: TWI 2008. ISBN: 978-1-903761-06-9.

WIERING & VAN OTTERLO 2012. Wiering, M.; van Otterlo, M.: Reinforcement Learning. State-of-the-Art. Berlin, Germany: Springer 2012. ISBN: 978-3-642-27644-6.

WILKINSON 2019

Wilkinson, R.: An introduction to Gaussian Processes (2019). School of Math and Statistics, University of Sheffield (GP summer school). Available online at <http://gpss.cc/gpss19/slides/Wilkinson2019.pdf> – visited on Oktober 8, 2020.

WILLENBACHER ET AL. 2018

Willenbacher, M.; Kunisch, C.; Wohlgemuth, V.: Application of Methods of Artificial Intelligence for Sustainable Production of Manufacturing Companies. In: Otjacques, B. et al. (Eds.): From Science to Society. Cham, Switzerland: Springer International Publishing 2018, pp. 225 – 236. ISBN: 978-3-319-65686-1.

WILLIAMS & STEUWER 2010

Williams, S. W.; Steuwer, A.: Residual stresses in friction stir welding. In: Lohwasser, D. et al. (Eds.): Friction stir welding. From basics to applications. Oxford, UK: CRC Press 2010, pp. 215 – 244. ISBN: 978-1-4398-0211-3.

WILSON & ADAMS 2013

Wilson, A. G.; Adams, R. P.: Gaussian Process Kernels for Pattern Discovery and Extrapolation. In: Dasgupta, S. et al. (Eds.): Proceedings of Machine Learning Research, PMLR 28(3), International Conference on Machine Learning (ICML). Atlanta, GA, USA, June 17 – 19, 2013. Brookline, MA, USA: Microtome Publishing 2013, pp. 1067 – 1075.

WOLF & STROHSCHEN 2018

Wolf, T.; Strohschen, J.-H.: Digitalisierung: Definition und Reife (Translated title: „Digitalization: definition and readiness“). Informatik Spektrum vol. 41 (2018) 1, pp. 56 – 64.

WUEST ET AL. 2016

Wuest, T.; Weimer, D.; Irgens, C.; Thoben, K.-D.: Machine learning in manufacturing: advantages, challenges, and applications. Production & Manufacturing Research vol. 4 (2016) 1, pp. 23 – 45.

XU & DENG 2008

Xu, S.; Deng, X.: A study of texture patterns in friction stir welds. Acta Materialia vol. 56 (2008) 6, pp. 1326 – 1341.

YOUSIF ET AL. 2008

Yousif, Y. K.; Daws, K. M.; Kazem, B. I.: Prediction of Friction Stir Welding Characteristic Using Neural Network. Jordan Journal of Mechanical and Industrial Engineering vol. 2 (2008) 3, pp. 151 – 155.

YU & GEN 2010

Yu, X.; Gen, M.: Introduction to Evolutionary Algorithms. London, UK: Springer 2010. ISBN: 978-1-84996-128-8.

YUNUS & ALSOUFI 2018

Yunus, M.; Alsoufi, M. S.: Mathematical Modelling of a Friction Stir Welding Process to Predict the Joint Strength of Two Dissimilar Aluminium Alloys Using Experimental Data and Genetic Programming. Modelling and Simulation in Engineering vol. 4 (2018), 4183816.

ZAEH & GEBHARD 2009

Zaeh, M. F.; Gebhard, P.: Übertragbarkeit von Schweißparametern beim Rührreibschweißen (Translated title: „Transferability of welding parameters in friction stir welding“). In: Research Association on Welding and Allied Processes of the DVS (Ed.): DVS Congress. Essen, Germany, September 14 – 19, 2009. Duesseldorf, Germany: DVS Media 2009, pp. 60 – 65. ISBN: 978-3-87155-584-8.

ZAPPIA 2010a

Zappia, T.: Friction stir welding equipment. In: Lohwasser, D. et al. (Eds.): Friction stir welding. From basics to applications. Oxford, UK: CRC Press 2010, pp. 73 – 117. ISBN: 978-1-4398-0211-3.

ZAPPIA 2010b

Zappia, T.: Inspection and quality control in friction stir welding. In: Lohwasser, D. et al. (Eds.): Friction stir welding. From basics to applications. Oxford, UK: CRC Press 2010, pp. 183 – 212. ISBN: 978-1-4398-0211-3.

ZELTERMAN 2015

Zelterman, D.: Applied Multivariate Statistics with R. Cham, Switzerland: Springer International Publishing 2015. ISBN: 978-3-319-14092-6.

ZETTLER ET AL. 2010

Zettler, R.; Vugrin, T.; Schmuecker, M.: Effects and defects in friction stir welding. In: Lohwasser, D. et al. (Eds.): Friction stir welding. From basics to applications. Oxford, UK: CRC Press 2010, pp. 245 – 276. ISBN: 978-1-4398-0211-3.

ZETTLER 2010

Zettler, R.: Material deformation and joint formation in friction stir welding. In: Lohwasser, D. et al. (Eds.): Friction stir welding. From basics to applications. Oxford, UK: CRC Press 2010, pp. 42 – 72. ISBN: 978-1-4398-0211-3.

ZHANG 2004

Zhang, H.: The Optimality of Naive Bayes. In: Barr, V. et al. (Eds.): Proceedings of the 17th International Florida Artificial Intelligence Research Society Conference. Miami Beach, FL, USA, May 17 – 19, 2004. Menlo Park, CA, USA: AAAI Press 2004, pp. 562 – 567. ISBN: 978-1-57735-201-3.

ZUO ET AL. 2018

Zuo, L.; Zuo, D.; Zhu, Y.; Wang, H.: Effect of process parameters on surface topography of friction stir welding. The International Journal of Advanced Manufacturing Technology vol. 98 (2018), pp. 1807 – 1816.

Appendix

A.1 List of embedded publications

Publication P1: Hartl, R.; Landgraf, J.; Spahl, J.; Bachmann, A.; Zaeh, M. F.: Automated visual inspection of friction stir welds: a deep learning approach. In: Stella, E. et al. (Eds.): Proceedings of SPIE Vol. 11059, Multimodal Sensing: Technologies and Applications. Munich, Germany, June 24 – 27, 2019. Bellingham, WA, USA: SPIE 2019, 1105909. ISBN: 9781510627970.

Publication P2: Hartl, R.; Bachmann, A.; Liebl, S.; Zens, A.; Zaeh, M. F.: Automated surface inspection of friction stir welds by means of structured light projection. IOP Conference Series: Materials Science and Engineering vol. 480 (2019), 012035.

Publication P3: Hartl, R.; Praehofer, B.; Zaeh, M. F.: Prediction of the surface quality of friction stir welds by the analysis of process data using Artificial Neural Networks. Proceedings of the Institution of Mechanical Engineers, Part L: Journal of Materials: Design and Applications vol. 234 (2020) 5, pp. 732 – 751.

Publication P4: Hartl, R.; Hansjakob, J.; Zaeh, M. F.: Improving the surface quality of friction stir welds using reinforcement learning and Bayesian optimization. The International Journal of Advanced Manufacturing Technology vol. 110 (2020) 11 – 12, pp. 3145 – 3167.

Publication P5: Hartl, R.; Vieltorf, F.; Zaeh, M. F.: Correlations between the Surface Topography and Mechanical Properties of Friction Stir Welds. Metals vol. 10 (2020) 7, 890.

Publication P6: Hartl, R.; Vieltorf, F.; Benker, M.; Zaeh, M. F.: Predicting the Ultimate Tensile Strength of Friction Stir Welds Using Gaussian Process Regression. Journal of Manufacturing and Materials Processing vol. 4 (2020) 3, 75.

A.2 List of supervised student research projects

In the context of the research performed by the author, various student research projects (see Table A.1) were intensively supervised with regard to the methodology, problem statements, objectives, and approach, along with the interpretation and documentation of the results. The supervision took place at the Institute for Machine Tools and Industrial Management (*iwb*) of the Technical University of Munich (TUM). The findings and results of the student research projects listed below have contributed to this dissertation. The author would like to express his sincere gratitude for the remarkable commitment of all supervised students and their interesting and important contributions.

Table A.1: Summary of supervised student research projects

Names of students	**Type, title, date of submission, and language of the written documentation of the research project**
Bigge, A.	Master's thesis, "Analysis of Process Variables in Friction Stir Welding Under the Influence of Disturbance Variables," submitted in March 2018, German, (*iwb* no. 2018/40032)
Zappe, T. and Ziaras, S. D.	Interdisciplinary project (Department of Informatics), "Development of a Relational Database for Friction Stir Welding," submitted in May 2018, German, (*iwb* no. not available)
Fuss, F.	Master's thesis, "Process Analysis for Friction Stir Welding of the Aluminum Alloy EN AW-5754," submitted in August 2018, German, (*iwb* no. 2018/42145)
Daisenberger, F.	Semester's project (Master's), "Production of an Industry 4.0 Demonstrator Component for Friction Stir Welding," submitted in November 2018, German, (*iwb* no. 2018/43329)
Landgraf, J. and Spahl, J.	Interdisciplinary project (Department of Informatics), "Automated Visual Inspection of Friction Stir Welds: A Deep learning Approach," submitted in November 2018, English, (*iwb* no. not available)
Mehn, J.	Bachelor's thesis, "Extension of an In Situ Measuring System for Real-time Recording of Process Responses During Friction Stir Welding," submitted in April 2019, German, (*iwb* no. 2019/45146)
Praehofer, B.	Master's thesis, "Analysis of Process Data in Friction Stir Welding by Means of Artificial Intelligence," submitted in April 2019, German, (*iwb* no. 2019/45147)
Hansjakob, J.	Interdisciplinary project (Department of Informatics), "Optimization of the Surface Quality of Friction Stir Welds using Reinforcement Learning and Bayesian Optimization," submitted in November 2019, German, (*iwb* no. not available)
Vieltorf, F.	Master's thesis, "Prediction of Mechanical Seam Properties in Friction Stir Welding Using Artificial Intelligence," submitted in November 2019, German, (*iwb* no. 2019/48282)

Rittau, D.	Semester's project (Master's), "Inline Quality Inspection and Control in Friction Stir Welding by Analysis of the Weld Topography," submitted in December 2019, German, (*iwb* no. 2019/47668)
Mair, T.	Master's thesis, "Prediction of Internal Irregularities in Friction Stir Welding Using Artificial Intelligence," submitted in June 2020, German, (*iwb* no. 2020/51366)
Steinhauser, M.	Master's thesis, "Predicting the Seam Quality in Friction Stir Welding Using Artificial Intelligence," submitted in December 2020, German, (*iwb* no. 2020/54053)

A.3 List of the software used for data processing

The following list contains the most important software packages, modules, and frameworks that were used for data processing. Additionally, the publication in which the software was used, is indicated.

- Anaconda 3-5.0.1 (P1, P4), Python 3.6 (P1, P4), and Pycharm 2018.3.4 (P1, P4) with the following:
  - Keras-Preprocessing 1.0.9 (P1) and Keras-Applications 1.0.7 (P1)
  - Matplotlib 3.0.2 (P1) and Matplotlib 3.1.1 (P4)
  - Numpy 1.15.4 (P1) and Numpy 1.17.2 (P4)
  - Pandas 0.23.4 (P1)
  - Scikit-learn 0.20.0 (P1)
  - Scipy 1.1.0 (P1) and Scipy 1.3.1 (P4)
  - Tensorflow-gpu 1.5.0 (P1) and Tensorboard 1.5.0 (P1)
  - Torch 0.4.1 (P1)
  - YOLOv2 (P1) and Darkflow 1.0.0 (P1)
- Matlab R2017b (P2) and Matlab R2019a (P3, P6) with the following:
  - Bioinformatics Toolbox 4.2 (P6)
  - Deep Learning Toolbox 12.1 (P3)
  - Deep Learning Toolbox Model for AlexNet Network 19.1.0 (P3)
  - Deep Learning Toolbox Model for VGG-19 Network 19.1.0 (P3)
  - Gaussian Process Regression and Classification Toolbox 3.1 (P6)
  - Parallel Computing Toolbox 7.0 (P3)
  - Signal Processing Toolbox 8.2 (P3)
  - Vehicle Network Toolbox 4.2 (P3)
- Microsoft Excel 2016 (P1 – P6)

A.4 Visualization of the Gaussian process by a three-dimensional surface plot

In Figure A.1, the GP is visualized for Study 1, after three process parameter sets were tested. The BO multi-task approach, which was presented in Subsection 5.3.3, was used to find suitable process parameters. The values for the surface defects *def* in the intervals between the welding speeds of 500 mm/min, 833 mm/min, 1167 mm/min, and 1500 mm/min were determined by linear interpolation. The optimum at a welding speed of 500 mm/min and a tool rotational speed of 1500 min^{-1} was already found in the first three steps. For better readability, the values for the acquisition function are not displayed in Figure A.1.

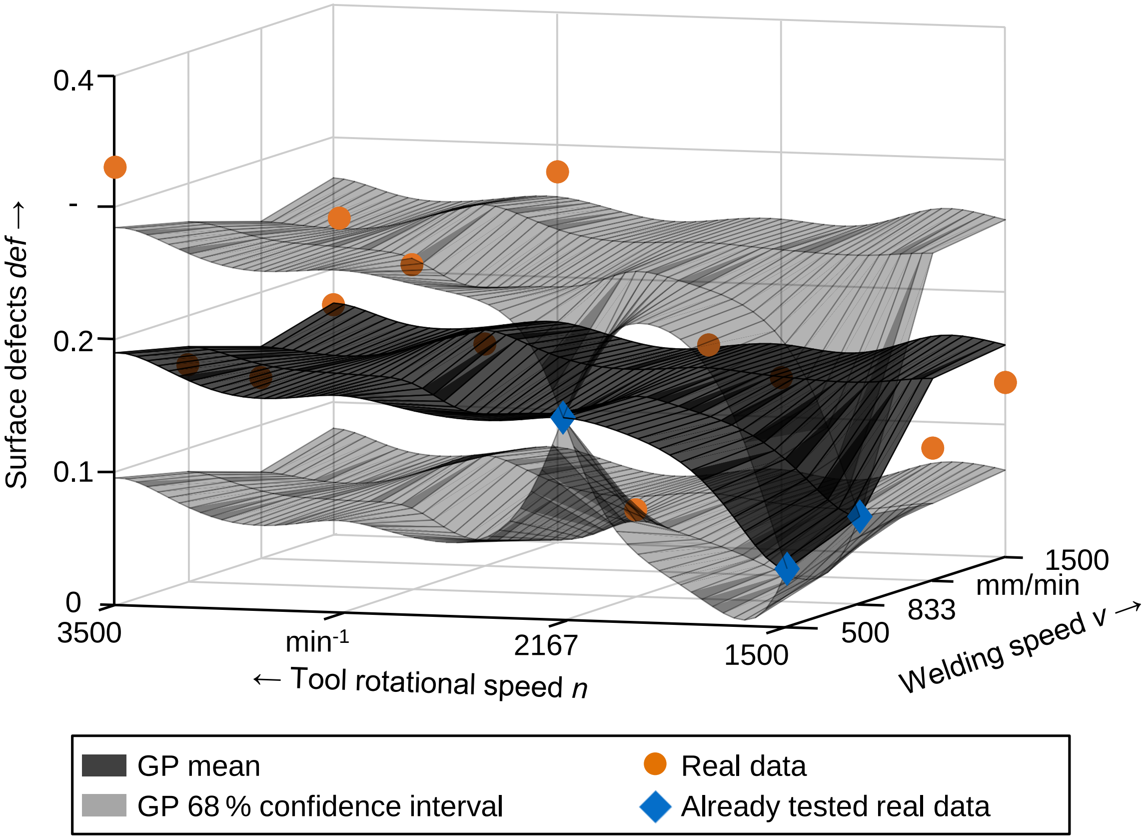

Figure A.1: Three-dimensional surface plot of the GP after three tested parameter sets in Study 1 using the BO multi-task approach (based on HARTL ET AL. 2020b)